UNIVERSIDADE
BEIRA INTERIOR

Design of an Experimental Rig for the Testing of Helium Compressor Cascades

Versão final após defesa

Fernando Jorge Queirós Pokee

Dissertação para obtenção do Grau de Mestre em
Engenharia Aeronáutica
(mestrado integrado)

Orientador: Prof. Dr Francisco Miguel Ribeiro Proença Brojo
Co-orientador: Prof. Dr João Amaral Teixeira

Maio de 2021

Resumo

O hélio é um gás quimicamente inerte e não radioactivo, o que o torna ideal para um ambiente de central nuclear onde as fugas radioactivas representam uma grande preocupação. Estas propriedades do gás ajudam a aumentar os fatores de segurança, bem como diminuir o processo de envelhecimento dos componentes da fábrica. Esta dissertação descreve o projeto e os detalhes do dimensionamento de um túnel de vento subsónico de baixa velocidade e tamanho médio a fim de testar uma cascata de pás de compressor de hélio. O túnel de vento foi projetado para atingir 100 m/s na secção de teste com nível de turbulência de baixa intensidade esperado. Para cumprir tais objetivos, foi levada a cabo uma concepção detalhada utilizando análises teóricas, simulação CFD numa pá de compressor em cascata e métodos semi-empíricos, todos eles aplicados para melhorar a qualidade de escoamento ao longo das secções do túnel de vento. Uma atenção cuidadosa foi dada à concepção das placas de canto e a montagem da secção de teste enquanto que o ventilador do túnel foi elaborado por um aluno diferente. O controle e estabilização de escoamento foram alcançados utilizando telas e telas de ninhos de abelha, ambos otimizados para induzir baixos níveis de turbulência na seção de teste. O projeto e a construção de cada secção do túnel de vento foram apresentados e discutidos, relevando os aspectos técnicos e apresentando também algumas diretrizes de concepção e fabrico para os principais componentes de um túnel de vento subsónico.

Keywords

Túnel de Vento; Cascata compressor para hélio; gás hélio

Abstract

Helium is a chemically inert and nonradioactive gas which makes it ideal for a nuclear power plant environment where radioactive leaks present a high concern. These properties of helium gas help to contribute to a safer working environment of these plants as well as to decrease the aging process of the plant components. This dissertation describes the design and some of the construction details of a medium size subsonic low speed wind tunnel to test a helium compressor cascade. The wind tunnel has been designed to achieve 100 m/s at the testing section with expected low intensity turbulence level. In order to accomplish such objectives, a detailed design was carried on using theoretical analyses, CFD simulation on a cascade compressor blade and semi-empirical methods, all of them applied to improve the flow quality through the wind tunnel sections. A careful attention has been focused on the design of the corner vanes and the test section assembly whilst the fan design was designed by a different student. Flow control and stabilization was achieved using screens and honeycombs, both of them optimized to induce low turbulence levels at the testing section. The design of each wind tunnel section has been presented and discussed shedding light on the most relevant technical aspects and an attempt is made to describe some design and manufacture guidelines for the main components of a low subsonic wind tunnel.

Keywords

Wind Tunnel; helium gas; Helium compressor Cascade.

Contents

Resumo v

Abstract vii

Contents ix

List of Figures xi

List of Tables xv

List of Abbreviations xvii

Nomenclature xix

Acknowledgment xxiii

Declaration xxv

1 Introduction 1

1.1 Background and justification of the work . . . 1
1.2 Aim and Objectives . . . 2
1.3 Thesis Structure and Organization . . . 3

2 State of the art 5

2.1 Generation IV of nuclear reactors . . . 6
2.2 Principles of a Wind Tunnel . . . 12
2.3 Wind Tunnel Models . . . 19
2.4 Elementary Cascade Theory . . . 25
2.5 Early Cascade Experiments . . . 27
2.6 Instrumentation and Calibration of the Test Section . . . 38
2.7 Pressure Losses and Turbulence Reduction Estimate . . . 40

3 Wind Tunnel Design Methodology 47

3.1 Design Criteria . . . 47
3.2 Test Section . . . 48
3.3 The Diffuser . . . 51
3.4 Corner Ducts . . . 52
3.5 Power Considerations . . . 55

3.6 The Contraction Cone 56
3.7 Honeycomb and screens 58
3.8 Cooling 59

4 Results **63**
4.1 General Description 63
4.2 Test Section 64
4.3 The Diffuser 66
4.4 Corner Ducts 69
4.5 The Fan Section 70
4.6 Honeycomb and screens 72
4.7 The Contraction Cone 73
4.8 Cooling 75
4.9 Total Pressure Loss 75
4.10 Wind Tunnel Views 80

5 Discussion **85**

6 Conclusions **89**

References **93**

A State of the Art **97**
A.1 Results 97
A.2 Worksheets 100

List of Figures

1.1 Ilustration of a Gas Turbine Power Plant [4] 1

2.1 Baseline design of GTHTR300 horizontal helium gas turbine in pressure vessel[28]. 10

2.2 Sketch of the jet engine components and corresponding thermodynamic states[24]. 11

2.3 Closed Brayton cycle gas turbine engines[24]. 12

2.4 Moody Chart[16]. 16

2.5 Boundary Layer[5]. 17

2.6 Working models for closed test section[3]. 18

2.7 Working models for open test section[3]. 18

2.8 Open-Loop Circuit Wind Tunnel[18]. 19

2.9 Closed-loop circuit wind tunnel [6]. 20

2.10 Characteristics of wind tunnels designed for the different speed regimes[3]. 21

2.11 Closed test-section cases[3]. 23

2.12 Open jet test-section cases[3]. 23

2.13 Cascade Tunnel[13]. 26

2.14 Compressor Cascade[13]. 26

2.15 Velocity Triangle[3] 27

2.16 Schematic of experimental setup [20]. 27

2.17 Cascade Assembly [20]. 28

2.18 Loss coefficient ζ for cascades of various solidity ratios d/c and various blade angles β; blade section NACA 0010; Reynolds number R2 = 5x10e5, fully turbulent boundary layer The circles with projected lines on the theoretical curves indicate the beginning of separation[22]. 30

2.19 Loss coefficients ζ of turbine cascades of various solidity ratios d/c and various blade angles β; blade section NACA 8410: Reynolds number R20= 5x10e5[22]. 31

2.20 Blade sections of the single-stage axial flow compressor of Figure 4[22]. . 31

2.21 Characteristic curves of a single-stage axial flow compressor, as calculated theoretically from cascade data, by N. Scholz. Pressure coefficient and efficiency coefficient against mass flow coefficient. 32

2.22 Cascade geometry for pressure distribution measurements in the High Speed Cascade Wind Tunnel; blade section NACA 0010[22]. 33

2.23 Cascade geometry for pressure distribution measurements in the High Speed Cascade Wind Tunnel; blade section NACA 8410[22]. 34

2.24 Pressure distribution measurements of cascades in compressible flow; blade section NACA 0010; Reynolds number R, = $W.C/TO$ = 3x10e5; see Figure 2.22 [22]. 35
2.25 Pressure distribution measurements of compressor cascades in compressible flow;blade section NACA 8410; Reynold number R2 = w^2c/v = 3xl0e5;see Figure 2.23[22]. 36
2.26 Pressure distribution measurements of turbine cascades in compressible flow; blade section NACA 8410; Reynolds number R2 = w2c/v = 5xl0e5; see Figure 2.23 [22]. 36
2.27 Comparison of theoretical and experimental velocity distribution of cascades in compressible flow. Theory from Prandtl-Glauert rule; experiments, see Figure 2.24 Blade section NACA 0010; Reynolds number R = wc/v = 3xl0e5[22]. 37
2.28 Wind and body reference frames [3]. 38
2.29 Manometer[8]. 39
2.30 Types of pitot tube [8]. 40
2.31 Forces and velocities in a blade cascade[17]. 41
2.32 Values of the resistance coefficient C for different shapes of bodies[7]. 43

3.1 Cascade notation: Θ =camber, Γ =stagger, i =incidence, ε =deflexion, δ =deviation, α =air inlet angle, β =air efflux angle[25]. 49
3.2 Schematics of cascade design. 50
3.3 Schematics of the diffuser's expansion parameters(adopted from [3]). . . 51
3.4 Description of the corner duct. 53
3.5 Schematics of vane numbering(adopted from[1]). 54
3.6 Schematics of the contraction shape[ ]. 58
3.7 Variations of turbulence intensity Vs. velocity with one screen and four screens[23]. 60

4.1 Schematics of the wind tunnel with average velocity distribution 64
4.2 Front view of the compressor cascade 65
4.3 First diffuser design 66
4.4 Second diffuser design 67
4.5 Third and fourth diffuser design 68
4.6 Fifth diffuser 68
4.7 First corner vanes 69
4.8 Second corner design 70
4.9 Nose, fan and tail design 71
4.10 Fan blades. 72
4.11 Tri-dimensional of honeycomb and screens. 73
4.12 Contraction Design. 74
4.13 Simulation of cascade blade s/c=0.7 77
4.14 Variation of pressure with velocity 80
4.15 Bi-dimensional top view of the wind tunnel. 81
4.16 Bi-dimensional front view of the wind tunnel. 81
4.17 Bi-dimensional left view of the wind tunnel. 81
4.18 Engine in the tri-dimensional view of the wind tunnel. 82

4.19 Tri-dimensional open view of an open Wind tunnel. 82
4.20 Tri-dimensional closed view of Wind tunnel. 83

A.1 Side view of the first diffuser. 97
A.2 Front view of the first diffuser. 98
A.3 Left view of the second diffuser. 98
A.4 Right view of the third and fourth diffuser. 98
A.5 Top view of the third and fourth diffuser. 99
A.6 Front view of the fifth diffuser. 99
A.7 Similarity parameters with GTHTR300. 100
A.8 Cascade forces. 101
A.9 Cascade design. 102
A.10 Cooling estimations. 102
A.11 Component dimensioning. 103
A.12 Component dimensioning(continuation). 104
A.13 Test section and settling chamber design. 104
A.14 Screens comparison. 105
A.15 Liming Peng estimations. 105
A.16 Diffusers design. 105
A.17 Corner ducts design. 106
A.18 Contraction design. 106
A.19 Complementing estimations and graphics. 106

List of Tables

2.1 Goals for Generation IV nuclear energy systems[21] 7
2.2 GTHTR300 design and minimally expected performance data[28]. 9
2.3 Parameters of the test blades[20]. 28

3.1 Mach number Range - Compressor blades section type correlation[27] . . 56

4.1 Diffuser dimensions 67
4.2 Corner dimensions 69
4.3 Fan dimensions in meters 71
4.4 Blade design parameters 71
4.5 Blade design parameters 72
4.6 Screens dimensioning[4] 73
4.7 Contraction dimensions 75
4.8 Flow cooling temperature estimation 75
4.9 Total dynamic pressure loss estimations for the compressor cascade with s/c equal to 1.2 76
4.10 Total dynamic pressure loss estimations for the compressor cascade with s/c equal to 0.7 77
4.11 Total dynamic pressure loss estimation comparison between air and helium for the compressor cascade with s/c equal to 1.2 79

List of Abbreviations

BWRs	Boiling Water Reactors
CANDU	Canadian units with deuterium uranium
CFD	Computational Fluid Dynamics
CBC	Closed Brayton Cycle
GIF	Generation International Forum
HTTR	High Temperature Engineering Test Reactor
JAERI	Japan Atomic Energy Research Institute
LWRs	Light Water Reactors
MWe	Megawatt of electric power
MWt	Megawatt of thermal power
PWRs	Pressurized Water Reactors
rms	Root mean square
rpm	Rotation per minute
VHTRs	Very High Temperature Reactors

Nomenclature

V	Absolute Velocity of the fluid
C	Airfoil Chord
β	Blade Angle
α	Cascade blade notation:air inlet angle
Θ	Cascade blade notation:camber
β	Cascade blade notation:air efflux angle
ε	Cascade blade notation:deflection
δ	Cascade blade notation:deviation
i	Cascade blade notation:incidence
Γ	Cascade blade notation:stagger
L_x	Cascade horizontal length
L_y	Cascade vertical length
CW	Compression work
A_0	cross section's area
ρ	Density

δ^* Displacement Thickness

η Efficiency

E_R Energy Ratio

W_{ent} Entrance Width

H_{ent} Entrance Height

W_{ext} Exit Width

H_{ext} Exit Height

Γ Flow Circulation

Φ Flow Coefficient

g Gravitational acceleration

y Half of the difference between the inlet and outlet width of the diffuser

D_H Hydraulic Diameter

L Length

M Mach number

$\dot{m}$ Mass flow rate

V_m Mean velocity

θ Momentum Thickness

Ncornerradius Non dimensional corner radius

h Planck constant

P Pressure

ψ	Pressure Coefficient
$Q, \dot{V}$	Volumetric flow rate
γ	Ratio of specific heats (at constant pressure and constant volume)
Re	Reynolds number
Re_d	Reynolds number based on wire diameter
H	Shape factor
S	Space between blades
c	Speed of light in a vacuum inertial frame
V_{W1}	Tangential component of V (absolute velocity), called Whirl velocity
V_{W2}	Tangential component of V_m (mean velocity)
T_{in}	Temperature at inlet
T_{out}	Temperature at outlet
W	Work

Acknowledgment

This thesis is the result of the collaboration opportunity between the University of Beira Interior, Portugal, and Cranfield University, Bedfordshire, United Kingdom, provided by the Erasmus internship programme throughout the academic year 2019/2020. I would first like to acknowledge Dr Engineer Francisco Brojo, President and Professor of the Department of Aerospace at the University of Beira Interior, thanks to whom I was able to bring this thesis to conclusion.

In particular, I would like to express my sincere gratitude to my supervisor Dr João Teixeira, Lecturer for Centre for Propulsion Engineering, for his guidance and infallible support, time, motivation, encouragement, patience and professional insights. It was, indeed, a compass for this present collaborative work and a fuel of enthusiasm and knowledge during the research I carried out.

And to Engineer Arnold G.Briggs, former Cranfield University student, the Founder and Executive Director at EGB Engineering, as his followance and guidance to the project was undoubtedly fundamental and inspiring.

Thirdly, I would like to thank my professors of the master course "Sciences of Aeronautical Engineering" from the University of Beira Interior that taught me some of the skills and tools to develop this present project.

Finally, I would like to extend my thanks to family and friends. Especially, I would like to acknowledge my marvellous parents for their unconditional love and support, as well as my amazing sister Diana, who accompanied me throughout my entire life. To them, I express my eternal love. I would like to thank as well my friends made through

my life experience and short stay in England as well all the people that supported me during the pandemic. I thank them all for their support, love, and encouragement through the elaboration of this master's thesis.

Declaration

I hereby declare that this thesis is my own effort. All use of secondary sources has been cited in the reference section. If there are any mistakes in this report, it is not intentional in any way.

Signature:

Date:

Chapter 1

Introduction

1.1 Background and justification of the work

Generation IV nuclear power plants are being developed as non carbon emitting generation units with in built safety features designed to overcome proliferation, ensure operational integrity and, fuelling availability and to address societal concerns. This generation of nuclear power plant is the result of a cooperative international endeavor set up and promoted by a large number of countries, organized as part of the Generation IV International Forum(GIF).

The current focus of the GIF concerns the development of Generation IV nuclear reactors which meet the objectives mentioned above. The present research work

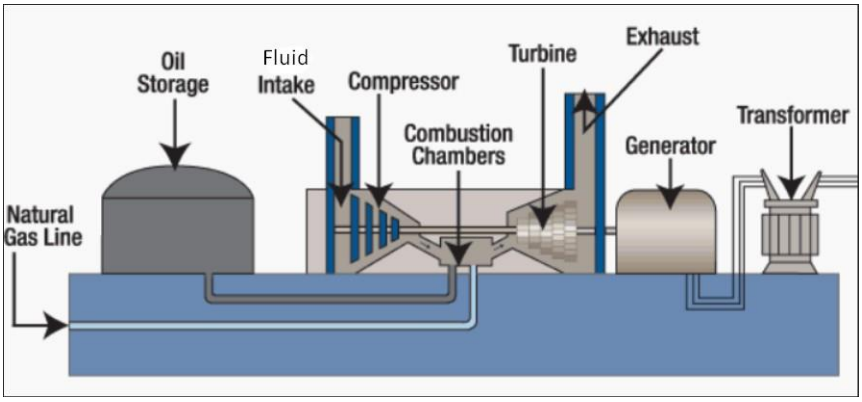

Figure 1.1: Ilustration of a Gas Turbine Power Plant [4]

falls within this domain and deals with the provision of helium gas as the working fluid in the primary cooling cycle of Generation IV plant. Figure 1.1 illustrates a Gas Turbine Power Plant in which the engine is a Compressor. Helium is a chemically inert and non-radioactive gas, and these properties contribute to the safe working environment of these plants as well as retarding the aging process of plant components. The lack of limited availability of helium turbomachinery data has made it difficult to study in detail the performance of the gas turbine components employed in these Very High Turbine Reactor powered cycles. Hence, further development and add experience and experimental data are greatly needed in this particular area.

A wind tunnel was designed to create a controlled environment of fast moving helium in order to analyze the flow over helium gas compressor blades. Cascade wind tunnels used to determine measurements of lift, drag, yaw, pitch, and roll momentum. They are also used to obtain a characterization of the flow through visualization techniques and this to gather information correlating blade design parameters, thickness distribution, camber, stagger and pitch to chord ratio, with boundary layer and separation information, all of which is very useful for turbomachinery design.

1.2 Aim and Objectives

In order to enable the experimental investigation of helium turbomachinery blading at reduced scale but at the same time representative flow conditions, the dissertation is developed with the detailed thermodynamic and aeromechanical calculations. The aim of the present dissertation is the design together with calculations for the partial fabrication of a new low turbulence wind tunnel facility with a versatile experimental setup suitable for a turntable helium compressor cascade and aerodynamic measurements on its blades. This should enable easy interchanges to study the influence and performance of different airfoils for use in helium turbomachinery applications. The following objectives can be listed:

- Conduct a review of literature focused on helium turbomachinery for power generation, as well as wind tunnel design principles and theories.
- Conduct a detailed calculation of each of the key components of the helium wind tunnel.
- Provide specifications to enable specialist analysis of power plant and numerical cascade investigations.

1.3 Thesis Structure and Organization

The thesis report is organized into seven chapters. This chapter presents the dissertation in an introductory way with background and justification of the work, aims and objectives and the structure of the thesis. In the second chapter, a literature review is presented, which includes an historical perspective and introduces knowledge to the development of a wind tunnel facility. In the third chapter, the wind tunnel design methodology is presented together with the calculations used. Chapter Four contains the presentation of the results. The general discussion of the data is presented in Chapter Five. Chapter Six introduces the conclusion and in the Chapter Seven, the potential future work is discussed.

Chapter 2

State of the art

A literature review is carried out by researching aspects of wind tunnels to base the knowledge and principles to be implemented in the new wind tunnel. The concept of wind tunnel testing originated from the fact that whether aircraft moves against wind or wind moves against aircraft, the aerodynamic loads generated are same. In the eighteenth century, the aerodynamic scientists also know as "aeronauts" closely studied the flight of birds and then started building flying machines patterned after avian structures. Their birdlike project failed terribly. Then the "aeronauts" realised that in reality, they still only knew too little of how air interacts with moving or stationary objects and also about the lift and drag forces that act on the surfaces cutting through the atmosphere. In order to fly, man first had to understand the flow of air over the flying object surfaces. So, in order to try to simulate this, they built instrumented facilities in which wings, fuselages, and control surfaces could be tested under controlled conditions. The first wind tunnel test was performed by Benjamin Robins using a whirling arm in 1746(Donald D. Baals & William R. Corliss 1981). [2]

The structure of the literature review comprises of 7 sub-chapters. The first sub-chapter gives understanding of Generation IV nuclear systems. The second two sub-chapters discusses the principles and basic models of the wind tunnel including the helium research. Afterwards, an elementary cascade theory followed by cascade experiments.

The sixth sub-chapter reveals basic concept and instruments concerning the test section. The final sub-chapter gives an explanation on the estimations involving the pressure losses coefficients.

2.1 Generation IV of nuclear reactors

This section gives an insight of the evolution of nuclear power plants, research of the nuclear power plant GTHTR300 and the Brayton power cycles.

2.1.1 Introduction to Generation IV

Generation IV International Forum (GIF) is an international organization founded and kept together by a large number of countries. It was set up to carry out the research and development needed to establish the viability and performance capabilities of the next generation nuclear energy systems. The current works and pressure are put to develop Generation IV nuclear reactors. The evolution of nuclear power plants has conventionally grown from four generations and may be described as[21]:

1. Generation I (1950-1970): first prototypes of several designs;

2. Generation II (1970-1995): comercial power plants,reliable and economically competitive, Light Water Reactors (LWRs) - Pressurized Water Reactors (PWRs) and Boiling Water Reactors (BWRs), Canadian units with deuterium uranium(CANDU) and Russian pressurized counterpart of PWR- VVER-1000 and with bad publicity due to Chernobyl disaster;

3. Generation III (1995-2030): evolution of II generation LWR with increased safety and economic factors in comparison. They still are being developed and utilized by the industry;

4. Generation IV (2030+): the generation of nuclear reactors which are currently being investigated. New technologies are taken into account in order to improve the

following criteria such as economic competitiveness, enhanced safety, minimizing of waste generation and proliferation resistance.

2.1.2 Goals of Generation IV

During GIF meetings and conferences, there have been defined eight technology objectives for Generation IV systems across four areas such as sustainability, economics, safety and reliability, and proliferation resistance and physical protection. These ambitious goals aim at evaluating the economic, environmental, and social requirements of the current century. They establish a framework and identify concrete targets for GIF efforts.[21]

The main tasks and requirements for the technology are summarized briefly in Table 2.1 with more detailed explanation.

Table 2.1: Goals for Generation IV nuclear energy systems[21]

Goals for Generation IV nuclear energy systems	
Sustainability-1	Generation IV nuclear energy systems will provide sustainable energy generation that meets clean air objectives and provides long-term availability of systems and effective fuel utilization for worldwide energy production.
Sustainability-2	Generation IV nuclear energy systems will minimize and manage their nuclear waste and notably reduce the long-term stewardship burden, thereby improving protection for the public health and the environment.
Economics-1	Generation IV nuclear energy systems will have a clear lifecycle cost advantage over other energy sources.
Economics-2	Generation IV nuclear energy systems will have a level of financial risk comparable to other energy projects.
Safety and Reliability-1	Generation IV nuclear energy systems operations will excel in safety and reliability.
Safety and Reliability-2	Generation IV nuclear energy systems will have a very low likelihood and degree of reactor core damage.
Safety and Reliability-3	Generation IV nuclear energy systems will eliminate the need for offsite emergency response.
Proliferation Resistance and Physical Protection	Generation IV nuclear energy systems will increase the assurance that they are very unattractive and the least desirable route for diversion or theft of weapons-usable materials, and provide increased physical protection against acts of terrorism.

2.1.3 High temperature gas-cooled reactors GTHTR300

The Japan Atomic Energy Research Institute (JAERI) has carried a successful development on the operations of the High Temperature Engineering Test Reactor (HTTR). The project's goal is to study applied systems of the reactor technology. One of these programs, it is the design and development of the Gas Turbine High Temperature Reactor of 300 MWe nominal capacity (GTHTR300). The GTHTR300 program has a fuel cycle design that is based on an improved HTTR fuel element and also a simple plant system. One of the aims of this program is the economical performance and efficiency.

This power plant incorporates a conventional steel reactor pressure vessel, non intercooled power conversion cycle as well an horizontal single-shaft turbomachine. The research also includes performance tests of subscale components and its system control. Table 2.2 shows the design and minimally expected performance data.[28]

Table 2.2: GTHTR300 design and minimally expected performance data[28].

Overall plant	
Reactor power	600 MWt/unit (4 units/plant)
Reactor pressure vessel	SA533 (Mn–Mo) steel
Reactor safety system	No active emergency system
Radioactive nuclide retention	Confinement
Plant cycle	Non-intercooled Brayton cycle
Power generation	280 MWe
Net power output	274 MWe
Net generating efficiency	45.6%
Plant capacity factor	>90%
Reactor core	
Coolant inlet/outlet temperature	587/850 °C
Coolant inlet pressure	6.92 MPa
Core coolant pressure loss	60 kPa
Average power density	5.8 W/cm^3
Fuel element	Pin-in-block prism
Fuel cycle	LEU once through cycle
Enrichment	14%
Average burnup	112 GWd/ton
Shutdown refueling	Once per 2 years
Refueling duration	30 days
Turbomachine	
Shaft design type	Horizontal, single shaft
Shaft speed	3600 rpm
Turbine inlet pressure	6.84 MPa
Turbine mass flow	438.1 kg/s
Turbine expansion ratio	1.87
Number of turbine stages	6
Turbine polytropic efficiency	93.0%
Compressor inlet temperature	28 °C
Compressor pressure ratio	2.0
Number of compressor stages	20
Compressor polytropic efficiency	90.5%
Generator drive	Cold-end, diaphragm coupling
Generator type	Synchronous
Generator cooling	7 MPa helium cooled
Generator efficiency	98.7%
Heat exchangers	
Recuperator design type	Plate-fin surface, 6 modular units
Recuperator thermal rating	1006 MWt
Recuperator effectiveness	95.0%
Recuperator total pressure loss	1.7%
Recuperator construction material	Type 316SS
Precooler design type	Helical-coiled finned tube bundle
Precooler thermal rating	323 MWt
Cooling water inlet temperature	22 °C
Precooler design LMTD	38 °C
Precooler tubing material	Carbon steel (STB410)

2.1.4 GTHTR300 Helium Gas Turbine

The design of helium gas turbine of the plant GTHTR300 is a single-shaft, axial-flow design having six turbine stages and twenty non-intercooled compressor stages, shown in Figure 2.1. The gas turbine powered at 300MWe and 3,600 rpm drives a synchronous generator. The gas turbine is set horizontally so that the bearing loads are minimized. The design characteristics were chosen respecting the established industrial practice in combustion gas turbines. There are new elements incorporated in the gas turbine baseline unit, mainly the narrow compressor flowpath, that results from working in helium, and the use of rotor magnetic bearings in order to avoid large pressure boundary penetration or potential lubricant contamination to the reactor system. The development and experiment programs were carried out to validate new technology components.

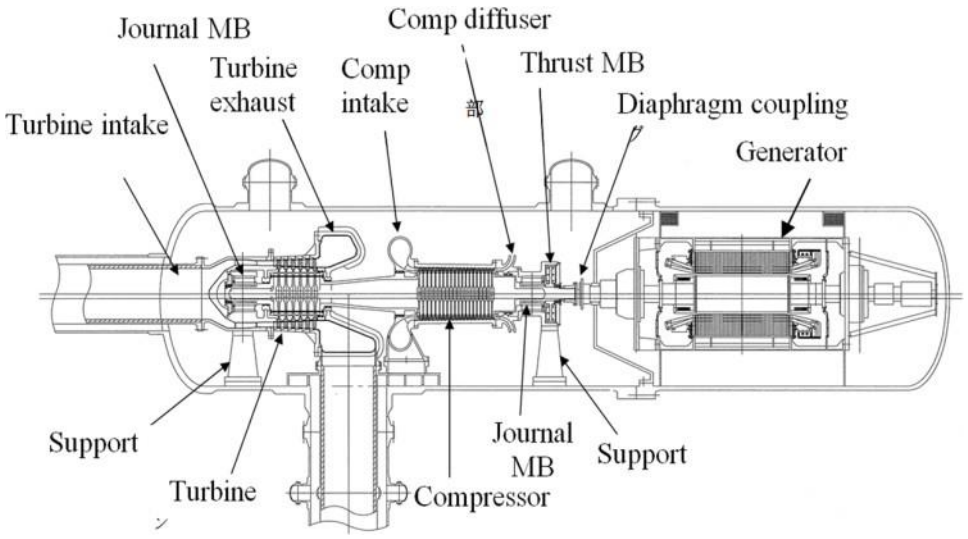

Figure 2.1: Baseline design of GTHTR300 horizontal helium gas turbine in pressure vessel[28]

2.1.5 Brayton power cycle

The Brayton cycle represents the operation of a gas turbine engine. The cycle consists of four processes, alongside a sketch of an engine as presented in Figure 2.2[24]:

- From a to b, there's an adiabatic, reversible compression in the inlet and compres-

sor;

- From b to c, there's a constant pressure fuel combustion;
- From c to d, there's an adiabatic, reversible expansion in the turbine and exhaust nozzle;
- From d to a, the air is cooled at constant pressure back to its initial condition.

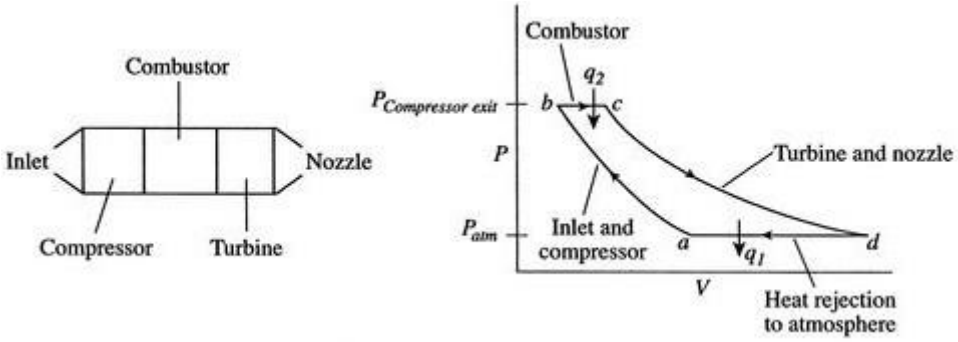

Figure 2.2: Sketch of the jet engine components and corresponding thermodynamic states[24].

2.1.6 Closed Brayton power cycle

For Space Power Systems Engineering and nuclear reactor power and propulsion systems, Closed Brayton Cycles (CBC) are used. The working fluid does not come in contact with atmospheric air.

The compression and expansion processes remain the same but the combustion process is replaced by a constant pressure heat addition(Q_H) process from an external source.

In the exhaustion process, the pressure heat is outcasted to the environment. The cold gas is drawn into the compressor, where its temperature and pressure are raised. The high pressure air passes through a heat exchanger, where the fuel is burned at constant pressure and hits its peak temperature. The high temperature gases then proceeds into the turbine where it expands to atmospheric pressure while producing output power. Some

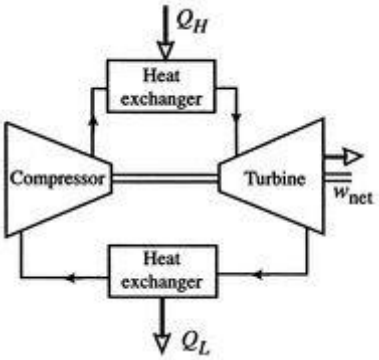

Figure 2.3: Closed Brayton cycle gas turbine engines[24].

of the output power (W_{net}) is used to drive the compressor and the remaining is available as shaft work. The exhaust gases leaving the turbine are cooled in a heat exchanger (Q_L) where it also partially rejects heat. The gas is restored to its initial state. There, in this cycle the same working fluid is recirculate causing the cycle to be classified as closed cycle. In both heat exchangers (Q_H and Q_L), these are used either to reject heat to the environment or a heat recovery steam generator. The waste heat derived from the combustion gases or rejected heat may also be used for industrial or domestic purposes, such as hot water supply.

When it comes to using an inert such as Helium instead of air as the working fluid, there are materials in the Turbine Design, such as Molybdenum alloys that are more adequate. This alloy has high stress properties at elevated temperature above 1000 degree centigrade. Through such material, the turbine plant efficiency increment over 50 % can be achieved.

2.2 Principles of a Wind Tunnel

Wind tunnel is an aerodynamic research tool that uses many working principles. To fully understand the main principles used, some fundamental working principles will be explained.

2.2.1 Bernoulli's Principle

Bernoulli's Principle states that the total pressure is constant for an incompressible and inviscid fluid travelling along a streamline. Equation 2.1 shows Bernoulli's Principle as applied to an ideal fluid flow:

$$constant = P_{static} + \rho g z + q \tag{2.1}$$

From Equation 2.1, total pressure is equivalent to the total pressure where the static pressure is P_{static}(Pa), $\rho(kg/m^3)$ is the density, g (m/s^2) is the gravitational acceleration, z (m) is height above reference level and q (kg/ms) is the dynamic pressure.

Along a streamline, an increase of static pressure leads to a decrease in velocity and vice versa. Hence, the equation can be simplified into Equation 2.2 . This principle can be used to estimate the velocity of an airflow when both total and static pressure is known:

$$P_{tot} = constant = P_{stat} + q \tag{2.2}$$

Where dynamic pressure (q)[Pa] is expressed in Equation 2.3 through velocity (v)

$$q = 1/2 \times \rho \times v^2 \tag{2.3}$$

However, pressure losses due to the friction of the fluid to the surface of the duct should be considered. Therefore the original equation can be expressed on Equation 2.4. It shows the equivalent equation between two points in a wind tunnel which is from the entrance to the exit of the tunnel.

$$P_{stat1} + q_1 - \Delta P_{tot} = P_{stat2} + q_2 \tag{2.4}$$

Where ΔP_{tot} is the sum of frictional and local pressure losses (Pa)

2.2.2 The Law of Conservation of Mass

The Law of conservation of mass claims that if there are no possible discharge of mass to another system, the mass in the system will be kept constant at any time. Equation 2.5 describes the law.

$$\dot{m} = \rho_1 V_1 A_1 = \rho_2 V_2 A_2 \tag{2.5}$$

where $\dot{m}$[kg/s] is the mass flow rate, V[m^3] is velocity of the fluid and A[m^2] the cross section area.

2.2.3 Similarity Parameters

The aerodynamic forces depend on the compressibility of the gas. When an object is cutting through the atmosphere, the atmosphere gas molecules interacting with the object are disturbed and move around the object. Aerodynamic forces are generated between the gas and the testing object. The magnitude of these forces depend on its shape, speed and mass of the gas flowing around the object and on two other important properties of the gas, the viscosity and compressibility. To properly model these effects, aerodynamic scientists or engineers use similarity parameters, which are ratios of these effects to other forces present in the problem.

When two experiments have equal values for the similarity parameters, it means the forces are being modelled properly. Aerodynamic forces depend on Re and M. For a valid experiment, Reynolds number and Mach number must match flight conditions. Regarding the similarity parameter for viscosity, it is the Reynolds number. The Reynolds number is the relation between inertial forces to viscous forces. From the momentum conservation equation, inertial forces are written as the product of the density ρ (kg/m^3) times the velocity V (m/s) times the gradient of the velocity dV/dx. Viscous forces are identified by the product of viscosity coefficient μ with the second gradient of

the velocity d^2V/dx^2. The Reynolds number Re then becomes:

$$Re = \frac{\rho \times V \times L}{\mu} \tag{2.6}$$

When an object moves through the gas, the gas molecules move around the object. If the object passes at a low speed, its density remains constant. But for high velocities, a part of the kinetic energy of the object interacts with the fluid around by compressing the fluid and therefore, changing the density, which changes the amount of output force applied on the object. The effect becomes more apparent as speed increases. Near and beyond the speed of sound, shock waves are generated and affect the lift and drag forces of the object.

Regarding compressibility, the important similarity parameter is the Mach number (M) and it is the ratio of the velocity of the object (V) to the speed of sound (a).

$$M = \frac{V}{a} \tag{2.7}$$

The Mach number appears also as a scaling parameter in equations for compressible flows, shock waves, and expansions. At wind tunnel testing, the Mach number between the experiment and flight conditions should also be matched.

The Moody diagram is a graphic that relates the Darcy friction factor with the Reynolds number while also giving the relative roughness for a fully developed flow in a circular pipe. Following the Moody chart from Figure 2.4, Darcy friction factor is highly dependent on the flow regime.

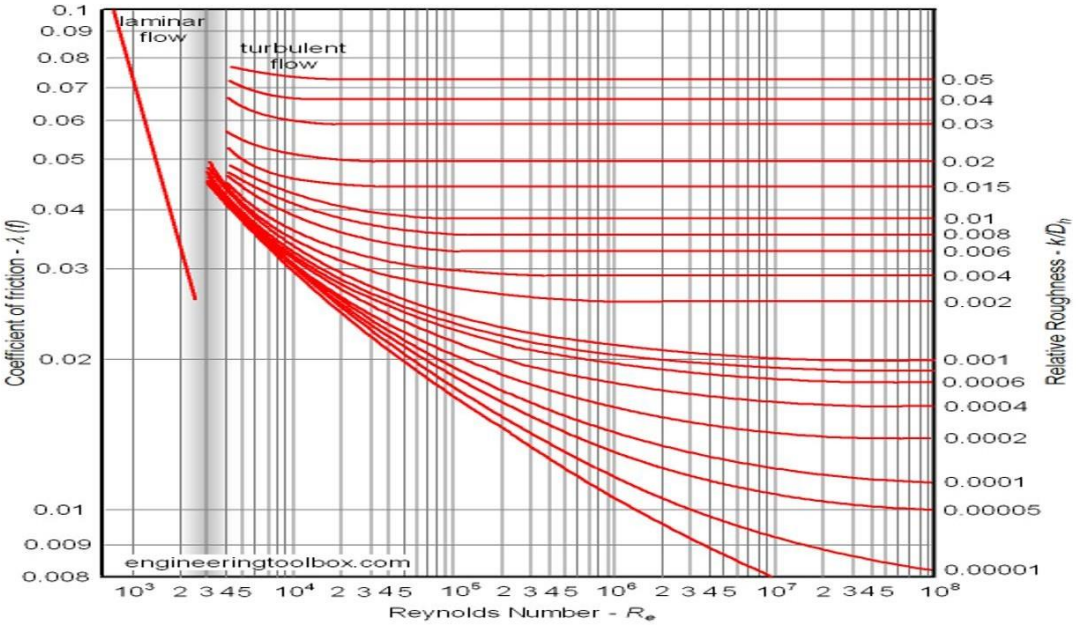

Figure 2.4: Moody Chart[16].

2.2.4 Boundary Layer

Boundary layers are regions of fluid that are located immediately adjacent to an immersed object or wall in which the flow velocities are influenced by viscous forces. Most of the heat exchange and drag forces that are experienced by the object are due to the existence of fluid in this region. Typically, boundary layers begin as a very thin region of laminar flow that thickens with increasing Reynolds number and then gradually transforms to a turbulent layer and in this region the flow becomes unsteady. Flow outside of the boundary layer is independent of Reynolds number. Figure 2.5 shows a boundary layer of a flat plate.[3]

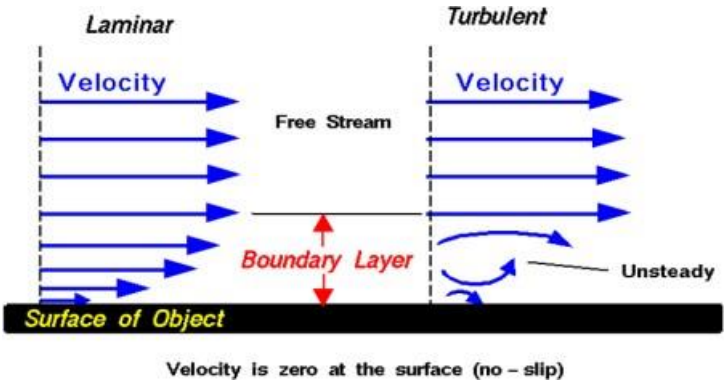

Figure 2.5: Boundary Layer[5].

Characteristics

The wall boundary layer velocity profile can be measured and fitted with power law function to find the boundary layer characteristics as displacement thickness, momentum thickness and shape factor using Simpson's 1/3 Rule for equal interval in the y-direction. These characteristics may be defined as follows:

$$\delta* = \int_0^{\delta} (1 - (\frac{U}{U_e}))\,dy \tag{2.8}$$

$$\theta = \int_0^{\delta} (1 - (\frac{U}{U_e}))(\frac{U}{U_e})\,dy \tag{2.9}$$

$$H = \frac{\delta^*}{\theta} \tag{2.10}$$

Where U/Ue is the velocity profile of the flow near the tunnel wall at specified position.

2.2.5 Boundary Layer corrections

The working models for developing wall corrections are then as indicated in Figures 2.6 and 2.7. For the closed test section case, the flow is considered inviscid and its wake is presented by a bluff body. The tunnel walls are straight and parallel. For the open test section, the flow is also considered inviscid and with the testing object and its wake presented by an equivalent body. The stream boundaries are constant pressure streamlines with the pressure equal to the ambient pressure outside the stream.[3]

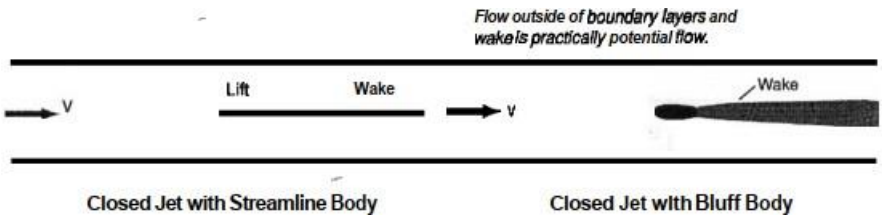

Figure 2.6: Working models for closed test section[3].

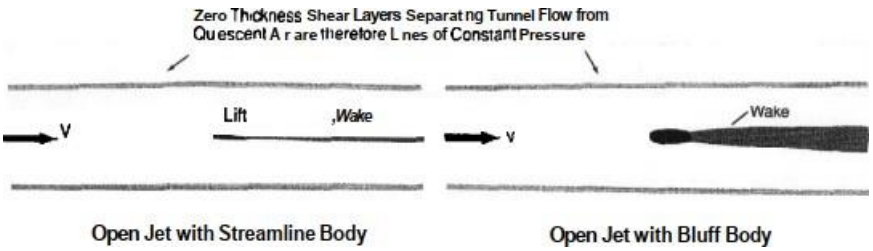

Figure 2.7: Working models for open test section[3].

2.2.6 Volumetric Flow Rate

The volumetric flow rate is the volume of fluid that passes per unit time. It may also be determined by multiplying the velocity (V) with the section's area (A_0). Once the

volumetric flow rate is constant, through Equation 2.11 relation, it is possible to estimate the flow velocity at each cross section of the wind tunnel.

$$Q = \dot{V} = \frac{dV}{dt} = V \times A_0 \tag{2.11}$$

2.3 Wind Tunnel Models

Wind tunnels may be classified organized in two categories. The first is based on the design of the wind tunnel and second is based on the air flow speed of the wind tunnel. Based on the structural design, there are two types of wind tunnel which are an open loop circuit wind tunnel and a closed loop circuit wind tunnel.

Open-Loop Circuit Wind Tunnel

An open loop circuit wind tunnel is an open design tunnel in which the air that is passed through the tunnel is collected from the air in the room where the wind tunnel is placed. The air is reused again using the surrounding air where the wind tunnel is placed. The design of an open loop wind tunnel is simpler, meaning that it is built of fewer sections compared to the closed loop wind tunnel.

The Figure 2.8 shows the basic design of an open loop wind tunnel with flow circulation. There are two types of open loop circuit wind tunnel which are (i) the suck-down and (ii) the blower wind tunnel. [3]

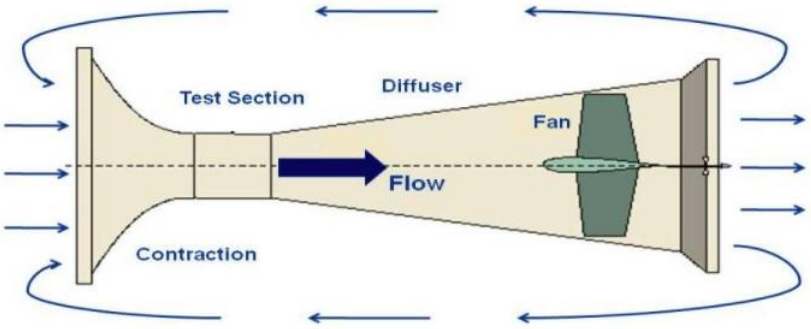

Figure 2.8: Open-Loop Circuit Wind Tunnel[18].

- (i) The Suck-Down tunnel consists on sucking the surrounding air from the test section to the fan. It is believed that the intake swirl is less problematic in the tunnel as the air doesn't pass through the fan before entering the test section .

- (ii) The blower wind tunnel operates by blowing the surrounding air towards the test section. It is more flexible as the test section can be interchanged without seriously disrupting the flow due to the location of the fan, which is placed at the inlet of the wind tunnel. The exit or diffusers can be completely removed to allow easier access to the testing object. However, this results in a noticeable power loss in the system as well as an increase at the turbulence levels of the test section.

Closed-loop circuit wind tunnel

It is a closed tube that recycles back the air that flows in the tube. The name comes from the design of the wind tunnel, in which the exhaust flow is directly returned to the inlet of the tunnel. The idea is to improve the efficiency of the wind tunnel for high speed testing by using recirculated air. The construction of a closed-loop wind tunnel is more difficult as it is larger in size compared to an open wind tunnel. Besides that, in order to ensure uniform air flow, the tunnel is tailored with specific sections carefully designed and every manufactored detail increases the cost its conception. Figure 2.9 shows the layout of a Closed-Loop Wind Tunnel[6]:

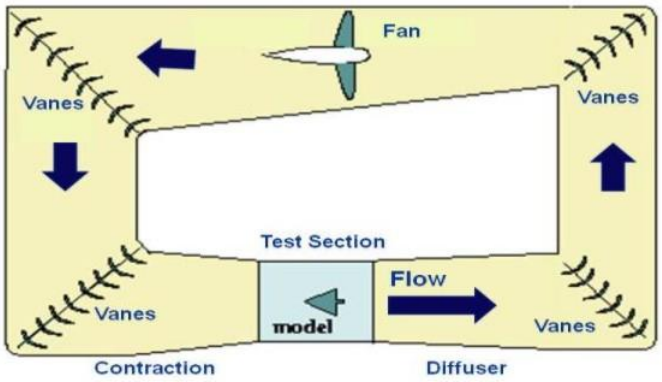

Figure 2.9: Closed-loop circuit wind tunnel [6].

There are four types of wind tunnels based on the speed of the air flow. The

next Figure 2.10, shows the classification of different types of wind tunnel based on different speed conditions.

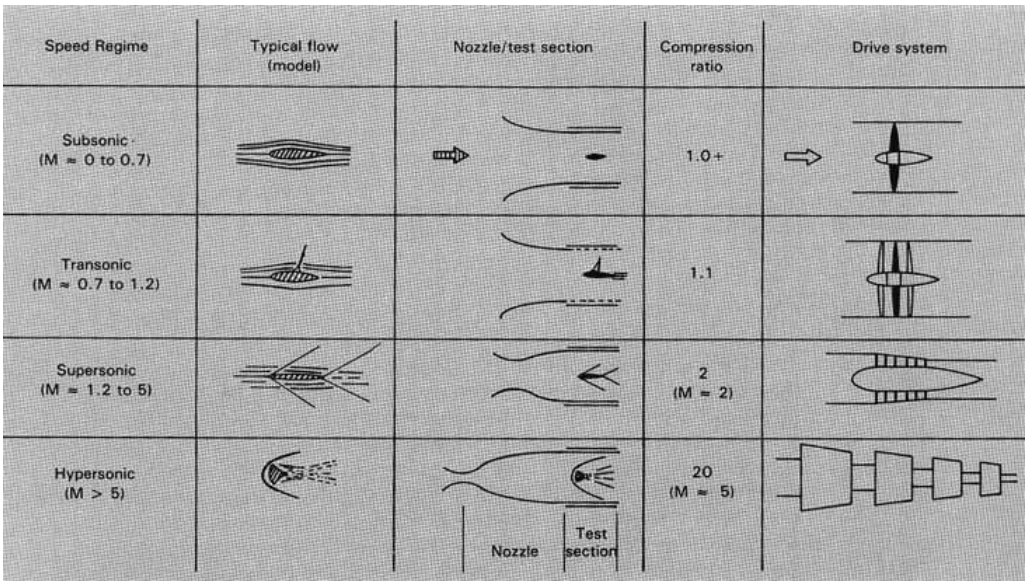

Figure 2.10: Characteristics of wind tunnels designed for the different speed regimes[3].

The nozzle or contraction cone of the supersonic test section has a unique design for each Mach number. Also, in order to achieve different Mach numbers, the contraction cone design of the supersonic wind tunnel has to be variable. This can be accomplished by flexible nozzle walls. This required change in the contraction shape makes one of the three major differences between the subsonic and supersonic wind tunnels.

The second fundamental distinction when comparing subsonic and supersonic wind tunnels is the magnitude of the energy losses in the fluid circuit. According to Barlow et Al(1999), in subsonic tunnels the fans need to increase the fluid pressure at about 10 percent in order to compensate for the energy losses induced by the tunnel walls and its models, turning vanes, and so on. However, in a Mach 2 tunnel, the fan pressure must be significantly increased by around 100 percent.

Evidently, a much larger amount of power is consumed by the big Mach 5 compressors relative to the simpler fans in subsonic tunnels. As a consequence, the flow losses around the circuit of the supersonic tunnel are also much higher for reasons associated with supersonic aerodynamics. The reason is that very large energy losses occurs

due to shock waves downstream of the test section. Once again, in order to compensate for these energy losses, the electrically driven fans or compressors must be able to supply this extra energy.

Finally, the third major difference between subsonic and supersonic tunnels involves the tunnel fluid itself. The fluid must be clean, not subjected to vapor nor dust.[3]

2.3.1 Fluid Flow

Liquid flow research is a necessary study for naval applications, for example, on designing ships, and it is widely used in civil engineering projects such as harbour design, houses foundations and even coastal protection. For centuries, scientists and researchers have studied fluid flow in various ways, and nowadays this area is still an important field of investigation. Gaseous flows are studied for the development and improvement of cars, aircrafts and spacecrafts. The design of certain machines such as combustion and turbine engines also plays a vital role in understanding and predicting the performance of gaseous flows when subjected to high temperatures. In chemistry, knowledge of fluid flow is as important for example, how the fluid behaves inside a reactor or how interacts with other chemical elements; in medicine, the flow of blood in arteries and veins is also studied. Numerous other examples could be pointed out. In the fluid flow research, being able to obtain empirical data through visualization is important and useful.

2.3.2 Description of Wind Tunnel Flow

The general occurring features from flow states in closed test sections and open jet test sections are described with streamlined bodies and bluff bodies present.

Figure 2.11 reveals sketches of closed test sections with a streamlined and a bluff body. From this figure, it is clear that there's much less volume of rotational flow, legended as "Wake", produced by the streamlined body in relation to the bluff body.

When the testing objects are mounted on a tunnel surface, there is a direct interaction of the tunnel surface boundary layer and the object's boundary layer.[3]

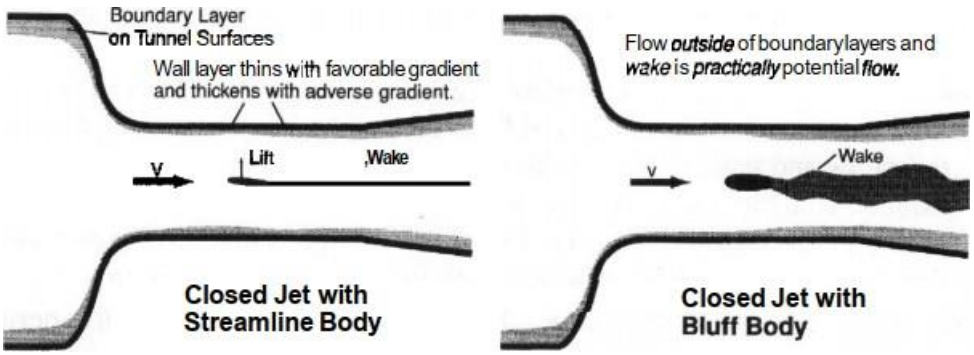

Figure 2.11: Closed test-section cases[3].

Figure 2.12 presents sketches of an open jet tunnel with a streamlined and a bluff body. Subtitled in the figure, one can see the existence of a free shear layer right at the boundary of the test section flow. That is, there is a velocity gradient due to the lack of a wall. Consecutively, there is a higher level of unsteady flow in relation to closed test sections.

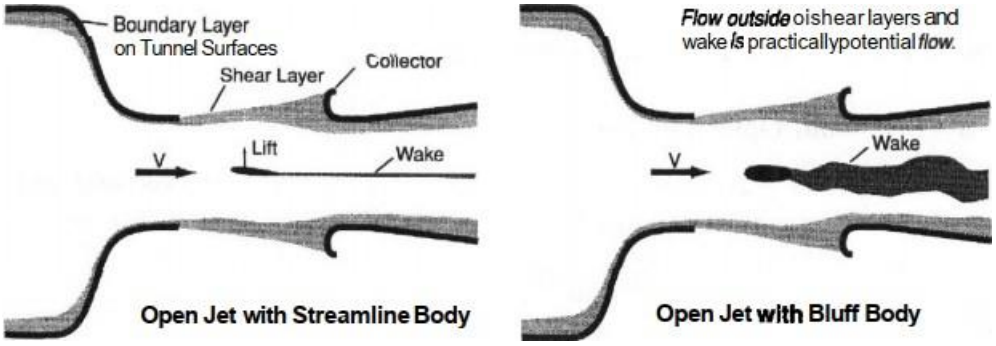

Figure 2.12: Open jet test-section cases[3].

2.3.3 Helium

Helium was discovered in 1895. Its name is originated from the ancient Greek symbology, 'helios' corresponding to the sun, as it was on the sun's corona that helium was initially observed. Helium is a two atomic gas with atomic weight of 4.002 g/mol.

Once it has almost constant thermophysical properties, it is a desirable working fluid in gas turbine cycle and also of interest in estimating cycle performance. Helium has a ratio of specific heats (at constant volume and constant pressure) called gamma coefficient $\gamma = 1.667$, and a constant specific heat (at constant pressure) $Cp = 5.194 kJ/kgK$. It is relevant to compare the values of γ and Cp to other fluids such as air. Higher value of γ gives a possibility of keeping lower pressure ratio for compression and expansion processes while having the same temperature ratio. This is responsible for power output and heat input. Equations 2.12, 2.13 and 2.14 explain this situation better.

During the compression process, as the pressure[Pa] is increased from P_1 to P_2, the temperature[K] increases from T_1 to T_2 according to this exponential equation:

$$\frac{T_2}{T_1} = \frac{P_2}{P_1}^{\frac{\gamma-1}{\gamma}} \tag{2.12}$$

where γ corresponds to the ratio of specific heats and

$$\left(\frac{\gamma-1}{\gamma}\right)_{helium} > \left(\frac{\gamma-1}{\gamma}\right)_{air} \tag{2.13}$$

Equation for estimating compression work(CW)[J/kg] can be written in a way presented below:

$$CW = Cp \times (T_{out} - T_{in}) = (ht_{out} - ht_{in}) \tag{2.14}$$

where Cp is the specific heat at constant pressure,T_{out} and T_{in},the outlet temperature and inlet temperature of the compressor respectively while ht_{out} and ht_{in} the specific stagnation enthalpy at the exit and entrance of the compressor respectively.

Considering that the temperature ratio remains the same for both cases, it is now clear that pressure ratio can be lower for helium while the process of compression work is also less intense due to its light molecular weight in comparison to air. Another point is that helium has relatively high specific heat, about 5.2 kJ/kgK. So, when comparing the power output considering the same temperature ratio, helium gives about 5 times

more power output per unit mass flow, compared to air which has specific heat at the level of 1 kJ/kgK. On the other hand, it enables a simpler design of the compact heat exchangers once heat exchange can be relatively high for lower temperature difference, in relation to other fluids with lower specifics heats.

Also, once helium has a lower molecular weight of 4 kg/kmol comparing to 29 kg/kmol for air which indicates that density is lower, it could be a problem for open cycle gas turbines since there are some limits due to mechanical aspects on turbomachinery dimensions as lower density would result in lower mass flow and in lower power output. In order to raise it to reasonable levels, Turbine Inlet Temperature should be raised which would raise materials considerations and consecutively the costs.[10]

2.4 Elementary Cascade Theory

The study and development of flow on the two dimensional perspective through a cascade of aerofoils has played a vital part into the development of a highly efficient modern axial flow turbine or compressor. A cascade is an array of blades that represent a blade ring from an actual turbo machinery compressor or turbine.

Figure 2.13 shows a compressor blade cascade tunnel. As the air flow passes through the cascade, at up and downstream of the cascade, the air direction turns. So the pressure and velocity are measured in these two points of the cascade. The cascade is mounted on a turntable so that its angular direction relative to the direction of inflow can be changed, which enables tests to be made for a range of incidence angles(i).[13]

As the flow passes through the cascade, it is deflected and there will be a circulation Γ and thus the lift generated is shown on Equation 2.15. where V_m is the mean velocity that makes an angle α_m with the axial direction. Following Figure 2.14, C is the chord of the blade and S the pitch.

$$\Gamma = S(V_{w1} - V_{w2}) \tag{2.15}$$

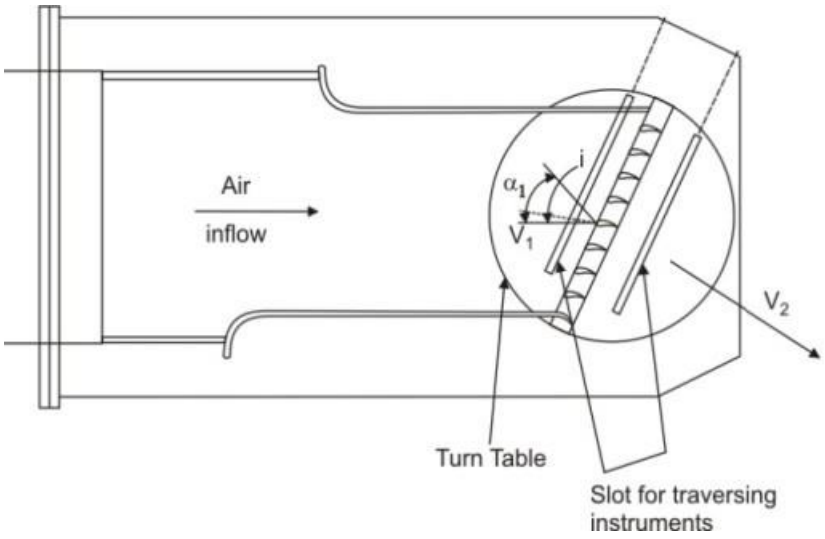

Figure 2.13: Cascade Tunnel[13].

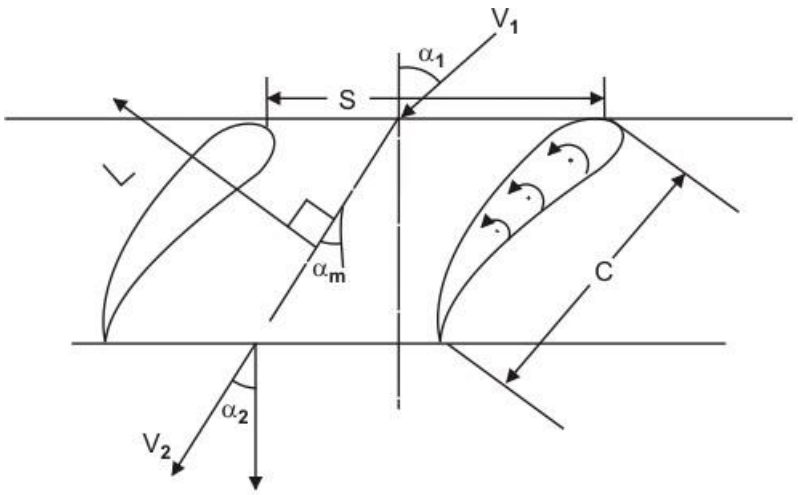

Figure 2.14: Compressor Cascade[13].

$$Lift = \rho V_m \Gamma \tag{2.16}$$

From the Figures 2.15, Equations 2.17, 2.18 and 2.19 are estimated.[13]

$$V_{w1} = V_f tan(\alpha_1) \tag{2.17}$$

$$V_{w2} = V_f tan(\alpha_2) \tag{2.18}$$

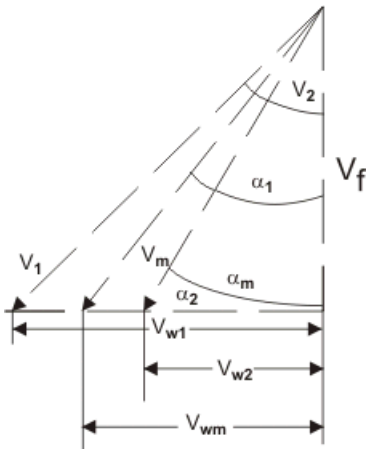

Figure 2.15: Velocity Triangle[13].

$$C_L = 2\frac{S}{C}\left(\frac{V_f}{V_m}\right)(tan(\alpha_1) - tan(\alpha_2)) \tag{2.19}$$

2.5 Early Cascade Experiments

2.5.1 Experimental study of flow through compressor Cascade

In their research work, Panchala and Mayavanshi (2017) aimed to study the behaviour of flow at the inlet, within the blade passage and at the exit of a compressor cascade through a wind tunnel, see Figure 2.16.

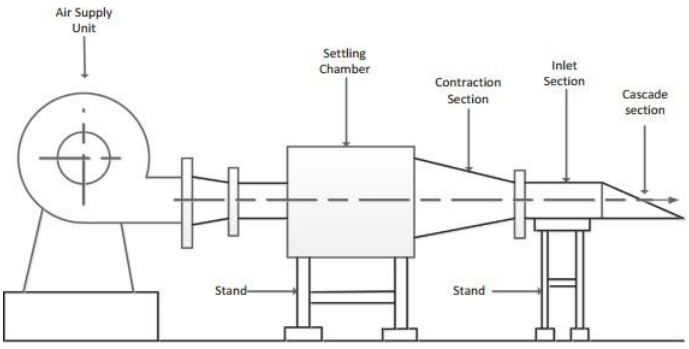

Figure 2.16: Schematic of experimental setup [20].

The blades for the test cascade were tested at low Mach number, 0.20–0.30, based on mean flow conditions relative to the rotor. The parameters for the test blades are

presented in Table 2.3. The cascade consists on seven blades and is shown in Fig:2.17.

Figure 2.17: Cascade Assembly [20].

Table 2.3: Parameters of the test blades[20].

Item	value
Camber line	Parabolic
Base profile	C4
Position of maximum camber	40% of chord length from leading edge of the blade
Chord length	80 mm
Height of the blade	160 mm
Camber angle (Deflection)	45°
Stagger angle	30°

The summary of the tests made on the cascade are on the following list[20]:

1. The flow parameters were less affected by the incidence at the far upstream of the cascade;

2. The flow parameters and flow directions upstream of the cascade were affected by the incidence;

3. Following a high negative incidence, comes a greater disturbance on the flow conditions within the passage of the cascade. The disturbances were very high near the pressure surface. On the other hand, with positive incidence, the disturbance decreased near to the pressure surface;

4. At the region near to the suction surface, there were no disturbances with any incidences;

5. The pressure distributions along the surfaces were affected by the flow incidence. The effect of incidence was greater on the pressure surface. Whilst on suction surface, it was observed a continuous deceleration at higher negative incidence;

6. The effect of incidence failed at roughly about 50 of the axial chord on the suction surface;

7. The pressure surface side developed a wake compared to the suction surface side. The magnitude of the wake was very high at –50° incidence. And by increasing the incidence, the wake was reduced.

2.5.2 Incompressible Cascade Flow

On Schlichting's (1957) two-dimensional cascades project, the main purpose of the investigations was to estimate theoretically the loss coefficients of the cascade. This was accomplished by applying boundary layer theory to the cascade flow. Figures 2.18 and 2.19 show some examples of the loss coefficient plotted against the dimensionless deflection.

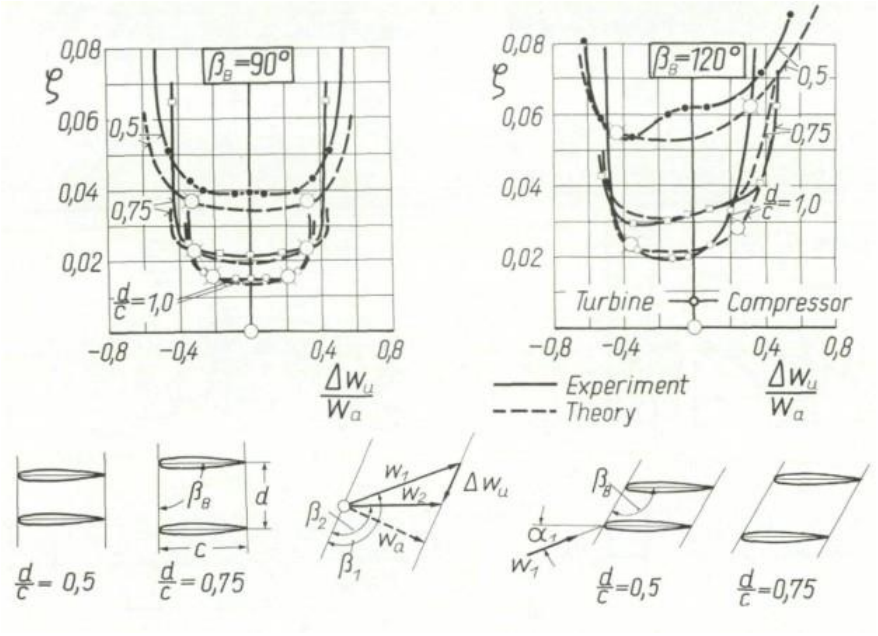

Figure 2.18: Loss coefficient ζ for cascades of various solidity ratios d/c and various blade angles β ; blade section NACA 0010; Reynolds number R2 = 5x10e5, fully turbulent boundary layer The circles with projected lines on the theoretical curves indicate the beginning of separation[22].

Theoretically, it has been assumed fully turbulent flow in the boundary layer, and pratically this was achieved by a turbulence wire near to the leading edge of the blade. The results of Figure 2.18 are for cascades of blades with the symmetrical profile NACA 0010, whereas in Figure 2.19 the blades have the cambered profile NACA 8410. In both cases, the solidity ratio d/c and the blade angle have been varied.

The agreement between theory and experiment is very satisfactory. These results on two-dimensional cascades have finally allowed the theoretical determination of the characteristic curves of an axial flow compressor. The example of this kind of estimations is given in Figure 2.20 and Figure 2.21. In Figure 2.20 the blade angles the velocity vectors at different cross sections are given. Figure 2.21 shows the pressure coefficient $\psi = 2 * gH/u_A$ and the efficiency coefficient for the single-stage compressor plotted against the flow coefficient $\Phi = V/(\pi r_A^2 u_A)$.

The overall shape of the curves agrees with what is expected.[22]

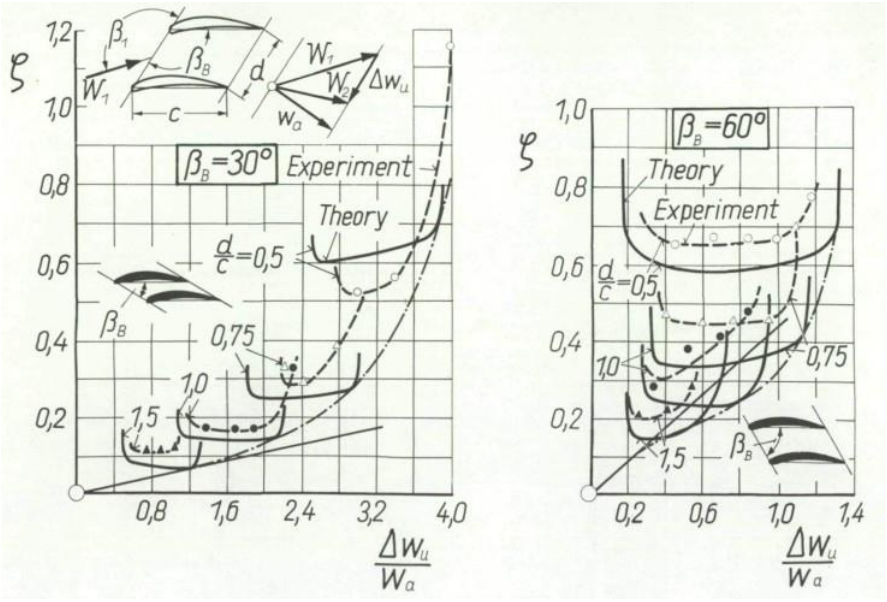

Figure 2.19: Loss coefficients ζ of turbine cascades of various solidity ratios d/c and various blade angles β; blade section NACA 8410: Reynolds number R20= 5x10e5[22].

	Section I (Tip)	Section II	Section III	Section IV (Hub)
r/r_h	1,0	0,85	0,7	0,55
d/c	1,30	1,11	0,91	0,71
β_B	131°	121°	113°	106°
$\Delta c_u/c_m$	0,575	0,547	0,589	0,695
	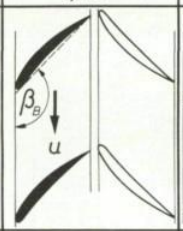		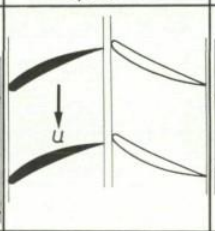	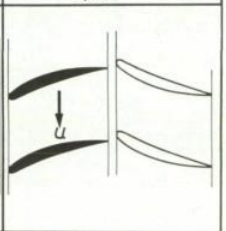
	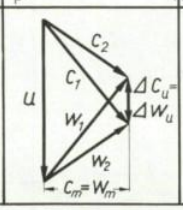	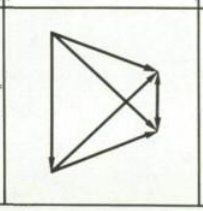	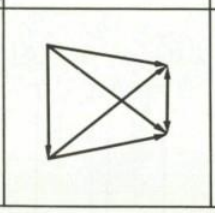	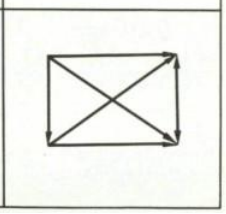

Figure 2.20: Blade sections of the single-stage axial flow compressor of Figure 4[22].

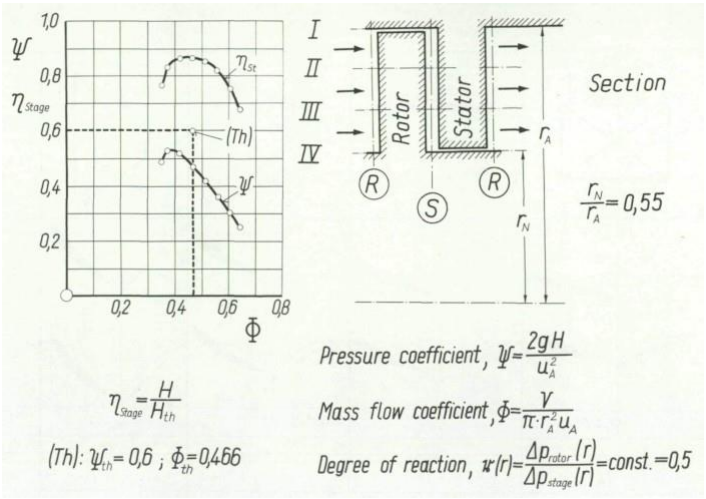

Figure 2.21: Characteristic curves of a single-stage axial flow compressor, as calculated theoretically from cascade data, by N. Scholz. Pressure coefficient and efficiency coefficient against mass flow coefficient.

2.5.3 Compressible Cascade Flow

Scholz and Grewe (1957) performed the tests regarding the compressible cascade flow on cascade blades at high subsonic speeds. The Mach number range varies from $M = 0.2$ to 1.1. The blade length $I = 300$ mm and the blade chord $c = 60mm$. Figures 2.22 and 2.23 present the cascade.

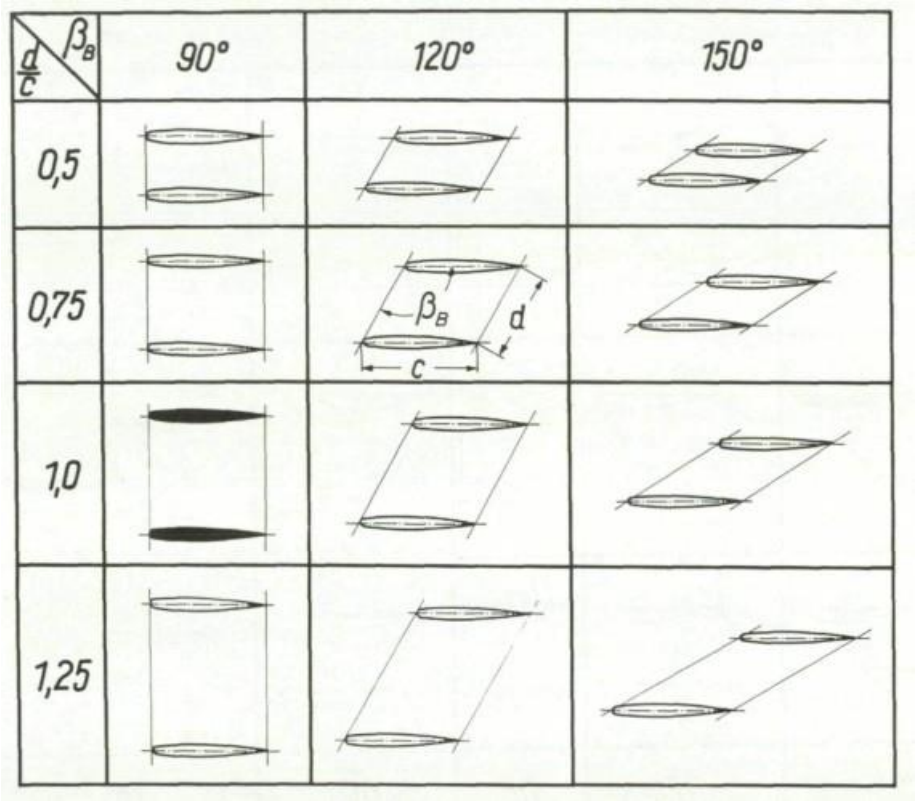

Figure 2.22: Cascade geometry for pressure distribution measurements in the High Speed Cascade Wind Tunnel; blade section NACA 0010[22].

The cascade geometry and the blade profile are from the study of incompressible cascade flow. The pressure measurements of the cascades were made considering different angles of inflow and with the Mach number varying from $M = 0.2$ to the choking Mach number. A special feature of the used wind tunnel is that both Mach number and Reynolds number may change independently. In this case, the Reynolds number is constant over the changing of Mach number, $R2 = w2c/v = 3x10^5$. The results given refer to the three cascades marked in solid black in Figures 2.22 and 2.23.

Following Figure 2.24 the cascade is unstaggered and its blades have a NACA

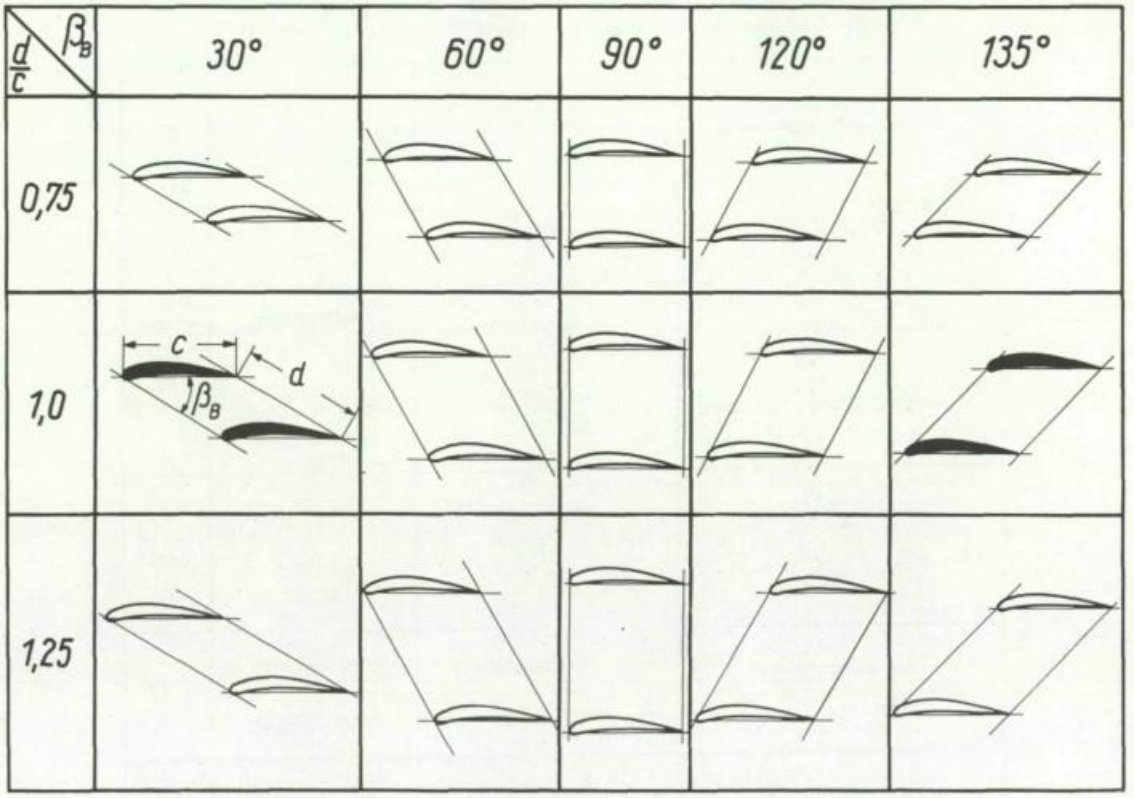

Figure 2.23: Cascade geometry for pressure distribution measurements in the High Speed Cascade Wind Tunnel; blade section NACA 8410[22].

0010 profile. The flow reaches the cascade with an angle $\beta_1 = 90°$, for the first bracket and $\beta_1 = 100°$ on the second. With increasing Mach number the pressure distribution remains quite normal up to about $M_1 = 0.65$. For $\beta_1 = 100°$ and $M_1 = 0.65$ a shock wave appears on the suction side of the blade. With $M_1 = 0.69$ choking has occurred, and the mass flow rate is limited. As the result of choking, the pressure distribution changes completely, following Figure 2.24 for $M_1 = 0.69$. This is accompanied by a sudden increase of the pressure difference across the cascade, $P_1 - P_2$.

From Figure 2.25, similar results are presented for a compressor cascade of blade profile NACA 8410 and blade angle $\beta_{Blade} = 135°$. The pressure distribution doesn't change its form up to $M_1 = 0.7$. The choking Mach number is different for the two angles of inflow. For $M_1 = 0.75$, it is $\beta_1 = 142°$, but for $M_1 = 0.90$ it is $\beta_1 = 148°$. Considering the big amount of stagger, the increase of the pressure drop through the cascade is not as steady in relation to an unstaggered cascade.

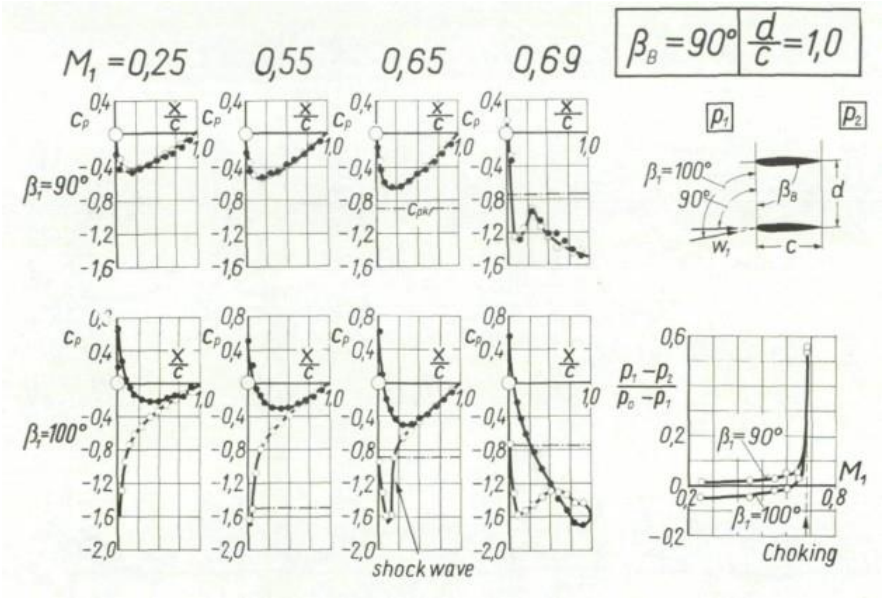

Figure 2.24: Pressure distribution measurements of cascades in compressible flow; blade section NACA 0010; Reynolds number R, = $W.C/TO$ = 3x10e5; see Figure 2.22[22].

Following Figure 2.26, some results for a turbine cascade are presented, the blade angle being $\beta_{Blade} = 45°$ and the blade profile the same. The change of the pressure distribution, when reaching the choking Mach number, isn't so significant comparing to the compressor cascade. This must be credited to the favourable pressure gradient of the turbine cascade.

Finally, from Figure 2.27, the empirical results of Figure 2.24 for the unstaggered cascade of NACA 0010 profile are compared to theoretical calculations. For high subsonic Mach numbers, the compressibility effect on the pressure distribution is significant. The Mach numbers where no shock waves occur, there is a satisfactory agreement of the theoretical and experimental pressure distributions.[22]

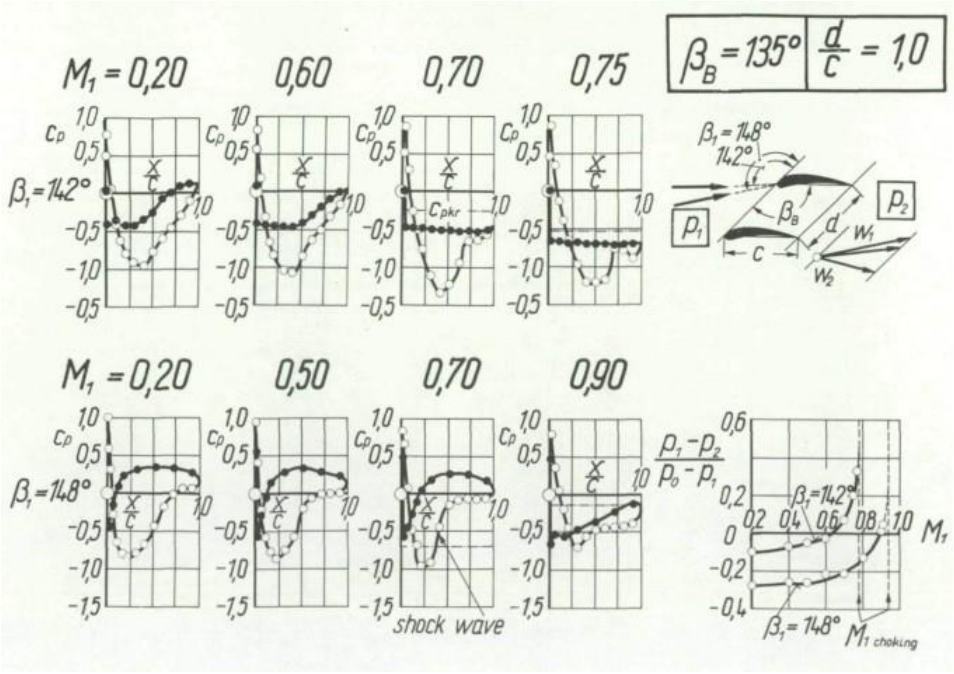

Figure 2.25: Pressure distribution measurements of compressor cascades in compressible flow;blade section NACA 8410; Reynold number R2 = w^2c/v = 3xl0e5;see Figure 2.23[22].

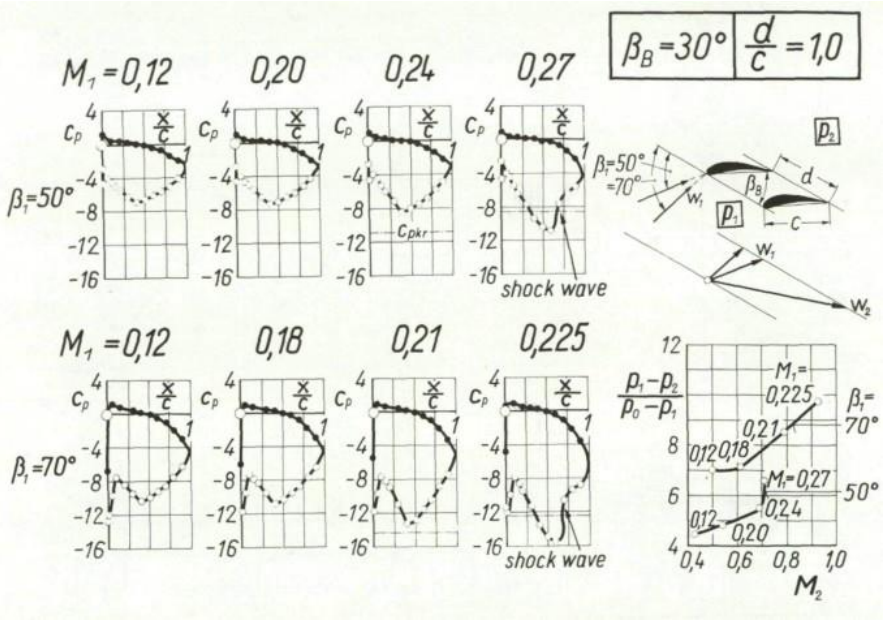

Figure 2.26: Pressure distribution measurements of turbine cascades in compressible flow; blade section NACA 8410; Reynolds number R2 = w2c/v = 5xl0e5; see Figure 2.23[22].

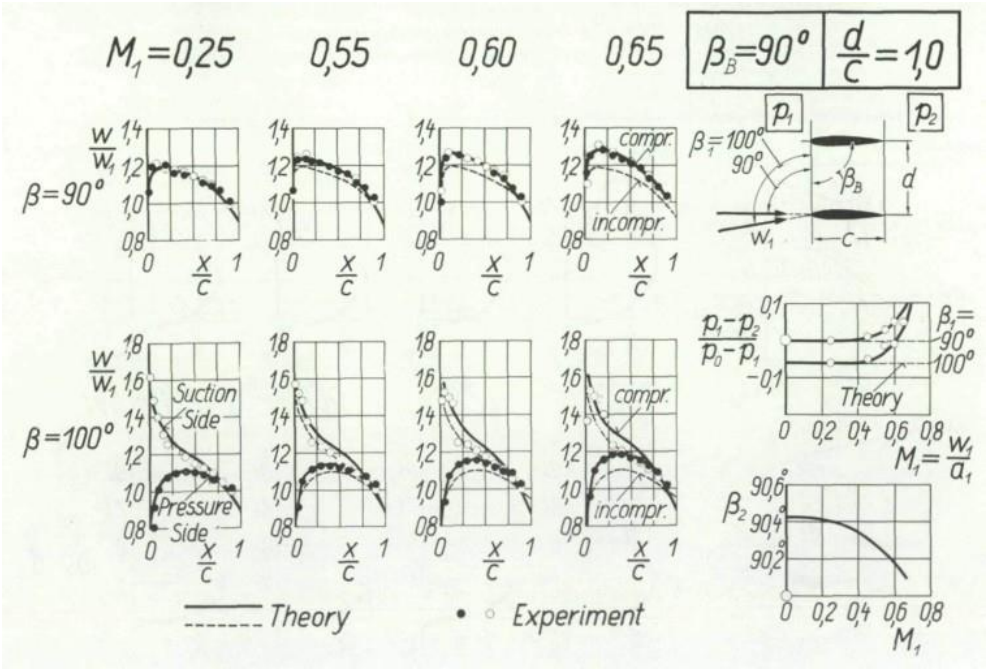

Figure 2.27: Comparison of theoretical and experimental velocity distribution of cascades in compressible flow. Theory from Prandtl-Glauert rule; experiments, see Figure 2.24. Blade section NACA 0010; Reynolds number R = wc/ν = 3xl0e5[22].

2.6 Instrumentation and Calibration of the Test Section

2.6.1 Forces and Moments

The objective of measuring loads on the model is to reveal the forces and moments so that they may be corrected for tunnel boundary and scale effects and also utilized in a way the performance of the full scale vehicle or other device is predicted.

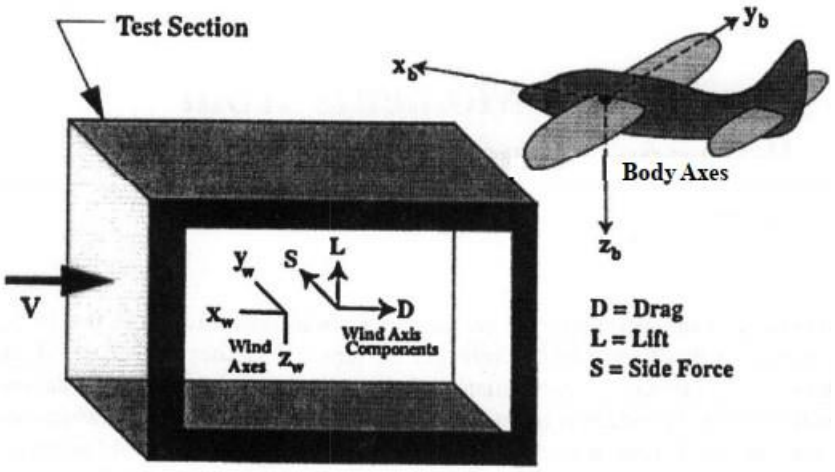

Figure 2.28: Wind and body reference frames [3].

The moment components on the x, y, z axes are referred to as rolling moment, pitching moment, and yawing moment, respectively. Following Figure 2.28, the conventions for the positive aerodynamic force components (L,S and D) are not in the positive directions for the axes (x,y and z). For a wind tunnel. the lift (L) and drag (D) are aerodynamic forces because they exist due to the flow of the fluid through the testing object. The weight pulls down on the object opposing the lift created by the fluid flowing over the object.

$$L = \frac{1}{2} C_L \rho V^2 A \tag{2.20}$$

$$D = \frac{1}{2} C_D \rho V^2 A \tag{2.21}$$

2.6.2 Manometers

A manometer is a device that indicates the pressure difference between two points by the offset in height of a liquid, usually in a “U” shaped tube. Pictured below are two types of manometers. Both of these must be in the vertical position to produce accurate readings.

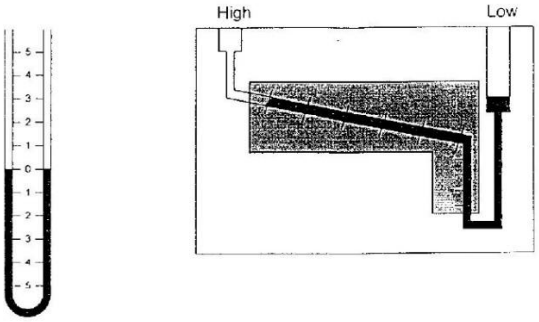

Figure 2.29: Manometer[8].

The difference in pressure (δp) is related to the height difference in the liquid by

$$\delta p = p_1 - p_2 = \Delta h \sin\beta g(p_f - p_a) \tag{2.22}$$

where Δh is the height difference, β the fluid angle from the second figure from Fig.2.29 and p_f and p_a the pressure from the highest point and lowest point, respectively, as expressed in the Figure.

2.6.3 The Pitot Tube

Pitot tube is a measurement device which can measure static pressure and total pressure. After that, the dynamic pressure can be obtained through estimation. In Figure 2.30, the total pressure is measured at the stagnant point in the flow direction, and the static pressure is measured at openings parallel to the flow.

The measurement of pressure consists in involving a small bore tube to the stream that’s being measured, either bent so that its mouth faces upstream, or a radial hole in its wall, so arranged that it also faces upstream.

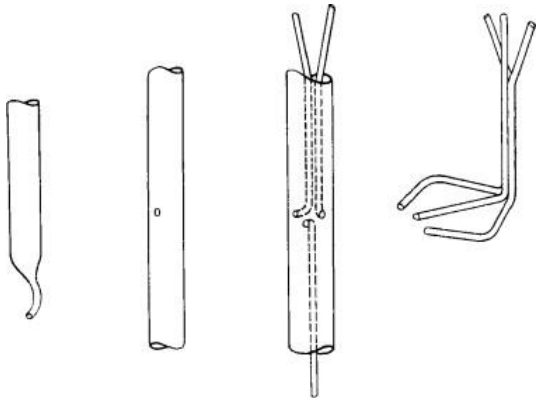

Figure 2.30: Types of pitot tube [8].

2.7 Pressure Losses and Turbulence Reduction Estimate

At this section, the pressure losses equations that were used in the project are presented. The pressure loss coefficient is important to find the power required by the fan to compensate for pressure loss in the wind tunnel. Without the pressure loss coefficient, the power calculation will not be accurate. For this dissertation, it is identified that there are seven components of a closed- loop wind tunnel.

2.7.1 Test Section

It is relevant to determine the pressure loss from the walls at the test section. The Equation 2.23 estimates the loss coefficient for a constant area section. This is given by[12]:

$$K_D = f \frac{L}{D_H} \tag{2.23}$$

where D_H[m] is the hydraulic diameter and the friction factor f just like K_D is dimensionless,

Compressor Cascade

Next, follows the estimation of the test section's object of study pressure loss coefficient. Figure 2.31 shows a portion of an isolated blade cascade (for a compressor).

The forces X and Y are applied per unit depth of blade upon the fluid and are equal and opposite to the forces pressured by the fluid upon unit depth of blade. A control surface is drawn with end boundaries far upstream and downstream of the cascade and with side boundaries coinciding with the median stream lines.[17] Assuming incompressible flow

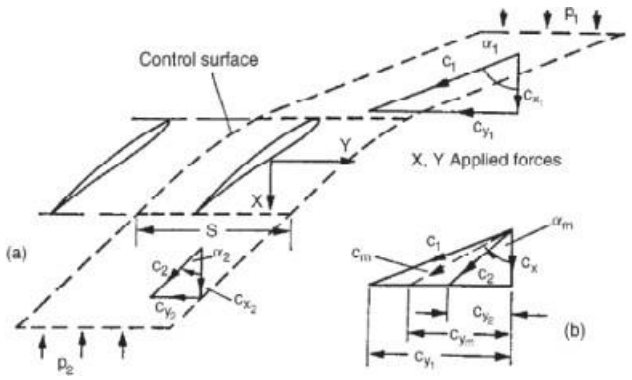

Figure 2.31: Forces and velocities in a blade cascade[17].

and applying equation of continuity to a unit depth of span yields:

$$c_1 cos(\alpha_1) = c_2 cos(\alpha_2) = c_x \tag{2.24}$$

The total pressure loss coefficient can be defined as

$$\zeta = \Delta P_0 / (\frac{1}{2} \rho \times c_x^2) \tag{2.25}$$

2.7.2 Diffuser

K_D is the coefficient pressure loss of a diffuser that is the sum of two losses which is K_f friction due to wall friction and K_{ex}, expansion losses as shown in[11]

$$K_f = (1 - \frac{1}{A_R})(\frac{f}{8 sin\theta}) \tag{2.26}$$

where θ is the semi-angle of expansion and

$$K_{ex} = K_{e(\theta)}\left(\frac{A_R - 1}{A_R}\right) \tag{2.27}$$

and A_R the entrance and exit area ratio of the diffuser and

$$K_{e(\theta)} = \begin{cases} 0.09623 - 0.004152\theta & \text{for } 0^\circ < \theta < 1.5^\circ \\ -0.1222 - 0.04590\theta + 0.02203\theta^2 + 0.003269\theta^3 - 0.0006145\theta^4 - & \\ \quad -0.00002800\theta^5 + 0.00002337\theta^6 & \text{for} 1.5^\circ \leq \theta \leq 5^\circ \\ 0.01322 + 0.05866\theta & \text{for } 5^\circ > \theta \end{cases} \tag{2.28}$$

$$K_D = K_f + K_{ex} \tag{2.29}$$

2.7.3 Corner

For closed circuit wind tunnels, corners are equipped with turning vanes to reduce losses. These vanes can vary in geometry and chord to gap ratio. There is an estimation for the loss coefficient of a corner as[12]

$$K_{corner} = \left(0.10 + \frac{4.55}{\log(Re)^{2.58}}\right)\frac{D_0^4}{D^4} \tag{2.30}$$

where: D_0 =jet equivalent diameter, D =local tunnel equivalent diameter

2.7.4 Power Fan

The drag produced by the shape of the nacelle and tail are estimated through the measurement showed that at higher velocities the magnitude of the resistance force is directly proportional with to the square of the relative velocity of the body times the density and half of the cross section area. For the magnitude of the aerodynamic drag

force (D) acting on bodies of any shape, Newton derived the relation:

$$D = \frac{1}{2} C_d \rho S v^2 \tag{2.31}$$

where C_d is the coefficient of resistance (depends on the shape of the body, see Figure 2.32), fluid density (ρ) and cross section area (S) of the body perpendicular to direction of movement and the magnitude of the relative velocity. Pressure (Pa) equals to

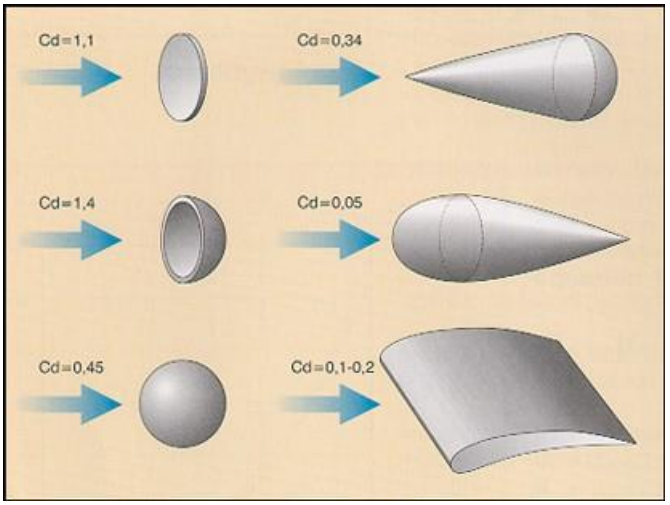

Figure 2.32: Values of the resistance coefficient C for different shapes of bodies[7].

the perpendicular force (N) divided by its area (m^2 that is subjected to the force.

$$P = \frac{F}{A} \tag{2.32}$$

Considering the Equations 2.31 and 2.32 plus the equation 2.23 for a constant area section, the pressure loss at the power section may be determined.

2.7.5 Honeycomb and Screens

Some of the turbulence theories are based on a pressure loss coefficient K. This coefficient is defined as the ratio of pressure loss across the screen ΔP over the mean

flow dynamic pressure q. This pressure loss coefficient is equal to[3]:

$$K = K_0 + \frac{55.2}{R_d} \tag{2.33}$$

with,

$$K_0 = \left(\frac{1 - 0.95\beta}{0.95\beta}\right)^2 \tag{2.34}$$

and

$$\beta = \left(1 - \frac{d}{M}\right)^2 \tag{2.35}$$

where β represents the porosity, d is the wire diameter and M the mesh width.

2.7.6 Contraction

K_c is defined as the pressure loss coefficient at contraction cone. The loss in contraction cone is considered only due to the skin friction and it is estimated as follows[3]:

$$K_c = 0.32 * f_{average} * \frac{L_c}{D_{hc}} \tag{2.36}$$

Where $f_{average}$ is the average friction factor, D_{hc} the length of the contraction cone and L_c the hydraulic diameter of the exit of the contraction cone. The average friction factor is evaluated at the inlet and the outlet of the contraction cone which is expressed in Equation 2.37. Both friction factor for contraction cone (f_c) and friction factor at test section (f_{ts}) can be calculated from the Darcy friction factor shown in Equation 2.36.

$$f_{average} = \frac{f_{ts} + f_c}{2} \tag{2.37}$$

2.7.7 Energy Ratio

The energy ratio (E_R) as defined by Equation 2.38 is expressed in terms of the

sum of the loss coefficients from the various wind tunnel sections.

$$E_R = \frac{1}{\Sigma K_i} \tag{2.38}$$

This definition of energy ratio excludes the energy losses associated with the fan and the engine. The energy ratio for close wind tunnels and open circuit tunnels other than free-jet facilities is nearly always greater than unity. Its typical range is from 3 to 7 for closed throat tunnels.[3]

Chapter 3

Wind Tunnel Design Methodology

Wind tunnel design is an iterative process where research goals are first set, which then establish the design criteria. Typically, the wind tunnel design involves constraints such as cost, fabrication and it is subjected to facility space limitations among other conflicting constraints. This chapter presents the estimation methods and guidelines behind each component dimensioning. Some of the figures provided in this chapter are designed by the author.

3.1 Design Criteria

Wind tunnel are designed and built for a purpose. They should be suitable to meet the specific research goals. In this case, due to the size of the test cells earmarked for this facility, the wind tunnel had to be designed with a maximum length of 14 m and a maximum width of 9 m. The larger the dimensions means higher the cost and bearing in mind that the working fluid is helium, the budget is already expected to be high. The design of the wind tunnel should be feasible and acceptable while maintaining a reasonable construction cost.

3.2 Test Section

The first step in the design of a wind tunnel is to determine the size and shape of the test section. This choice depends on the intended uses of the facility and, as will be discussed, is intrinsically linked to financial resources available to build the equipment and in this case, the cascade design.

A rectangular shape is recommended for aeronautical applications. In the case of three-dimensional testing ojects, the common width to height ratio is 4:3; however, for the tests that are two-dimensional it is advised a 2:5 ratio. This should enable the boundary layer thickness in the test section to be much smaller than the model span.[3]

3.2.1 Cascade

A blade-testing wind tunnel must enable the engineer to apply to groups, or cascades of blades of any construction air or other fluid under controlled two-dimensional flow conditions in such a way that he can measure and vary its attack and discharge directions, and observe the pressure and velocity changes occurred in its passage through the cascade. The variables involved are illustrated in Figure 3.1.

3.2.2 Similarity Parameter

The key parameters such as velocity, blade span and chord, number of rotor and stator blades, Reynolds and Mach number, for this wind tunnel's cascade design were based on GTHTR300C cascade design. Targeting a Reynolds number of 100,000 while considering the chord of 0.107 m, through Yan et al.(2003) research, and the properties of helium at standard atmospheric pressure ISA, the velocity was obtained (106.9 m/s).

These values set the cascade design aim, meaning that a Reynolds number and chord at the test section would be chosen and estimated so that the Reynolds number wouldn't be lower than 100,000 and the chord equal or higher to 0.107 m while testing at a speed of 100 m/s .

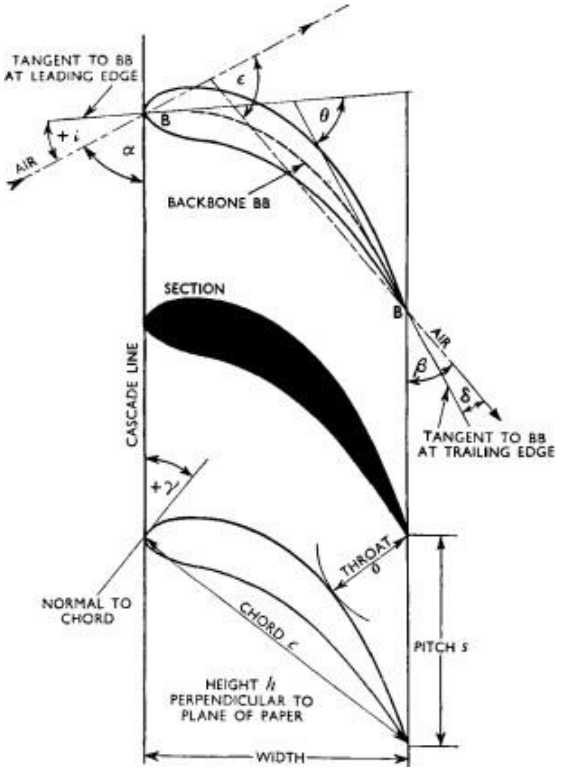

Figure 3.1: Cascade notation: Θ =camber, Γ =stagger, i =incidence, ε =deflexion, δ =deviation, α =air inlet angle, β =air efflux angle[25].

3.2.3 Cascade limitations

While designing a cascade, its limitations should also be considered. Curvilinear and coriolis effects are discarded. The coriolis effect is an inertial force that is applied on objects in motion within a frame of reference which rotates with respect to an inertial frame. So the object may appear to be moving through a curved line when in fact it is a straight line, for example. Other cascade limitations are as follow[3]:

1. Predominantly a cold flow test method;

2. Offers no information on three dimensional flow structure;

3. A very difficult process while applied to radial flow machines;

4. May be an expensive experiment;

3.2.4 Design

Figure 3.2 represents the schematics of the cascade design. The cascade is set on a rotative disk also known as turntable.

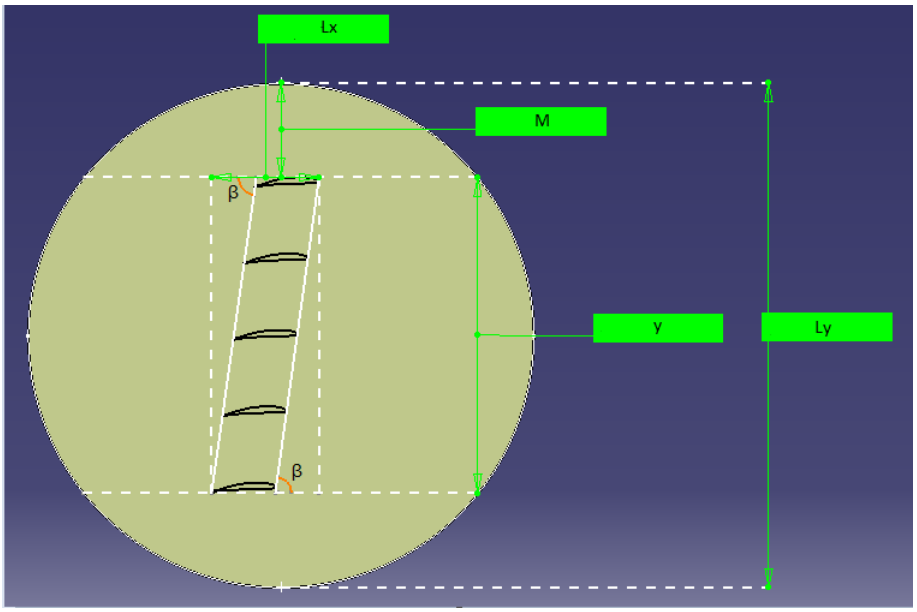

Figure 3.2: Schematics of cascade design.

The vertical length of the turntable cascade L_y is estimated as

$$L_y = y + 0.01 \times 2 \times M \times y \tag{3.1}$$

where M represents the margin of the boundaries of the disk and the space between blades is determined through

$$s_y = \frac{s}{c} \times c \tag{3.2}$$

while the horizontal length of the cascade as

$$L_x = c + \frac{y}{tg(\beta)} \tag{3.3}$$

where n is the number of blades, t the blade thickness, c the chord and s the space between vanes. All the paremeters are in meters.

3.3 The Diffuser

The inlet cross-section area and shape of the first diffuser are known because they are equal to the cross-section area and shape of the testing chamber. This diffuser has a fundamental role in the test chamber flow quality because the fluid enters with almost its maximum velocity and the first diffuser expands the fluid and very significantly decreases its velocity. In case of flow detachment, the pressure pulsation is transmitted upstream into the test chamber, resulting in pressure and pressure disturbances generated in the first corner. In order to design a diffuser, the semi-angle parameter($\frac{\alpha}{2}$) must be set. Applying trigonometry relations on the diffuser(see equations 3.4, 3.5 and 3.6, the inlet and outlet widths and Length(L) of the diffuser may be determined.

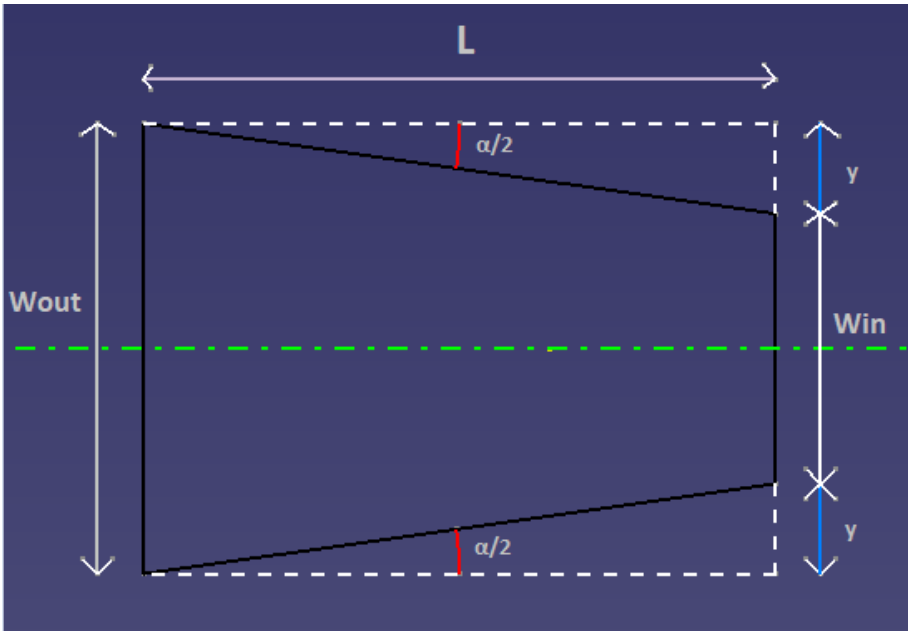

Figure 3.3: Schematics of the diffuser's expansion parameters(adopted from [3]).

$$tan(\frac{\alpha}{2}) = \frac{y}{L} \tag{3.4}$$

$$y = \frac{W_{outlet} - W_{inlet}}{2} \tag{3.5}$$

$$W_{outlet} = W_{inlet} + 2Ltan(\frac{\alpha}{2}) \tag{3.6}$$

Where W_{inlet} and W_{outlet} are the width of the diffuser entrance and exit, respectively, and α the diffuser semi.angle. For a non square cross-section, a and b are, respectively,the width and height of the cross-section, the hydraulic diameter is considered and is determined as

$$D_H = \frac{2ab}{a+b} \tag{3.7}$$

3.4 Corner Ducts

The corner ducts of a closed-circuit wind tunnel need careful attention because they have the vital task of turning the flow by 90° while minimizing the secondary flow. This secondary flows are cross flows superimposed on the longitudinal flow. The corners may not have expansion angles, so it means the inlet dimensions are also the outlet dimensions($W_{ent} = W_{exit}$).

As described on Figure(3.4), the width and the height at the entrance, W_{ent} and H_{ent} respectively, are given by the previous cross-section diffuser exit dimension. The height at the exit, H_{exit}, should be the same as at the entrance, but the width at the exit, W_{exit}, may be increased, giving the corner duct an expansion ratio, W_{exit}/W_{ent}. According to Barlow et Al(1999), this parameter may have positive effects on the pressure loss coefficient when the ratio is approximately 1,1 . However, it is not typical for corners to have expansion ratios, so it must be designed considering certain geometrical constraints or factors.

The corner radius is normally proportional to the width at the corner entrance. When the corner radius increases, it reduces the pressure loss due to the pressure distribution on corner vanes but also increases the pressure losses due to friction as well as the overall wind tunnel dimensions. It is recommended to use 0,25 W_{ent} as the value of the non dimensional radius for corners 1 and 2, and 0,20 W_{ent} for the other two corners.[9]

The extrance and exit length may be determined through

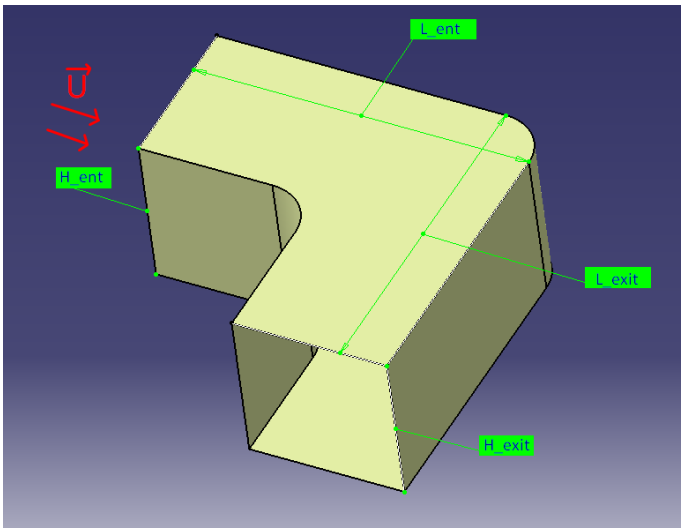

Figure 3.4: Description of the corner duct.

$$L_{ent} = W_{ent} + W_{ext} \times Ncornerradius \tag{3.8}$$

$$L_{exit} = W_{ent} \times (1 + Ncornerradius) \tag{3.9}$$

3.4.1 Turning Vanes

The most challenging flow turnings are the first two following the test section accounting the high flow velocities. In order to avoid great losses and to preserve relatively straight flow throughout the duct circuit, turning vanes will be placed at the four corner ducts of the tunnel. The corner radius will be the same for the respective corner vanes radius.

The type of vane chosen is a curved plate instead of airfoil blades. This is chosen for two reasons. First, the cost to make airfoil blades for the tunnel will increase the construction cost. The second reason is that this corner vane tests were made and proved that cambered airfoil blades presents a higher pressure loss than curved plates. To make sure this is right, when researching at recorded data from previous tests and

experiments, the amount of loss that is recovered from an airfoil instead of a curved plate is about 4%. [3]. On the other hand, curved plates are also simpler form for design and flow estimations.

In order to determine the number of vanes to be used, a initial space to chord ratio must be set and the turning vane diagonal estimated. Barlow and Pope(1999) explain that the space to chord ratio should be one third or smaller in order to employ a reasonable lift coefficient.[3]

As for the number of vanes, this was determined through a relation of space to chord ratio and corner duct diagonal length(see Figure 3.5.

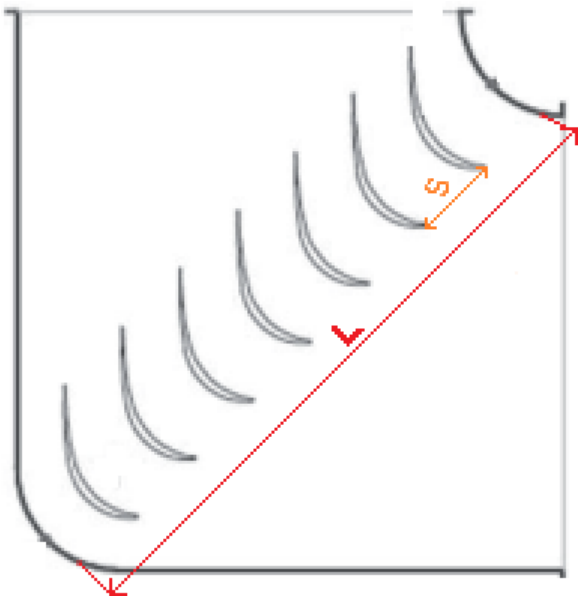

Figure 3.5: Schematics of vane numbering(adopted from[1]).

The equation 3.10 explains that the diagonal length equals to the space multiplied by the number of vanes less one with the difference of the first and last vane that correspond to the shape of the walls.

$$L = s \times (n - 1) - 2 \tag{3.10}$$

The Diagonal Length(L) is determined through the Pythagoras theorem con-

sidering the wide entrance and exit of the corner duct.(Please see in the Appendix complementing calculations). Therefore, the number of vanes (n) is:

$$n = \frac{L}{s} \_ 1 \tag{3.11}$$

3.5 Power Considerations

For a closed circuit of this size, a very efficient motor will have to be provided in order to enable the velocities required to this project. Pope(1999) elaborates that the most efficient fans provide a lift to drag ratio of about 50 . The place for the mounting of the fan is better suited for the fastest velocity of the wind section that runs through the tunnel. Data has been gathered regarding this section's nacelle drag as the velocity increases and it was concluded that the most efficient location to place the fan is downstream of the second corner duct in relation to the test section.

The area ratio between the fan and the test section is usually between 2 or 3 to 1. In case of the ratio being larger, there is a chance of a poor velocity profile before the engine section and an increase in cost due to the size. On the other hand, if area ratio is small, the incoming velocity will be higher and fan rpm will also be higher to maintain reasonable blade angles.

It is adequate to estimate the power in a flowing jet in order to obtain an idea of the forces and pressures involved. Equation 3.12 expresses this power, for example the flow in a wind tunnel test-section, it may be estimated through the density, test-section area as well the flow velocity.[3]

$$P = \frac{1}{2}\dot{m}V^2 = \frac{1}{2}\rho AV^3 \tag{3.12}$$

3.5.1 Nacelle Design

The nacelle should have a length to diameter ratio of about 3 with 30-40% of

its length of constant diameter. The equivalent closing cone angle should be 5° or less. [3]

3.5.2 Blade Design

The aerodynamic design of the two-stage blower (high powered fans are often called blowers) was carried out by Liming Peng, who was a Thermal Power MSc student at Cranfield Univeristy whose research project focused on the design of turbomachinery components for helium applications.

Depending on the type of cascade selected, the designer has various loosely established procedures for effecting his design. Table 3.1 summarizes the Mach number ranges in which the modern aerodynamic designer must work and the generally acceptable cascade types for each range.

Table 3.1: Mach number Range - Compressor blades section type correlation[27]

Category number	Design point inlet Mach number	Recommended section types
1	$M \leq 0.78$	NACA 65-series blades, circular or parabolic arc meanlines
2	$0.7 \leq M \leq 1.20$	Double circular arc sections
3	$1.10 \leq M \leq 1.50$	Arbitrary straight leading edge sections, specially design sections, multiple circular sections
4	$M > 1.50$	Special normal shock-free sections

3.6 The Contraction Cone

The effect of a contraction (CR) on unsteady velocity variations and turbulence is more complex as the reduction of axial component fluctuations is greater than that of transverse fluctuations. One of the Prandtl analysis predicts that the ratio of root mean square (rms) axial velocity fluctuation to mean velocity is reduced by a factor $1/CR^2$.

Equation 3.13 explains better the relation. For flow quality improvement, there is the contraction cone, also known as "Nozzle" through which the flow accelerates before entering the test section. For estimation and design purposes, the hydraulic diameter(HD) should be considered. In the contraction cone, the flow is accelerated rapidly. These results in a large streamwise strain, that reduces mean flow variations and higher the contraction ratio, means a greater strain and thus reduction.[3]

$$W_{Contraction} = HD_{TestSection} \times \sqrt{CR} \tag{3.13}$$

The contraction may be split into two sections. The first section has walls of concave shape and it is relevant to extend this part as much as possible to avoid wall boundary layer separation to occur here. There is risk for separation in the boundary layer due to the streamline curvature effects on the pressure gradient. The second part has walls of convex shape that tend to tangent continuity lines from the shape of the test section.

The design of a contraction centres on the creation of a uniform and steady stream. Two more advantageous criteria involve minimum exit boundary layer thickness and a minimum contraction length. An ideal design is when separation would be avoided while the exit non uniformity equals the maximum tolerable level. [3]

Following the Figure 3.6, the conditions required to define the polynomial starting at the wide inlet are: the coordinates (L,$\frac{W_{Entrance}-W_{Exit}}{2}$), the horizontal tangential condition in that point, the point where the contour line crosses the Match point, usually in the 50% of such line, and the tangency with the line coming from the narrow end. For the line starting at the narrow end the initial point is (L, $\frac{He}{2}$), with the same horizontal tangential condition in this point, and the connection to the wide end line.

Consequently, the polynomials are[1]:

$$y = a + bx + cx^2 + dx^3 \tag{3.14}$$

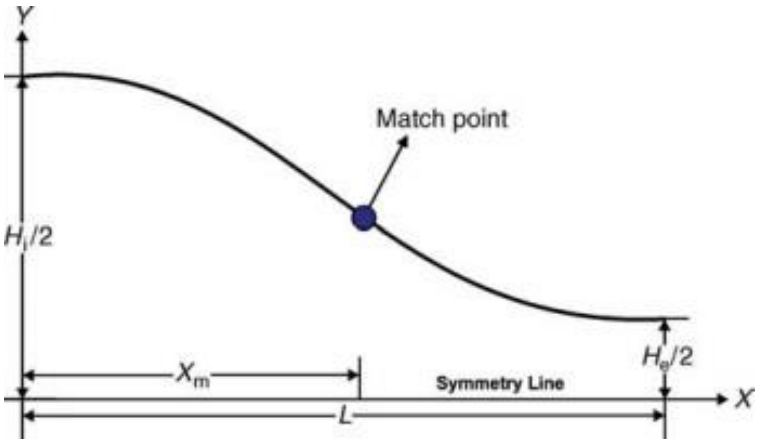

Figure 3.6: Schematics of the contraction shape[1].

$$z = a + bx + cx^2 + dx^3 \tag{3.15}$$

Considering the match point is in the middle of the contraction shape, the point coordinates should be:

$$(X_m, Y_m) = \left(\frac{L}{2}, \frac{W_{Entrance} - W_{Exit}}{2}\right) \tag{3.16}$$

Introducing the conditions in both polynomial equations, the two families of coefficients may be found.

3.7 Honeycomb and screens

The settling chamber mainly contains a honeycomb followed by screens. These are used to reduce the incoming airflow turbulence and increase the flow uniformity.

If severe swirl is expected in the flow from the wide-angle diffuser, it is reccomended to install at least one screen upstream of the honeycomb, so that the flow angles are reduced. The honeycomb should be installed some way downstream of the wide-angle diffuser exit, so that the flow static pressures and angles have had a chance to become more uniform.

Regarding the pressure loss estimations, once screens with small porosity, i.e,

$\beta < 0.57$, tend to generate instabilities, presumably in the form of longitudinal vortices, at least one screen with a larger β , β (> 0.57) should be used, at the most downstream position, if a truly two-dimensional boundary layer is required in the working section. A large β , $\beta > 0.8$, is also not suitable for good turbulence control. So the screens are chosen by respecting this β gap while looking for the lowest pressure loss. [15]

3.7.1 Spacing between screens

There are two fundamental properties to consider:

1. For the pressure drops inside the settling chamber through the screens to be completely independent, the spacing between them should be such that the static pressure has fully recovered from the perturbation before reaching the next screen (i.e. $\frac{dp}{dy} = 0$).[15]

2. It's recommended a screen spacing of 0.2 settling chamber hydraulic diameters and also this spacing between the last screen and the contraction entry. In case this distance is much shorter significant turbulence levels of the flow through the last screen may be expected. On the other hand, if the distance is too long, then unnecessary boundary layer growth occurs and consecutively the flow performance in this section decays .[3]

The Figure 3.7 presents a study of turbulence variations intensity for one and four screens. The result indicates that by the addition of three anti-turbulence screens placed in a suitable location in the settling chamber, the tunnel turbulence is decreased significantly for all operating speeds.

3.8 Cooling

All the energy supplied to the engine driving the wind tunnel finally emerges as an increase of heat energy in the flowstream. This means an increase of the global

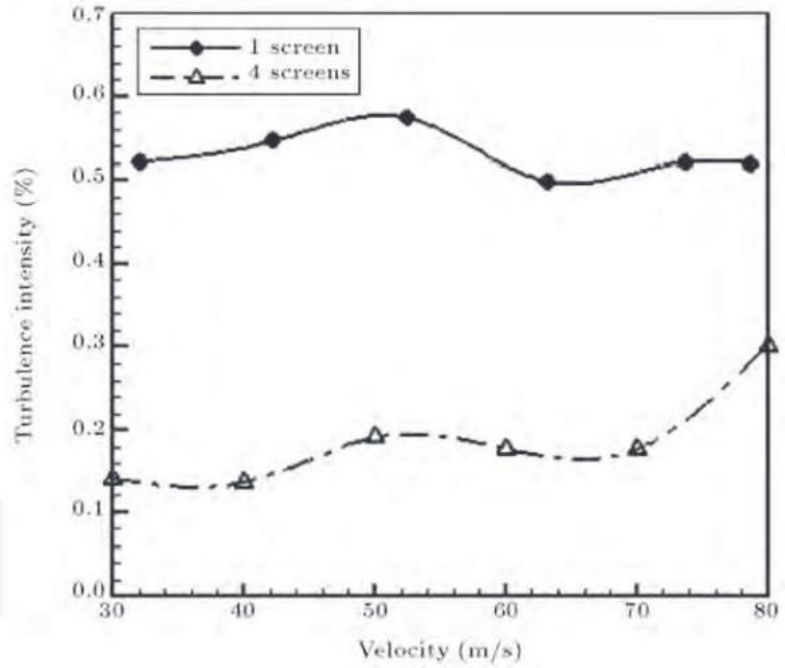

Figure 3.7: Variations of turbulence intensity Vs. velocity with one screen and four screens[23].

temperature of the tunnel flow until heat losses balance the input. For low-power tunnels, this balance is realized at reasonable temperatures, the heat transfer through the surface cooling and air exchange being sufficient. In the case of tunnels with high-power inputs or high jet velocities this low-temperature balance no longer occurs.[3]

In order to balance the flowstream heat energy of the wind tunnel by decreasing its heat energy, a cooling system is set. This system consists on applying a coolled heat of energy through a forced conduction to each set of corner vanes and then natural flow convection from the surface of the corner vanes to the flowstream. The equation 3.17 determines the required thermal energy(Q)[19].

$$\frac{dQ}{dt} = \dot{Q} = h \times A(T_{env} - T(t)) = -h \times A\Delta T(t) \tag{3.17}$$

where h $[W/(m^2K)]$ is thermal transfer coefficient, T_{env}[K] the environment temperature

and A[m^2] the Surface area to the place heat is being transferred.

$$T_m(x) = T_{m,i} + \frac{q_s'' P}{\dot{m} C_p} x \tag{3.18}$$

where q" represents the imposed heat flow, P the perimeter, $\dot{m}$ the flow rate, T_s[K] the Surface temperature and finally, $T_{m,i}$[K]the Convection temperature.

$$\frac{T_m(x) - T_s}{T_{m,i} - T_s} = e^{-\frac{Ph}{\dot{m} C_p} x} \tag{3.19}$$

In this subsection, it was also required for the turning vanes in the corners to provide 50% contingency temperature drop. In order to achieve this, the thermal energy should be lower and from Equation 3.17, the environment temperature is considered half in Celsius Degrees. This way, the thermal energy provided will be 50% of the energy if the temperature went down by its half.

Reversibly, if the temperature of the facility is below expected and the temperature of the main fluid also happens to be, instead of the system supplying cool heat of energy, it also may supply warm heat of energy.

Chapter 4

Results

4.1 General Description

The whole wind tunnel is about 9.522 meters long and 5.866 meters width. The fan diameter is 92 cm. The average velocity distribution in the wind tunnel is shown in Figure 4.1.

After the test section, the flow is expanding through a first diverging duct and reaches the first corner vanes. Then one diffuser with equivalent expanding angle of 3.5° expands the flow without separation before passing through the second corner vanes. The third diffuser ducts the second corner to the fan inlet. After the fan, the flow passes through a fourth diffuser and expands into a 134 cm side square section corner. A 178 cm long duct with expanding section follows before the flow goes to the fourth corner and before reaching the settling chamber. The settling chamber consists of one thick honeycomb to straighten the flow and 5 screens to reduce turbulence levels. Wood spacers may potentially be used to hold them in place inside the settling chamber box. The screen spacing depends on the mesh length of each upstream screen in order to optimize the turbulence reduction of the air flow (see section 3.7.1). Then, the well conditioned and uniformed flow enters the contraction cone and is accelerated to the test section inlet. The contraction cone consists of 2 matched cubic polynomial curves to guide the flow from a

157.5 cm square duct to a 97 cm x 36 cm rectangle duct, equivalent to a contraction ratio of 7.5.

The wind tunnel has a mass flow rate of 5.78 kg/s at design conditions and takes about 6.65 kg of helium to perform optimally. It is included to this quantity, a 20% plus of the total helium required to fulfill the whole closed tunnel.

The figures provided in this chapter are designed by the author. Figure 4.1 shows the average velocity distribution of the wind tunnel.

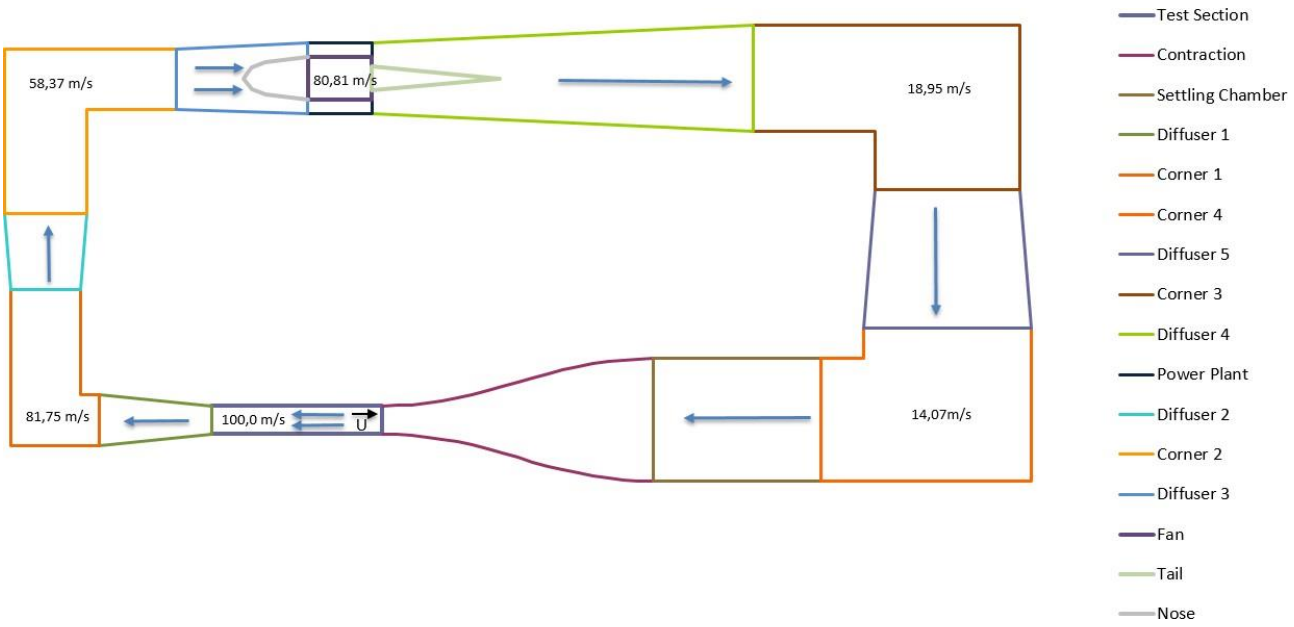

Figure 4.1: Schematics of the wind tunnel with average velocity distribution

4.2 Test Section

The first step in the design of a wind tunnel is to determine the size and shape of the test section. This choice depends on the intended uses of the facility and, as will be discussed, is intrinsically linked to financial resources available to build the equipment and also the cascade dimensioning.

Three quarters of scale factor(in relation to GTHTR300) were considered at the initial design stage, considering the cascade blades cruising to a Mach number of 0.0979 and with span close to 36 cm and a length of 1.60 m. An approximation to

the available Reynolds number in atmospheric conditions is 100.000, not similar to the GTHTR300 but at representative flow conditions, providing satisfactory speed limits for the models that could be accommodated inside the closed-test section. The sidewalls may be made of plexiglass which enables optical access to the cascade.

4.2.1 Cascade

The cascade is set on a turntable disk. The blades are initially set to an angle of 5° and as the spacing and incidence angle may change, the space to chord ratio also may. The blade chord is 12.0 cm, the span length is 36 cm, its airfoil is NACA 65(12)-10 and has a stagger angle of 6,5°. Considering the size of the blade and a flow velocity of 100 m/s, the Reynolds number produced is about 105.200 . The cascade is dimensioned to assemble a maximum of 7 compressor blades and set to vary a space to chord ratio from 0.7 to 1.2. Figure 4.2 shows the cascade assembly with a space to chord ratio of 1.2.

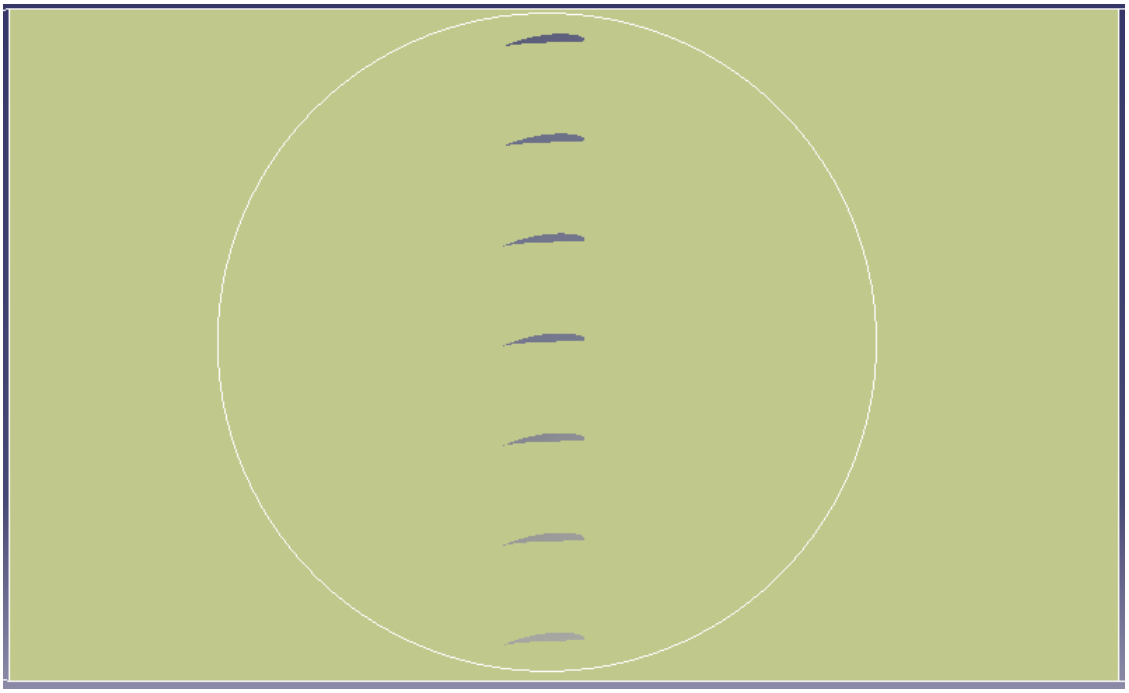

Figure 4.2: Front view of the compressor cascade

4.3 The Diffuser

The inlet cross-section area and shape of the first diffuser are known because they equal the cross section area and shape of the test chamber(see Figure 4.3 while respecting the expansion angle. Side views are presented in the Appendix A.1,A.2).

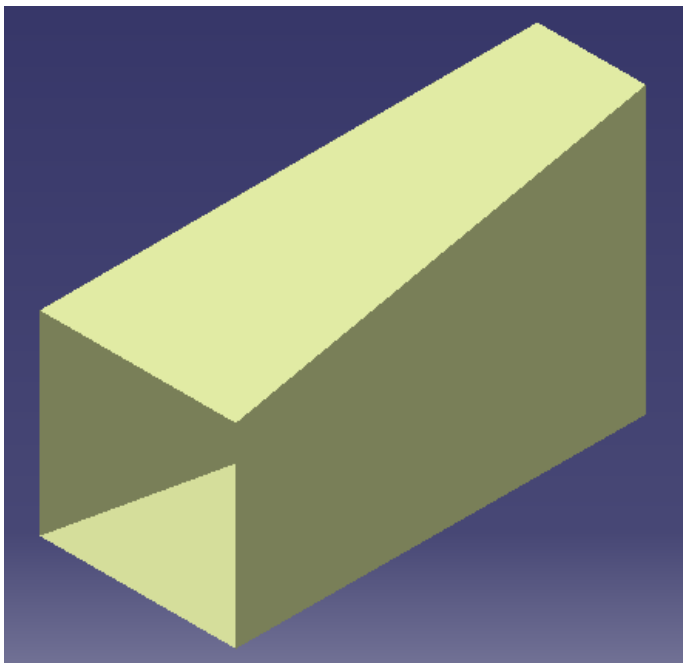

Figure 4.3: First diffuser design

The second diffuser, connecting the first corner duct to the second corner duct is presented in Figure 4.4 The outlet cross-section area of the third diffuser is also known because it equals the inlet fan cross-section area. Since the fan inlet cross-section is round and most diffusers are square, the third and fourth diffuser take the form of a Multi-Section's surface modelling result as presented on Figure4.5 applied from CATIA software.

Finally, the last diffuser takes the maximum width and height of the contraction cone.(see Figure 4.6

Considering a diffuser semi-angle of 3.5°, the dimmensions of every diffuser are presented on the next Table 4.1

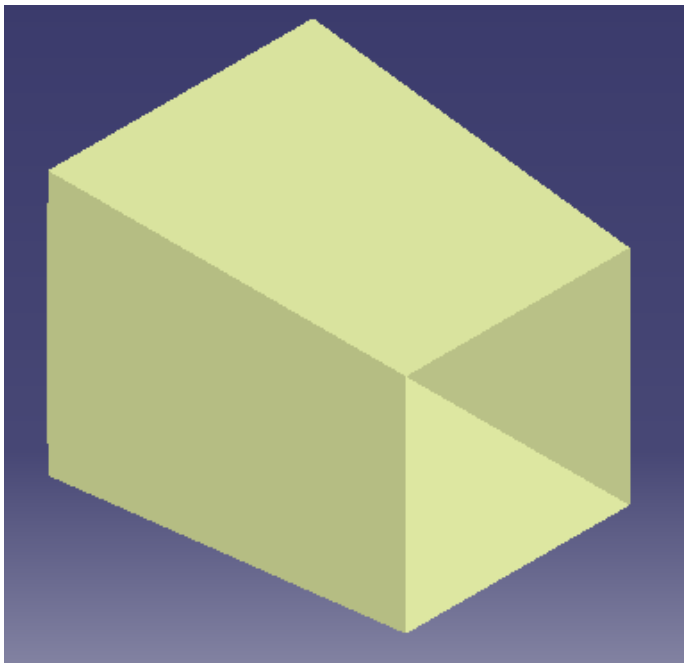

Figure 4.4: Second diffuser design

Table 4.1: Diffuser dimensions

Diffuser	Entrance Width[m]	Entrance Height[m]	Exit Width[m]	Exit Height[m]	Length[m]
1	0.360	0.970	0.654	0.654	1.005
2	0.654	0.654	0.773	0.773	0.980
3	0.773	0.773	0.920	0.920	1.230
4	0.920	0.920	1.358	1.358	3.577
5	1.358	1.358	1.575	1.575	1.780

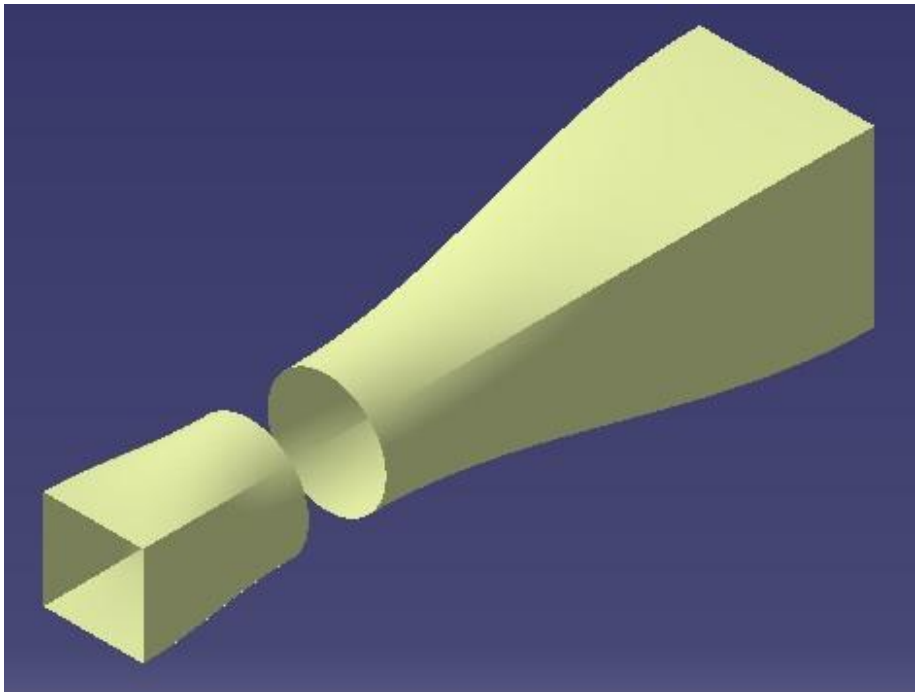

Figure 4.5: Third and fourth diffuser design

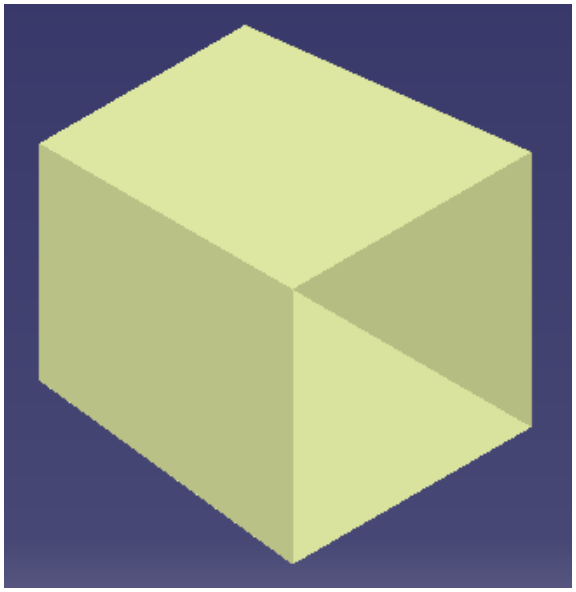

Figure 4.6: Fifth diffuser

4.4 Corner Ducts

In order for the flow to be turned 90°, 4 sets of corner ducts have been designed.

Following Figure 4.8, every corner was integrated with similar turning vanes specially designed to turn the flow by 86º at the bend. Also, these turning vanes are quite important to avoid large losses and to maintain relatively straight flow inside the channel.

For the turning vanes, thin plates were considered as they produce a considerable less pressure loss in relation to blade vanes. These thin plates have chord of 25.4 cm, a thickness of 16.3 mm and a space to chord ratio of less than 1/3.

Table 4.2: Corner dimensions

Corner Width	Entrance [m]	Exit[m]	Number of vanes
1	0.654	0.654	12
2	0.773	0.773	13
3	1.358	1.358	18
4	1.575	1.575	21

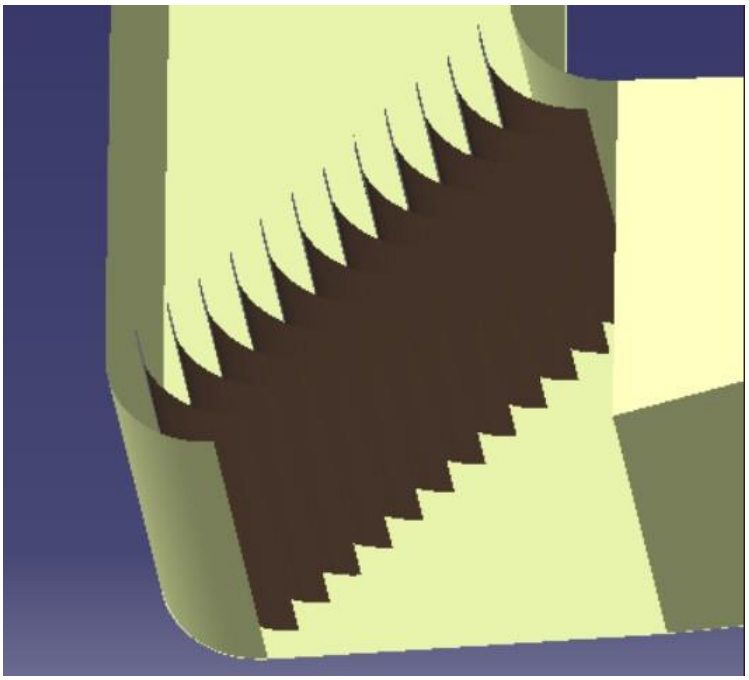

Figure 4.7: First corner vanes

The table 4.2 details the dimensions of the corners.

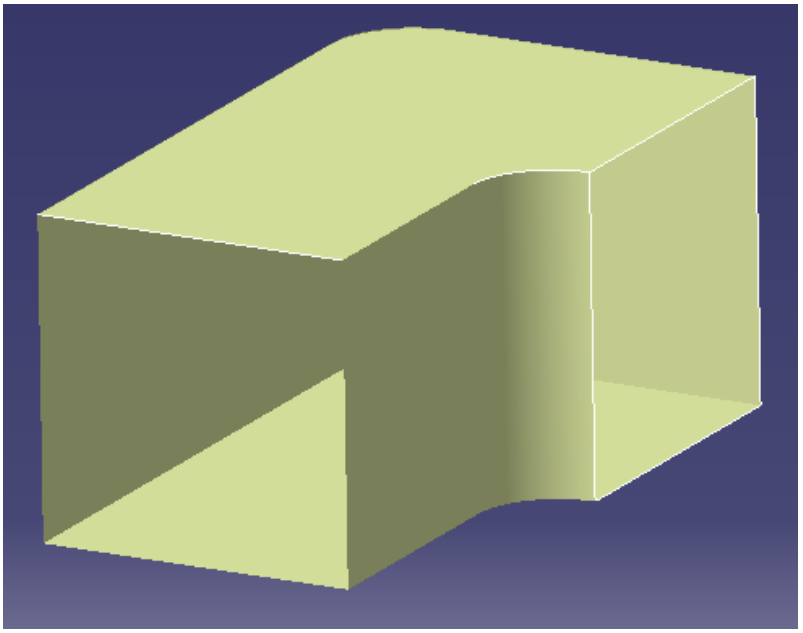

Figure 4.8: Second corner design

4.5 The Fan Section

The facility is powered by a 118.7 kW two stage axial blower with an output capacity of 5.78 kg/s at design conditions. This bespoke fan has a design rotational speed of 4620 rpm. This section was designed so that an axial velocity of 80 m/s is achieved. The wind tunnel has been dimensioned to be able to run experiments at a Reynolds number of 100,000, based on the axial chord, similar to engine conditions. The engine will be assembled in a “puller” configuration as a design choice. With this engine configuration, there is a better aerodynamic performance in comparison to a "pusher" configuration and is expected less flow turbulence. The area ratio between the fan and the test section is 1.94, aproximately 2. The fan dimensions from Liming Peng’s study is presented in Table 4.3

Design Table 4.3 presents the inner and outer radius of the fan, giving the dimensions for the blades span and structure sizing of this section.

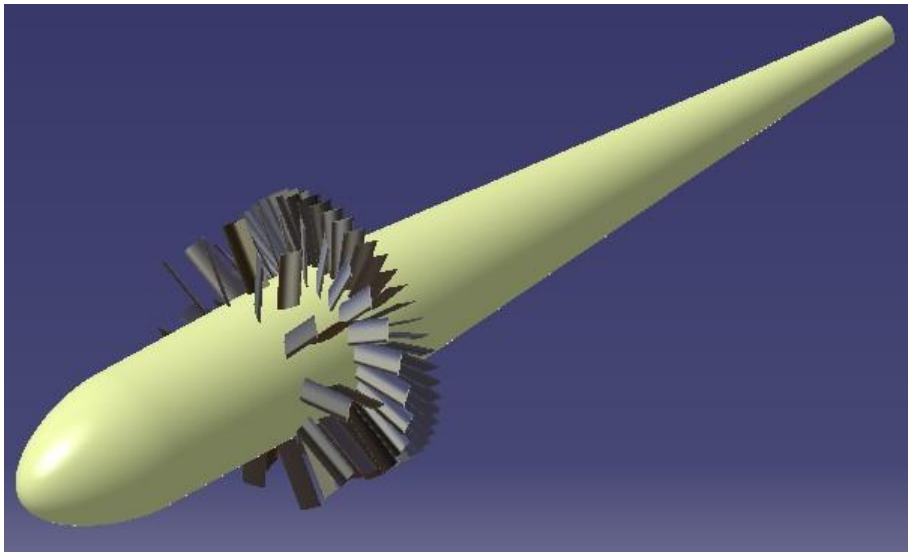

Figure 4.9: Nose, fan and tail design

Table 4.3: Fan dimensions in meters

Fan Radius	Inlet [m]	Exit[m]
Inner	0.279	0.281
Outer	0.465	0.464

4.5.1 Blade Design

Once the Mach number at the Fan section is about 0.23, the recommended airfoils are the NACA 65 series. The chosen airfoil blades are NACA 65-(12)10 and should be built in aluminium or steel.

Table 4.4 describes the design of the two-stage blower in terms of number of stages, the angles β and α of blades. Estimations made by the former student Liming Peng predict an 4620 rpm's, a mean blade speen of 180.09 m/s and a fan radius of 0.37 m.

where α and β correspond to the blade angle a fluid flow entrance angle, respectively.

Table 4.4: Blade design parameters

Stage Number	$\alpha 1$ [°]	$\alpha 2$ [°]	$\alpha 3$ [°]	$\beta 1$ [°]	$\beta 2$ [°]
1	0.0	35.6	28.7	66.1	56.9
2	28.7	51.4	20.0	59.6	44.9

Table 4.5 details the design of the high powered fan in terms of the space to chord ratio(s/c) of the blades and its number:

Table 4.5: Blade design parameters

Annular Blades	1	2	3	4
s/c	0.0	35.6	28.7	66.1
Number	19	10	25	51

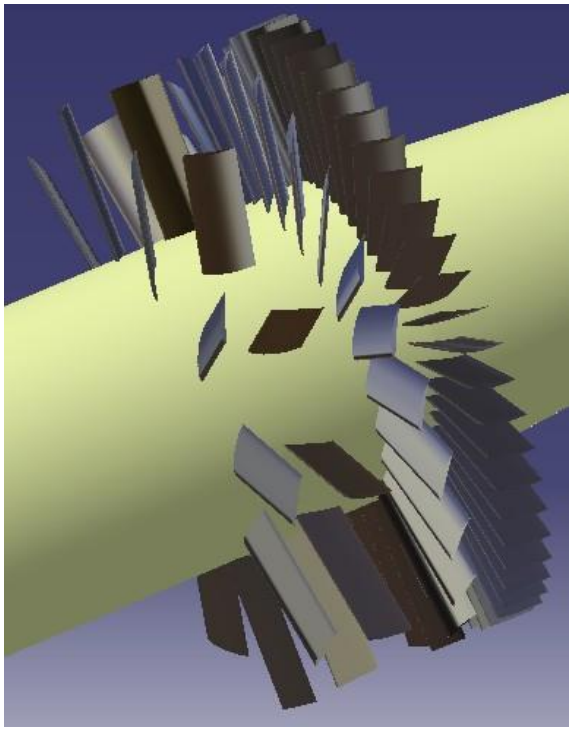

Figure 4.10: Fan blades.

4.6 Honeycomb and screens

The settling chamber is 1575 mm long. There are 5 screens at the settling chamber and one honeycomb. The honeycomb used here is 75 mm long and the hexagonally shaped cells have a diameter of a quarter of an inch or 6.4 mm. The honeycomb applies a pressure loss coefficient of $K_{honeycomb} = 0.2$.

The primary reason to use a honeycomb is that, with a sufficient length of about 14 mm cell diameters, it is a very effective flow straightening device, the most

optimal size. It allows to maintain compressive strength while reducing weight.The dimensions of the screens are presented on the following table:

Table 4.6: Screens dimensioning[14]

Screen	Mesh width [mm]	Wire diameter[mm]	β	Re_{wd}	K_0
1	3.2	0.71	0.61	$8.76x10^4$	0.55
2	2.4	0.56	0.59	$6.91x10^4$	0.63
3	2.4	0.56	0.59	$6.91x10^4$	0.63
4	0.7	0.16	0.60	$1.97x10^4$	0.59
5	0.7	0.16	0.60	$1.97x10^4$	0.59

Figure 4.11 presents a more detailed and closer look to the designed settling chamber:

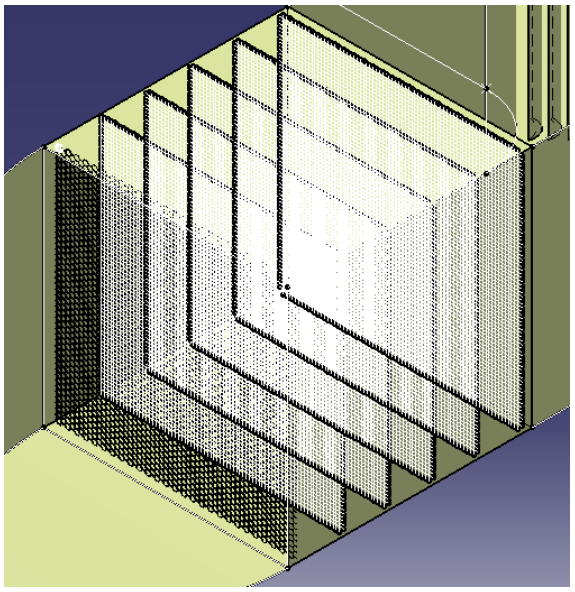

Figure 4.11: Tri-dimensional of honeycomb and screens.

4.7 The Contraction Cone

The contraction ratio also sets the height and width of the fourth corner. As mentioned previously,the fan was already selected and the dimension of it as well.

In order for the flow to be gradually increased until the fourth corner, the contraction ratio had to be at least 7.2. This way, when the flow reaches the fan, the diffusers may still expand and not contract. And since flow speed at the test section is

relatively high, it demands a high flow quality that a contraction ratio of 7.5 provides. The contraction ratio is 7.5 as the Figure 4.12 presents and the equations below estimate;

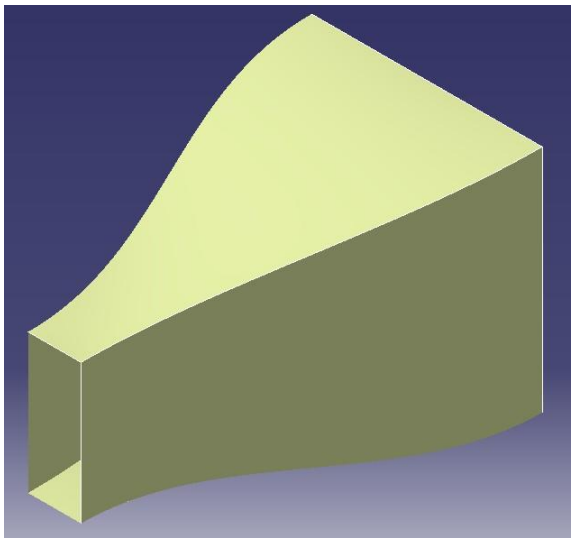

Figure 4.12: Contraction Design.

Equations 4.1 and 4.3 give the polynomial spline from the entrance until medium points of the shape to their respective y and z component, while Equations 4.2 and 4.4 present the polynomial spline from the medium to exit point of the contraction cone. Through these equations, the total contraction shape may be designed.

$$y = 0.22544x^2 - 0.2954x^3 \tag{4.1}$$

$$y = -0.3646 + 0.57339x - 0.02954x^3 \tag{4.2}$$

$$z = 0.11229x^2 - 0.01472x^3 \tag{4.3}$$

$$z = -0.1816 + 0.2856x - 0.01472x^3 \tag{4.4}$$

Table 4.7 presents the contraction entrance and exit dimensions.

Throughout this section's and wind tunnel design, the area ratio of the nozzle

Table 4.7: Contraction dimensions

Contraction	Entrance [m]	Exit[m]
Width	1.575	0.360
Height	1.575	0.970

was in consideration. It is optimal to maximize the area ratio because it will cause the fluid in the rest of the tunnel to move in slower motion relatively to the fluid in the test section. Once pressure losses of each component change with the local helium speed squared, by maximizing this area ratio will result in a higher efficiency of the tunnel.

4.8 Cooling

Estimations were made considering that the fan increases the temperature of working fluid by $4°C/s$ and that the initial temperature of the fluid is $25°C$ and the imposing heat temperature to be of $20°C$. By applying heat transfer through the 4 sets of corner vanes, the new temperature of fluid is presented on Table 4.8.

Table 4.8: Flow cooling temperature estimation

Corner	T_{flow} [°C]	T_{flow} ° C 50%
1	20.21	10.63
2	20.61	11.20
3	20.67	12.29
4	20.69	12.66
Total average	20.61	11.20

4.9 Total Pressure Loss

Following the applications of the pressure loss equations presented in the State of the Art chapter including other computational calculations, the summary of the dynamic pressures losses are determined considering two space to chord ratios of the turntable cascade blades with flow travelling by 100 m/s at the test section.

The Table 4.9 summarizes the total pressure loss estimation for the initial cascade design set, a blade's space to chord ratio of 1.2:

Table 4.9: Total dynamic pressure loss estimations for the compressor cascade with s/c equal to 1.2

Component	K_0	Total Losses(%)	ΔP (Pa)
Test Section	0.178	13.7	63.22
Diffuser 1	0.075	9.4	43.10
Diffuser 2	0.028	5.1	23.27
Diffuser 3	0.003	0.6	2.57
Diffuser 4	0.042	7.7	35.55
Diffuser 5	0.001	0.2	1.09
Settling Chamber	0.063	11.6	53.58
Power plant	0.111	20.3	93.55
Corner 1	0.118	21.6	99.48
Corner 2	0.033	6.1	27.98
Corner 3	0.001	0.1	0.67
Corner 4	0.001	0.1	0.23
Contraction	0.019	3.6	16.37
TOTAL	0.545	100	460.64

As expected from a typical closed wind tunnel, reading Table 4.9, from the five diffusers, the first expanding component after the test section loses the biggest amount of pressure. Afterwards, when flow reaches the first corner, from all sets of corners, this is the one where pressure takes a significant hit of loss.

Figure 4.13 shows the flow field around an individual cascade blade. The plot depicts the velocity distribution in a periodic passage of the cascade. The simulation employed 2D compressible model, k-epsilon turbulence model and inlet velocity and outlet pressure boundary conditions. A hexahedral mesh was employed.

The space to chord ratio is 0.7, corresponding to the most severe spacing that the project envisages testing. For the low angles examined, the pressure drop does not vary greatly with the angle of attack, somewhat surprisingly. Within that range the static pressure loss for the seven blades is of the order of 620 Pa, which is very high and definitely unbalances the pressure loss distribution. Taking this into account, Table 4.10 represents the estimated pressure losses for the cascade blades with a space to chord ratio

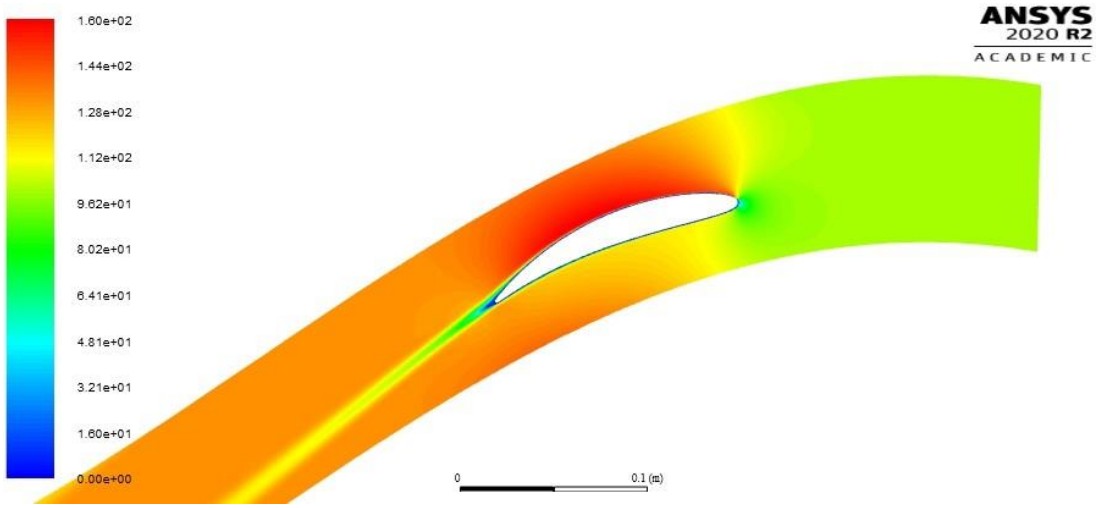

Figure 4.13: Simulation of cascade blade s/c=0.7 .

of 0.7:

Table 4.10: Total dynamic pressure loss estimations for the compressor cascade with s/c equal to 0.7

Component	K_0	Total Losses(%)	ΔP(Pa)
Test Section	0.789	62.7	667.02
Diffuser 1	0.051	4.0	43.10
Diffuser 2	0.028	2.2	23.27
Diffuser 3	0.003	0.2	2.57
Diffuser 4	0.042	3.3	35.55
Diffuser 5	0.001	0.1	1.09
Settling Chamber	0.063	5.0	53.58
Power plant	0.111	8.8	93.53
Corner 1	0.118	9.3	99.48
Corner 2	0.033	2.6	27.98
Corner 3	0.001	0.1	0.67
Corner 4	0.001	0.0	0.23
Contraction	0.019	1.5	16.37
TOTAL	1.260	100	1064.44

Comparing the two tables above, there is a significant difference on the total static pressure loss coefficients and its distribution. If the cascade space to chord ratio is 0.7

For frictional losses estimations, steel was the material considered.

At the settling chamber, finding proper screens was a challenge. Estimations

across several types of screens performed on past experiments were analysed until the most suitable screens were found.

In the corner duct, the losses due to the vanes can be made small by selecting an efficient cross sectional shape and by using an appropriate space to chord ratio. In the beginning of the project, different equations and options were explored. Hollow cambered airfoils were considered but, as a result of high pressure loss were then changed to curved plate vanes. Estimations were updated and produced a lower pressure loss. A comparison was made on the current curved plates to the initial considered airfoil cambered blades design. The comparison reveal a decrease in pressure of about 30% in the first corner duct and about 53% of the total pressure loss.

In Winter (1952)[26] experimental data on corner vanes cascades can be found, similar to the Reynolds number and pressure and vane profiles we are studying at this section. Winter reported a pressure loss coefficient K of 0.033 at a Reynolds number of 1.9 x 10^6. This loss only considers the integrated pressure profile at mid-span of the 2D profile. It does not take fully into consideration all the secondary losses such as endwall effects. Though, the operating Reynolds number is about 500,000, similar to engine conditions and also closer to the optimal operating condition of this vane profile. Therefore, it may be presumed a vane pressure loss coefficient of the cascade $K = 0.3$.

.

The pressure loss in the diffusers was evaluated through frictional and expanding losses.

These estimations were consistently iterative as they were aimed to achieve a energy ratio closer to 3.

It was also made an estimation of the dynamic pressure loss considering air as the working fluid of the closed circuit. Table 4.11 reveals the results of the total pressure loss for the wind tunnel with air and helium as the main fluid and the compressor cascade design with s/c of 1.2 .

Table 4.11: Total dynamic pressure loss estimation comparison between air and helium for the compressor cascade with s/c equal to 1.2

Component	Air ΔP (Pa)	Helium ΔP (Pa)
Test Section	458.23	63.22
Diffuser 1	312.39	43.10
Diffuser 2	168.69	23.27
Diffuser 3	18.61	2.57
Diffuser 4	257.66	35.55
Diffuser 5	7.91	1.09
Settling Chamber	388.37	53.58
Power plant	677.98	93.55
Corner 1	721.06	99.48
Corner 2	202.84	27.98
Corner 3	4.83	0.67
Corner 4	1.70	0.23
Contraction	118.67	16.37
TOTAL	3338.95	460.64

As expected, if air flows through the wind tunnel, the dynamic pressure loss will increase. Estimations reveal it is 7.25 times higher in relation to helium.

Figure 4.14 presents a graphic plot that shows the pressure loss is proportional to the velocity. It also shows the total estimated pressure loss for the respective speed. Red dot highlighted corresponds to the speed of 100 m/s studied. Inherent to the project, it is the pressure loss associated to the testing velocity and it has to be chosen in a reasonable

but feasible way.

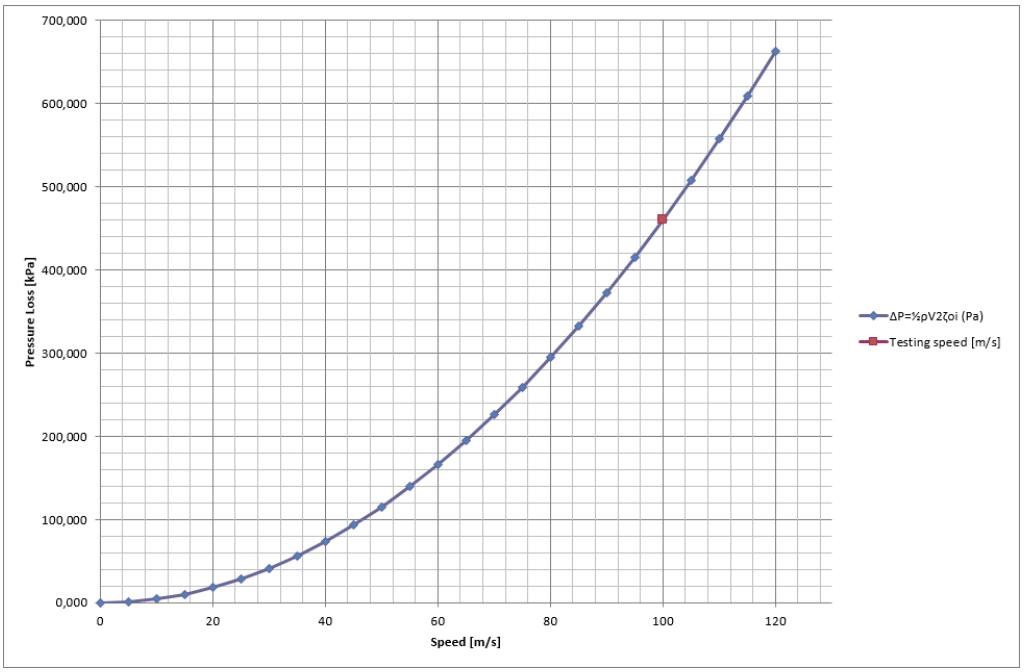

Figure 4.14: Variation of pressure with velocity

4.10 Wind Tunnel Views

Finally, in order to conclude this chapter, the Figures below present the sum of each designed component into a final global configuration of the wind tunnel. The Figures 4.15,4.16 and 4.17 picture the sides of the wind tunnel final design.

The figure 4.20 represents a tri-dimensional view, whereas the corner vanes, the cascade of the test section,the fan and honeycomb are included in detail.

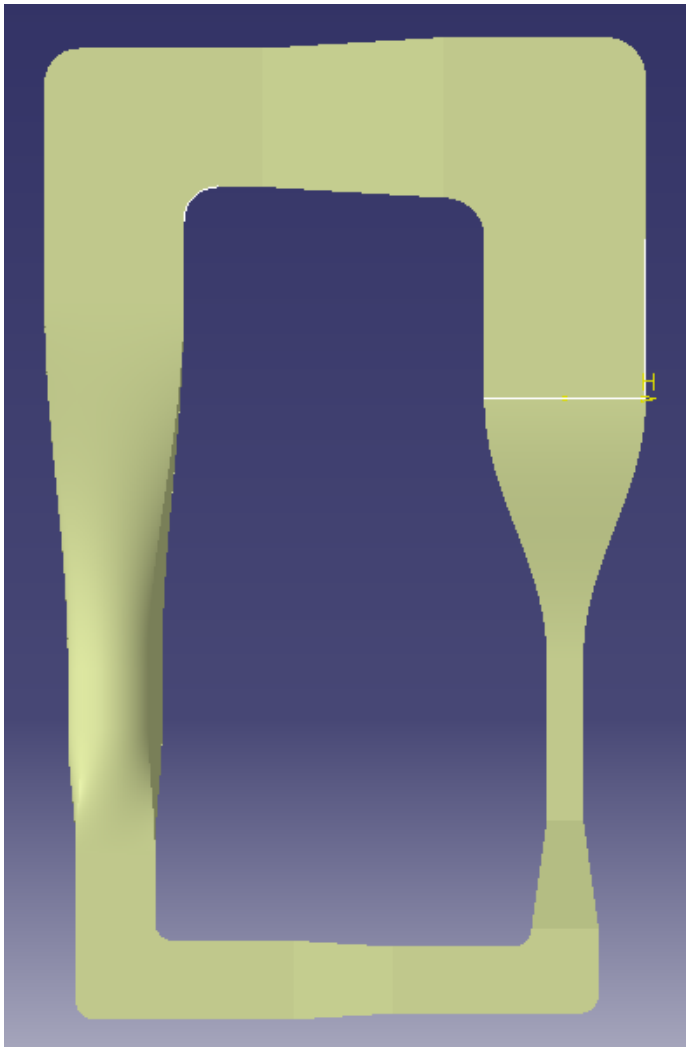

Figure 4.15: Bi-dimensional top view of the wind tunnel.

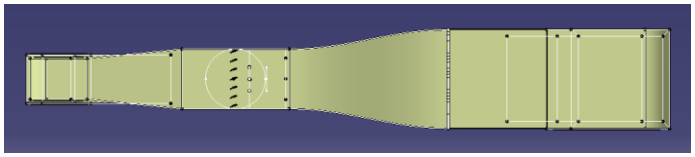

Figure 4.16: Bi-dimensional front view of the wind tunnel.

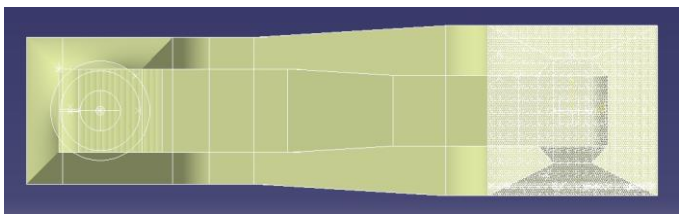

Figure 4.17: Bi-dimensional left view of the wind tunnel.

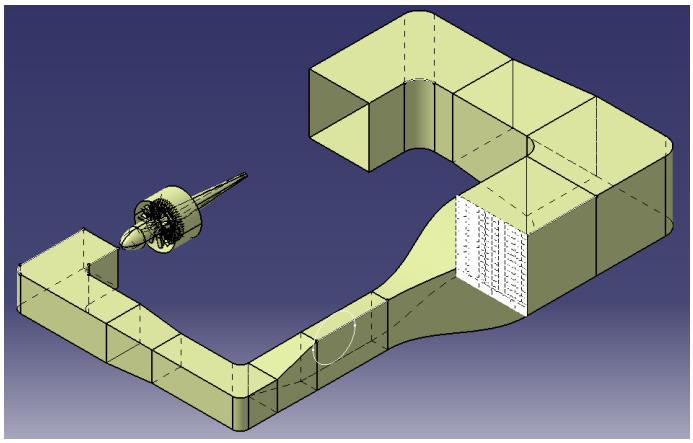

Figure 4.18: Engine in the tri-dimensional view of the wind tunnel.

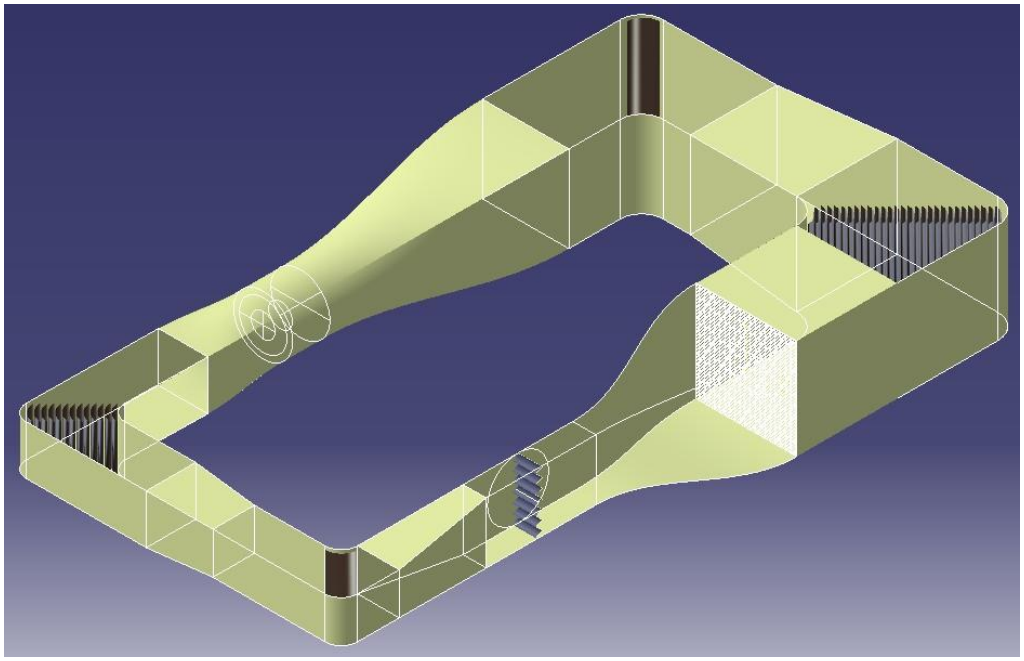

Figure 4.19: Tri-dimensional open view of an open Wind tunnel.

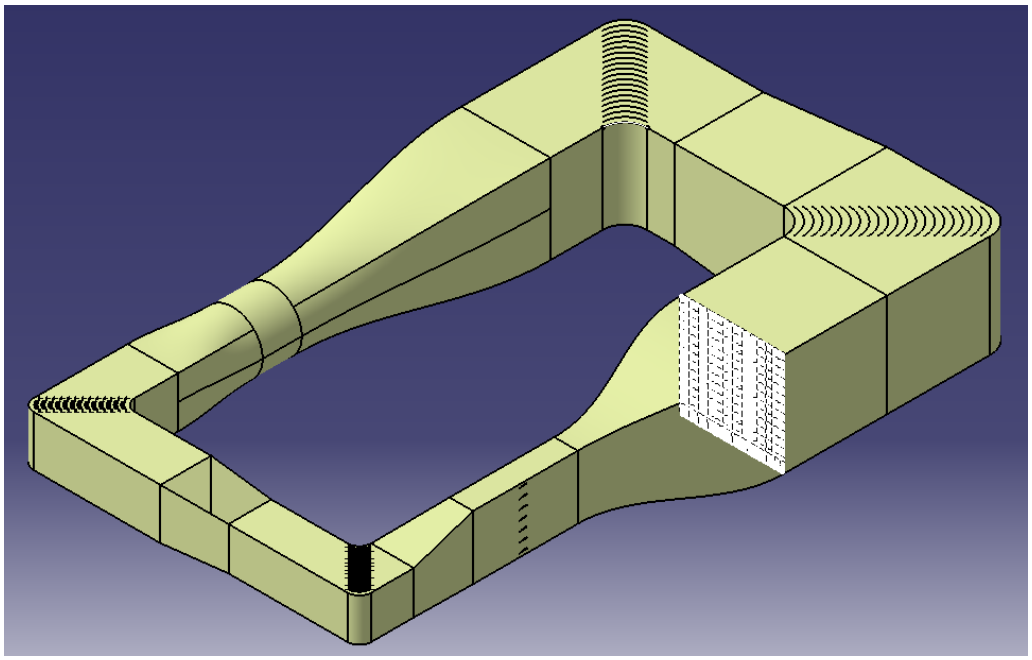

Figure 4.20: Tri-dimensional closed view of Wind tunnel.

Chapter 5

Discussion

During the development of the previous chapter, a particular analysis was made to each section and what is expected from each components design. This chapter gives mainly a global analysis of the project.

The design of an experimental rig such as a wind tunnel is an iterative process and multidisciplinary, where it is not possible to make changes to one area without influencing the others. It is a hardworking task with many research articles across several contents such as fundamentals of aerodynamics, CFD, history of wind tunnels, fluid properties and estimations.

Pressure loss The search of means on how to reduce the pressure loss was also extensive. Finding equations and looking for the most adequate but also reliable was one of the hardest tasks. Still, there are unknowns associated to the pressure loss that not even the most advanced CFD can determine the exact loss.

The major restrictions on the feasibility of the work, regarding the pressure losses, are that CFD was not applied to the whole wind tunnel but a compressor blade. Therefore, the analytical estimations are not enough to exactly confirm.

Design Throughout the research and development of the estimations, several wind tunnel designs were made and taken to the Advisors and Engineer Arnold G. Briggs. After

their consultation on the design and also methodology estimations, the respective modifications and new research were applied, estimations changed and a new design was born. CATIA was the main design tool for the dimensioning of each component. Efforts and time were applied in simulating a compressor blade through CFD, ANSYS Fluent. Further time would be needed to fully simulate tridimensionally the wind tunnel.

Methodology In the beginning, an excel spreadsheet [9] made by students from Polytechnic University of Madrid and Beijing Institute of Technology was used and taken into consideration. As it sets the basic but detailed algorithms and estimations to the design of a quick and low cost wind tunnel. Then, new and further work was made. A more detailed and developed excel spreadsheet was achieved and iterated (see Figures in Appendix). Redefining design equations and algorithms adequate to the project, considering the instrumentation and its effects once applied, refining the accuracy of the pressure losses of each component and rewriting equations for bidimensional top pre-view of the tunnel. Applying a constant expansion angle, adding similarity parameters at the test section, adding cooling estimations and also associating Liming Peng's power estimations were also fundamental to the main spreadsheet.

Test Section The installation of a plexiglass sidewall at the test section should enable a visualization of the flow moving through the helium compressor cascade. This way, it will be possible to study a number of parameters and arrangements relevant to helium cascades, namely space to chord ratio, camber and flow separation, airfoil type and also off-design conditions including dependency on surface roughness and Reynolds number.

The aerodynamic performance data such as efficiency and the parameters mentioned above will be obtained through the tests to verify the design and evaluation methods of the helium gas compressors blading. The test results shall serve to further improve the aerodynamic design of the helium gas compressor blading.

Cost As one of the most important design requirements, the cost of the materials and components play the one of largest roles in this project. It is essential to have a balance between the cost of the materials and the overall optimum performance. As mentioned previously, bigger the size of the materials, higher will be its cost. So, during the design development, certain limitations were set, such as the sizing and lengths. Looking at the design requirements for this tunnel, the most costly of items would most likely fall under the corner ducts and fan motor.

Chapter 6

Conclusions

The design and detailed construction of a closed loop circuit, low subsonic wind tunnel was presented. Analytical models were considered to estimate the pressure losses and CFD was also applied on one compressor blade of the test section. The main conclusions are summarized and described, shedding light to the most fundamental design parameters and observations gathered during this project:

- The data regarding the existence of helium compressor cascades is scarce and not easy to find. As through the development of the literature review, this data was found indirectly in big projects such as the GTHTR300 project. Although this project doesn't envisage the construction of a wind tunnel or testing of an object, the gas turbine of this power plant and in particular, its compressor, it is runned by helium. So the need to improve further this data, attracted the concept of using wind tunnels to analyse the aerodynamic performance of helium gas compressors blading.

- At the test section, while designing the cascade configuration, the project was aiming for a Reynolds number of 100.000. Initially basing the chord on the GTHTR300 compressor blade, the flow stream velocity at the test section was estimated at 100 m/s.

- The size of the chord (12 cm) from the testing cascade was first based on the helium

compressor from GTHTR300 and then obtained in regards to the most optimal result of the estimations for the sizing of the cascade. In order to test the cascade, the Reynolds number couldn't be lower than 100.000 while testing at a speed of 100 m/s.

- The wind tunnel design is not standard procedure and depends extensively on variables such as facility space dimensions, flow speed requirements, goals of the project and cost for fabrication. The first 2 variables are quite sensitive to the need of educational and research purposes and can be copped through the stages of design. The cost variable imposes hard limitations to the design.

- The selection of turning vanes is fundamental to improve the flow quality in the test section and exigent as it requires optimal vanes to reduce pressure losses to a minimal point. A comparison was made on the current curved plates to the initial airfoil cambered blades design. The comparison reveal a decrease in pressure of about 30% in the first corner duct and about 53% of the total pressure loss.

- The fan blade is also fundamental to the wind tunnel performance. The design of optimal airfoils and propelling blades has been studied in great detail in the last decades and is given now to the designer some satisfactory data for designing such devices. This section was overseen by another student, Liming Peng, in which he made estimations to the dimensions of the power fan and also the wind tunnel power requirements.

- Nowadays, the design of the contraction is well defined and the amount of current information can lead to a feasible and effective shape. Additional tools, for example CFD simulations, are recommended to help improving the final design and identify some problems related to the flow uniformity.

- Although the cost related to aluminum or steel honeycombs and screens is very high and requires special attention for providing a solution, the choice of including at a

settling chamber is vital.

- Regarding the flow analysis, a CFD approach is quite indicated for this kind of design. The simulations may provide a good insight into how the flow runs inside the circuit, leading to additional ideas to improve the geometric shape. When possible, it is highly advantageous to proceed with such simulations as soon as the first design is achieved.

- There can be more work done on CFD simulations in order to determine the optimal spacing of the turning vanes to reduce losses and maximize flow uniformity in the corners. After the simulations on the corners and nozzle have yielded optimal designs, they can be built.

- The design of the corner ducts and vanes aim to reduce the pressure loss while redirecting the flow.

- The pressure losses in the diffusers should account the losses due to friction and expansion.

- The test section has pressure losses due to friction and the drag produced by the testing objects.

- The settling chamber stabilizes the flow to uniformity when it passes through the screens and honeycomb right before entering the contraction. This section generates a significant increase in pressure loss.

- The contraction accelerates the fluid to the maximum right before entering the test section. This section does not increase the pressure drop remarkably.

- The use of helium on estimations indicate significantly lower pressure losses and therefore a higher energy ratio. As the properties of helium-air comparisons state and results of this project through helium as the working fluid show, helium is

a fascinating fluid to run thermodynamic and energy experiments. It has a big potential to future and some of the current nuclear power plants.

- The estimations comparison made regarding air and helium for the designed wind tunnel indicate that air generates about 7.25 times the dynamic pressure loss that helium produces.

- On the other hand, one must magnify that the wind tunnel design and especially construction is without a doubt a very hardworking process which passes through from extensive and intensive research to meet the design criteria. There are many aspects that impose limitations and risks for the its design and construction phase, which must be properly addressed by the wind tunnel designers. Preliminary tests should indicate that the requirements of speed and flow quality have been met with success.

- The cost of the whole equipment and specific parts such as power system can really put pressure on the design for simpler configurations. Also, one of the most important phases of the design is not technical but economical.

- The next step to this project is to obtain funds to complete this tunnel.

- Once the construction of the wind tunnel is complete, instrumentation will need to be installed. This includes drilling holes to insert pitot static tubes in the settling chamber and test section. After the instruments have been installed and calibrated, the tunnel can be used for experiments.

- Finally, although this project envisages the testing of helium compressor cascades through detailed wind tunnel design, there is much more data to be added and explored to the future of Generation IV nuclear power plants.

References

[1] Odenir De Almeida et al. “Low Subsonic Wind Tunnel – Design and Construction”. In: *Journal of Aerospace Technology and Management* 10 (Feb. 26, 2018).

[2] Donald D. Baals and William R. Corliss. *Wind Tunnels of Nasa,Vol. 440*. Harvard: Scientific, Technical Information Branch, National Aeronautics, and Space Administration, 1981.

[3] Jewel B. Barlow et al. *Low-speed wind tunnel testing*. 3rd ed. New York: Wiley, 1999. 713 pp.

[4] D. S.Vijaya Bhaskar, ed. *Electrical Integrators Americas*. (accessed: 01.09.2021).

[5] *Boundary LayerNASA*. https://www.grc.nasa.gov/WWW/k-12/airplane/boundlay.html. Accessed: 2010-09-30.

[6] *Closed Return Wind TunnelNASA, NASA*. www.grc.nasa.gov/WWW/K-12/airplane/tuncret.html. Accessed: 2010-09-30.

[7] *Draf Coefficent value for different shapes of bodies*. http://www.aquaphoenix.com/lecture/matlab5/page2.html.. Accessed: 2010-09-30.

[8] Miguel A. Gonzalez Hernandez et al. “Design Methodology for a Quick and Low-Cost Wind Tunnel”. In: *Wind Tunnel Designs and Their Diverse Engineering Applications*. Ed. by Noor Ahmed. InTech, Mar. 6, 2013.

[9] Miguel A. Gonzalez Hernandez et al. “Design Methodology for a Quick and Low-Cost Wind Tunnel”. In: *Wind Tunnel Designs and Their Diverse Engineering Applications*. Ed. by Noor Ahmed. InTech, Mar. 6, 2013.

[10] Filip Grochowina. “PERFORMANCE EVALUATION OF GAS TURBINES FOR NUCLEAR POWER PLANTS”. In: (), p. 123.

[11] Jonathan Jaramillo. “Design and construction of a low speed wind tunnel”. In: (), p. 51.

[12] Jean-Philippe Junca-Laplace. “Design, Fabrication and Characterization of a New Wind Tunnel Facility – Linear Cascade with a Wake Simulator”. In: (), p. 134.

[13] DEPARTMENT OF CHEMICAL ENGINEERINGIIT KANPUR. *Elementary-cascade-theory-and-gas-turbine-performance*. (accessed: 01.09.2016).

[14] Bjorn Lindgren and Arne V Johansson. “Evaluation of the Flow Quality in the MTL Wind-Tunnel”. In: (), p. 39.

[15] R D Mehta and P Bradshaw. “Design rules for small low speed wind tunnels”. In: (1979), p. 11.

[16] *Moody DiagramEngineering Toolbox*. https://www.engineeringtoolbox.com/moody-diagram-d_618.html. Accessed: 2010-09-30.

[17] Q H Nagpurwala. “Cascade Aerodynamics and Loss Mechanisms”. In: (), p. 45.

[18] *Open Return Wind TunnelNASA, NASA*. https://www.grc.nasa.gov/WWW/k-12/airplane/tunoret.html. Accessed: 2010-09-30.

[19] P.J.Oliveira. “Notas para Transmissão de Calor”. In: (2015), p. 109.

[20] Satyam Panchal and Vijay Mayavanshi. “Experimental study of flow through compressor Cascade”. In: *Case Studies in Thermal Engineering* 10 (Sept. 2017), pp. 234–243.

[21] I. L. Pioro. “2 - Introduction: Generation IV International Forum”. In: *Handbook of Generation IV Nuclear Reactors*. Ed. by Igor L. Pioro. Woodhead Publishing Series in Energy. Woodhead Publishing, 2016, pp. 37–54.

[22] H Schlichting. “CASCADE FLOW PROBLEMS”. In: (), p. 28.

[23] Ghorbanian K. Soltani M. R. and Manshadi M. D. “Application of Screens and Trips in Enhancement of Flow Characteristics in Subsonic Wind Tunnels”. In: (2010).

[24] Prof. Z. S. Spakovszky. *Unified: Thermodynamics and Propulsion*. Ed. by D. Quattrochi. (accessed: 01.09.2020).

[25] K. W. Todd. “Practical Aspects of Cascade Wind Tunnel Research”. In: *Proceedings of the Institution of Mechanical Engineers* 157.1 (June 1, 1947). Publisher: IMECHE, pp. 482–497.

[26] KG Winter. “Comparative tests of thick and thin turning vanes in the royal aircraft establishment 4 X 3-ft wind tunnel”. In: (1947).

[27] L C Wright. “Blade Selection for a Modern Axial-Flow Compressor”. In: (), p. 24.

[28] X Yan et al. “GTHTR300 design and development”. In: *Nuclear Engineering and Design* 222.2 (June 2003), pp. 247–262.

Appendix A

State of the Art

A.1 Results

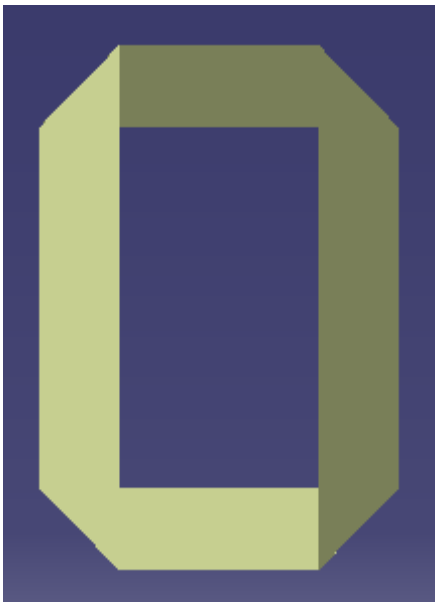

Figure A.1: Side view of the first diffuser.

This Appendix subsection shows in closer detail the side, front and back views of the five diffusers.

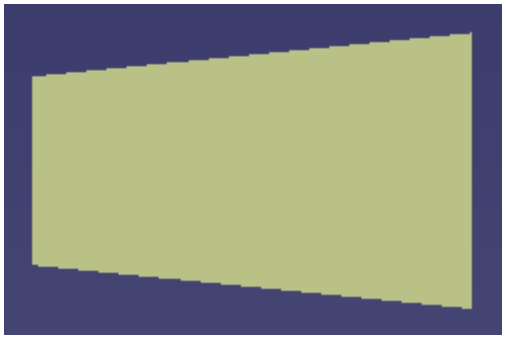

Figure A.2: Front view of the first diffuser.

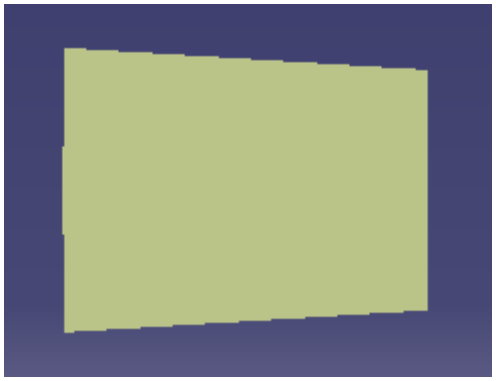

Figure A.3: Left view of the second diffuser.

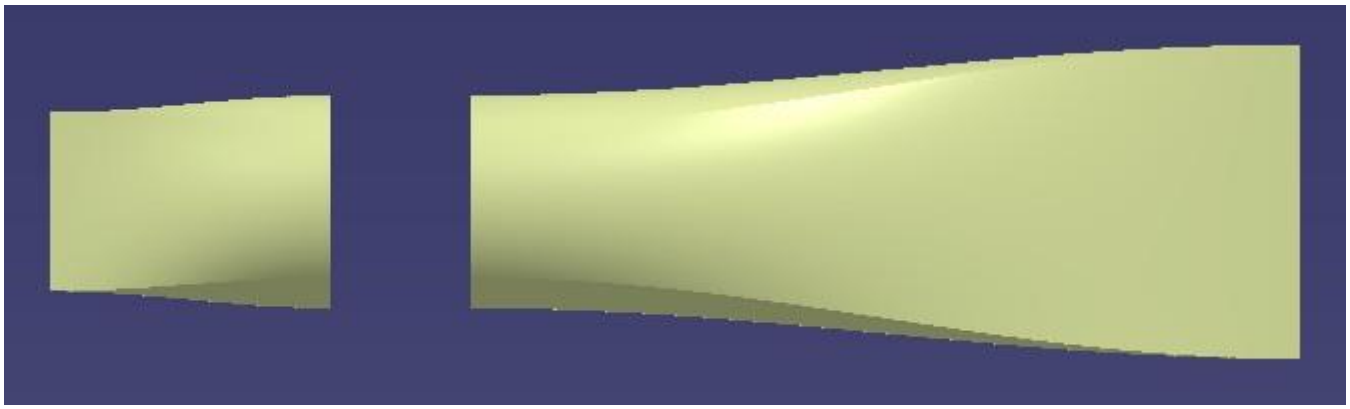

Figure A.4: Right view of the third and fourth diffuser.

Figure A.5: Top view of the third and fourth diffuser.

Figure A.6: Front view of the fifth diffuser.

A.2 Worksheets

GTHTR 300								Cascade Conditions										
Compressor inlet								Properties of helium at standard atmospheric pressure ISA										
Tin	28	C	301	K				Density	0,169	kg/m3	0,178?							
Pin	3,5	Mpa	35	bar				Kinematic viscosity	1,14E-04	m2/s								
m dot	441,8	kg/s						Dynamic viscosity	1,93E-05	kg/m s								
RPM	3600																	
Re Yan et al 2003	1,00E+07							Key parameters for cascade design										
Ma Yan et al 2003	< 0.4																	
gamma	1,6667							Full scale GTHTR 300				Cascade	fullsize	Cascade	3/4 size			
Density	5,5068	kg/m3	*Equation 3 – 19 Petersen: the properties of helium*					Chord (m)	0,107			Chord (m)	0,107	(mm)	150,0	[10,15] cm		
Dynamic viscosity	2E-05	kg/m s	*Equation 6 – 1 Petersen: the properties of helium*					Span (m)	0,102			Span (m)	0,102	(mm)	76,7			
R	2077	J/kg K						V (m/s)	339,82			V (m/s)	106,9	V (m/s)	76			
speed sound	1020,8	m/s						Re	1,00E+07			Target Re	1,00E+05		1,00E+05			
HTR (R1) Takada	0,88	Boss Ratio	(= hub diameter/tip diameter)					Ma	0,333			Ma	0,107	Blade naca 65 series				
Radius (R1) Shroud	0,852	m						blades R1	72			s (m)	0,070	(mm)	52,4			
Radius (R1) Hub	0,750	m						s (m)	0,070			blade						
A annulus	0,514	m2						s/c ratio	0,66			n	11		15			
Vaxial (R1)	155,94	m/s					10	blades S1	94			α1 (degre	3		30			
Ma absolute (R1)	0,1528											α2(degree	7					
U (R1)	301,92	m/s				Re=rho*V1*c/μ					deflection	ε	-4					
Vrel (R1)	339,82	m/s										helium flow						
Alpha	62,68	deg										α1(degree	1,6		157,5			
Ma relative (R1)	0,333											α2(degree	4		4,725			
Chord based on Re Yan	0,107	m									camber	θ	-2,4					
											incidence	i	-3					
Zweifel loading coef	1										deviation	δ	-3					
σx	-30,2411							circular ar			stagger	ξ	5					

Figure A.7: Similarity parameters with GTHTR300.

Figure A.7 is the worksheet where it was developed the similarity relation parameters between GTHTR300 and the project. On the left rows, it is displayed the main parameters of the project GTHTR300 and on the right the three quarters size from the full size GTHTR300 compressor cascade.

In the worksheet displayed in Figure A.8, one can find the calculations to estimate the pressure loss at the testing cascade. Along those results, it is also displayed the estimated X and Y Momentum and forces such as lift and drag.

Following the tables on Figure A.9, from the potential results surrounding the implications of designing the cascade with a 10 cm blade chord to 16 cm blade chord, the red column highlighted reveals the minimum Reynolds number allowed to run the experiment with its respective cascade sizing. And it also presents the chosen chord size (12 cm).

The worksheet displayed in Figure A.10, presents the estimations for the cooling mechanism of the wind tunnel. There are three more of those tables to the respective second, third and fourth duct corner. Yellow highlighted corresponds to the final tempera-

Cascade forces											
p1 (Pa)	845		αm (degre	0,096000442							
p2 (Pa)	839,94		cx (m/s)	99,61946981	99,15383297						
s (m)	0,144		cx1 (m/s)	61,07269784			Blades			Δp_1	10,12
chord (m)	0,120		Momentum				α1 (degre	5		Δp_0	2,296739
α1 (degre	0,087266		X	-0,72898488			α2(degree	8		ζ_{blades}	0,019172
α2 (degre	0,10472		Y	-4,13571337		deflection	ε	-3		ξ	=
c1 [m/s]	100,00						helium flow				
c2[m/s]	99,70	98	Forces				α1(degree	0,0872665		Zweifel loa	1
cy1[m/s]	8,715574		L [N]	-4,18654589			α2(degree	0,1047198		σx	-0,03485
cy2[m/s]	10,42149		D [N]	0,329207517		camber	θ	-0,0174533		a	1,01967
						incidence	i	-5		cθ	-0,00504
			Coeficients			deviation	δ	-7,8952802		γ = ξ	0,143521
			cm (m/s)	100,08029		stagger	ξ	6,5			
			Cl	- 0,046							
			Cd	0,003643897							
	Velocity Triangles										
$\Delta P=\frac{1}{2}\rho V^2\zeta_{oi}$ (Pa)		CFD									
1 blade	620	(Pa)	s/c	(Most severe spacing)							
7 blades	620	(Pa)	0,7								
ζ_{blades}	0,733728										

$$\xi = \frac{\int \rho_1 V_1 \cos\alpha_1 \, dy}{\int \rho_2 V_2 \cos\alpha_2 \, dy}$$

Figure A.8: Cascade forces.

ture of the fluid while orange highlighted to the final temperature of the fluid considering a 50% contingency temperature drop.

Figure A.11 and A.12 estimate the width and length of each component according to the expansion angle of the diffusers and contraction ratio and other intial conditions such as the fan size.

From Figure A.13, it is possible to see the flow rate estimation at the test section as well the pressure loss coefficient at the test section. As well, its Reynolds number, cross section area , volumetric flow rate and hydraulic diameter. In the tables below, the same parameters mentioned previously are estimated for the settling chamber. Regarding the pressure loss due to screens, see Figure A.14 these are compared and the most optimal screen is selected.

Taking a look at Figure A.15, where lies the other student's power estimations, it is relevant to consider the radius of the inlet and exit, inner and outer, radius so that one can predict the sizing of the engine, and with the chord and span of the blades, to estimate the width of the engine's section. Furthermore, it also estimates the mass flow rate required to optimally run the engine, the overall temperature rise, the power input and

				Plate of Blades/ Turn-table							
				Chord (m)	0,1	0,11	0,12	0,13	0,14	0,15	0,16
		%chord	10	thickness (m)	0,010	0,011	0,012	0,013	0,014	0,015	0,016
		n	7	Radius (m)	0,5	0,5	0,5	0,5	0,5	0,5	0,5
upper/lower endwall		%Margin	1	Diameter(m)	1	1	1	1	1	1	1
				y (m)	1	1	1	1	1	1	1
				s (m)	0,155	0,154	0,153	0,152	0,150	0,149	0,148
				s(mm)	155	153,8333	152,66667	151,5	150,3333	149,1667	148
				Ltotal(m)	1,000	1,000	1,000	1,000	1,000	1,000	1,000
				s/c	1,55	1,398485	1,2722222	1,165385	1,07381	0,994444	0,925
				Chord (m)	0,1	0,11	0,12	0,13	0,14	0,15	0,16
		s/c	[0,7;1,2]	s/c	1,2	1,2	1,2	1,2	1,2	1,2	1,2
				s_y(m)	0,12	0,132	0,144	0,156	0,168	0,18	0,192
			[10^5,6*10^5]	Re	8,77E+04	9,65E+04	1,05E+05	1,14E+05	1,23E+05	1,32E+05	1,40E+05
		(Length)	HORIZONTAL	Ltotal(m)	1,13	1,24	1,36	1,47	1,58	1,70	1,81
				y (m)	0,79	0,87	0,95	1,03	1,11	1,19	1,26
				A (m^2)	0,28	0,31	0,34	0,37	0,40	0,43	0,46
		(Height)	VERTICAL	Ltotal(m)	0,81	0,89	0,97	1,05	1,13	1,21	1,29

Figure A.9: Cascade design.

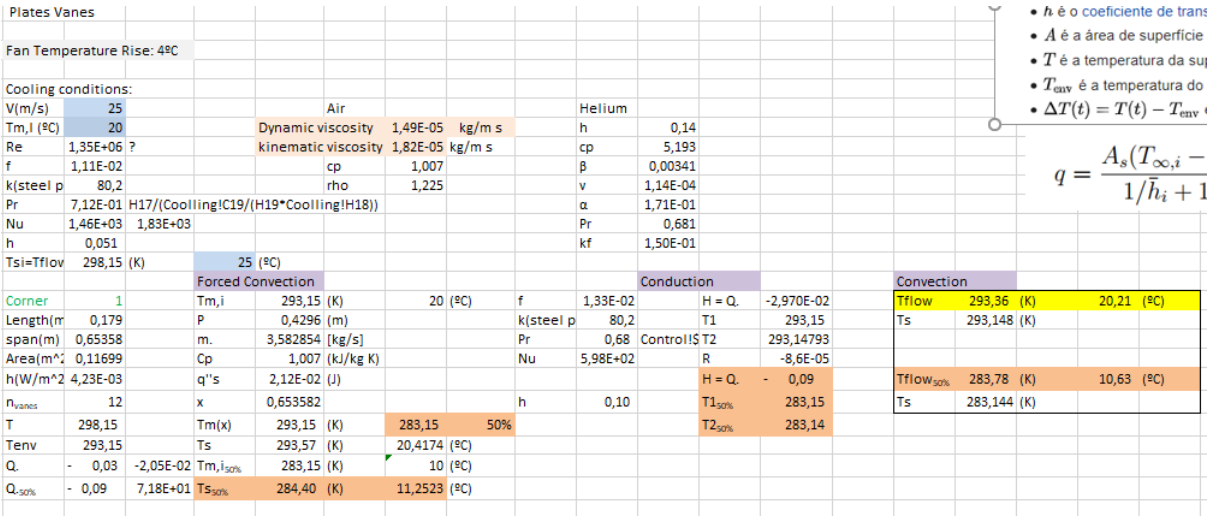

Figure A.10: Cooling estimations.

also specifies the number of compressor blades.

The worksheet from Figure A.16 estimates the width and length of the 5 diffusers as well the pressure loss coefficient that was determined through four different equations and then opted the most optimal result. Apart from the estimated width, height and lenght, it was estimates the previous parameters such as Reynolds number, mass flow rate, velocity and hidraulic diameter.

Figure A.17 shows the design spreadsheet of the first corner duct. It entails the estimated parameters mentioned previously and determines the pressure loss coefficient

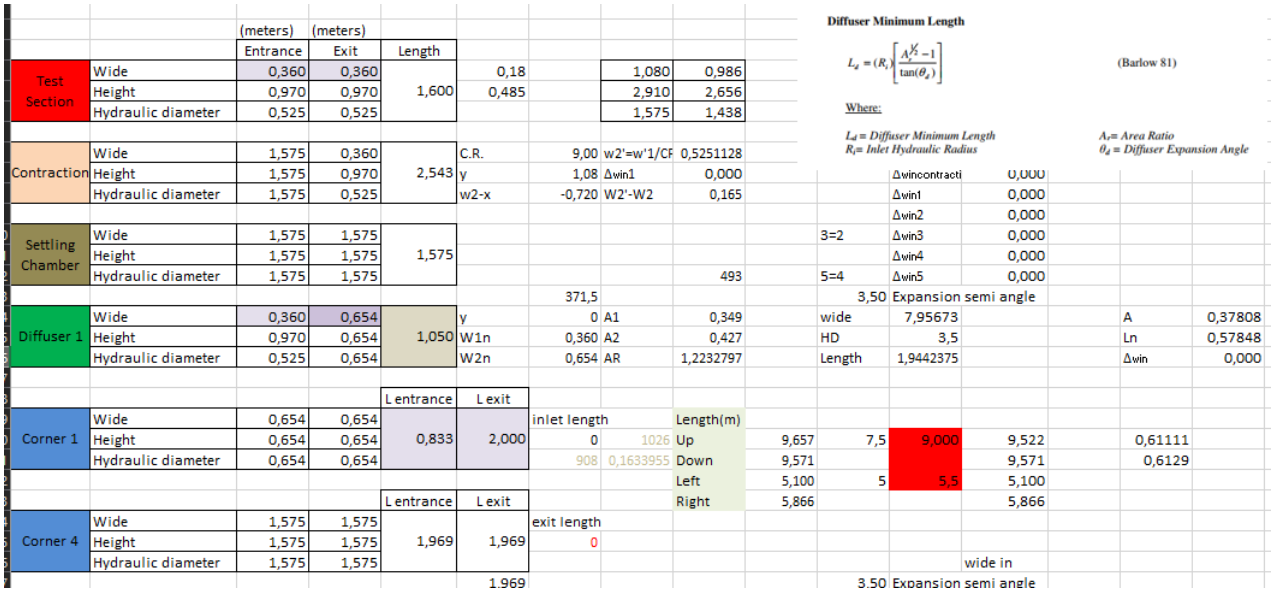

		(meters) Entrance	(meters) Exit	Length				
Test Section	Wide	0,360	0,360	1,600	0,18		1,080	0,986
	Height	0,970	0,970		0,485		2,910	2,656
	Hydraulic diameter	0,525	0,525				1,575	1,438
Contraction	Wide	1,575	0,360	2,543	C.R.	9,00	w2'=w'1/CF	0,5251128
	Height	1,575	0,970		y	1,08	Δwin1	0,000
	Hydraulic diameter	1,575	0,525		w2-x	-0,720	W2'-W2	0,165
Settling Chamber	Wide	1,575	1,575	1,575				
	Height	1,575	1,575					
	Hydraulic diameter	1,575	1,575					493
						371,5		
Diffuser 1	Wide	0,360	0,654	1,050	y	0	A1	0,349
	Height	0,970	0,654		W1n	0,360	A2	0,427
	Hydraulic diameter	0,525	0,654		W2n	0,654	AR	1,2232797
				L entrance	L exit			
Corner 1	Wide	0,654	0,654	0,833	2,000	inlet length		Length(m)
	Height	0,654	0,654			0	1026	Up
	Hydraulic diameter	0,654	0,654			908	0,1633955	Down
								Left
				L entrance	L exit			Right
Corner 4	Wide	1,575	1,575			exit length		
	Height	1,575	1,575	1,969	1,969	0		
	Hydraulic diameter	1,575	1,575					
					1,969			

Diffuser Minimum Length

$$L_d = (R_t)\left[\frac{A_r^{N} - 1}{\tan(\theta_d)}\right] \qquad \text{(Barlow 81)}$$

Where:

L_d = Diffuser Minimum Length
R_t = Inlet Hydraulic Radius
A_r = Area Ratio
θ_d = Diffuser Expansion Angle

												Δwincontracti	0,000				
												Δwin1	0,000				
												Δwin2	0,000				
											3=2	Δwin3	0,000				
												Δwin4	0,000				
											5=4	Δwin5	0,000				
											3,50	Expansion semi angle					
											wide	7,95673				A	0,37808
											HD	3,5				Ln	0,57848
											Length	1,9442375				Δwin	0,000
									9,657	7,5	9,000	9,522			0,61111		
									9,571			9,571			0,6129		
									5,100	5	5,5	5,100					
									5,866			5,866					
													wide in				
											3.50	Expansion semi angle					

Figure A.11: Component dimensioning.

through three different equations while taking into consideration the effect of the turning vanes. There are three more tables similiar to these that correspond to the second, third and fourth corner duct.

Following the spreadsheet from Figure A.18, apart from determining the parameters mentioned previously, it accounts to the shape of the contraction cone, given that its inlet is a square and the outlet of the contraction is a rectangle. A polynomial function had to be written to predict the shape of the contraction cone. This spreadsheet also entails the estimation of the pressure loss.

Finally, the spreadsheet in Figure A.19 was used to have a better understanding of aerodynamic relations such as energy ratio, flow rate, pressure, etc, and once these estimations are complementary and the spreadsheet is iterative, when fixing a variable, one can see the specific and overall changes.

Corner 4	Height	1,575	1,575	1,969	1,969	0								
	Hydraulic diameter	1,575	1,575									wide in		
					1,969					3,50	Expansion semi angle			
Diffuser 5	Wide	1,358	1,575		y	0				wide	3,5	1,3575832		
	Height	1,358	1,575	1,780	W1n	1,358				height	3,5			
	Hydraulic diameter	1,358	1,575		W2n	1,575		Δwin	0,000	Length	1,1693518			
				L entrance	L exit		0,82	0,773	0,920	1,358				
Corner 3	Wide	1,358	1,358											
	Height	1,358	1,358	2,497	2,117	inlet length		0,654	0,525	1,575				
	Hydraulic diameter	1,358	1,358			0,8								
				3,297						3,50	Expansion OUT			
Diffuser 4	Wide	0,920	1,358		y	0				wide	3,5	1,0545578		
	Height	0,920	1,358	3,577	W1n	0,920				height	3,5			
	Hydraulic diameter	0,920	1,358		W2n	1,358	3534,37mm	Δwin	0,000	Length	3,5772113	1,1		
							42,63							
Power Plant	Wide	0,920	0,920											
	Height	0,920	0,920	0,600										
	Hydraulic diameter	0,920	0,920											
										3,50	Expansion OUT			
Diffuser 2	Wide	0,654	0,773		y	0				wide	3,5	0,7759071	AR	1,40048
	Height	0,654	0,773	0,980	W1n	0,654				height	3,5			
	Hydraulic diameter	0,654	0,773		W2n	1,037		Δwin	0,000	Length	0,9517097	1		
	Dc1_cc2									L_d	1,96			
	3,91			L entrance	L exit									
Corner 2	Wide	0,773	0,773											
	Height	0,773	0,773	2,120	1,758	inlet length								
	Hydraulic diameter	0,773	0,773			0,8448041	0,1933652							
				3,287	1618,000					3,50	Expansion IN			
Diffuser 3	Wide	0,773	0,920		y	0				wide	3,40902	0,8588374	8,33675	
	Height	0,773	0,920						G145-C14	height	3,40902			
	Hydraulic diameter	0,773	0,920		W2n	0,920		Δwin	0,000	Length	1,1979489	0,5		

Linhas de Grade PrincipaisEixoVertical (Valor)

Figure A.12: Component dimensioning(continuation).

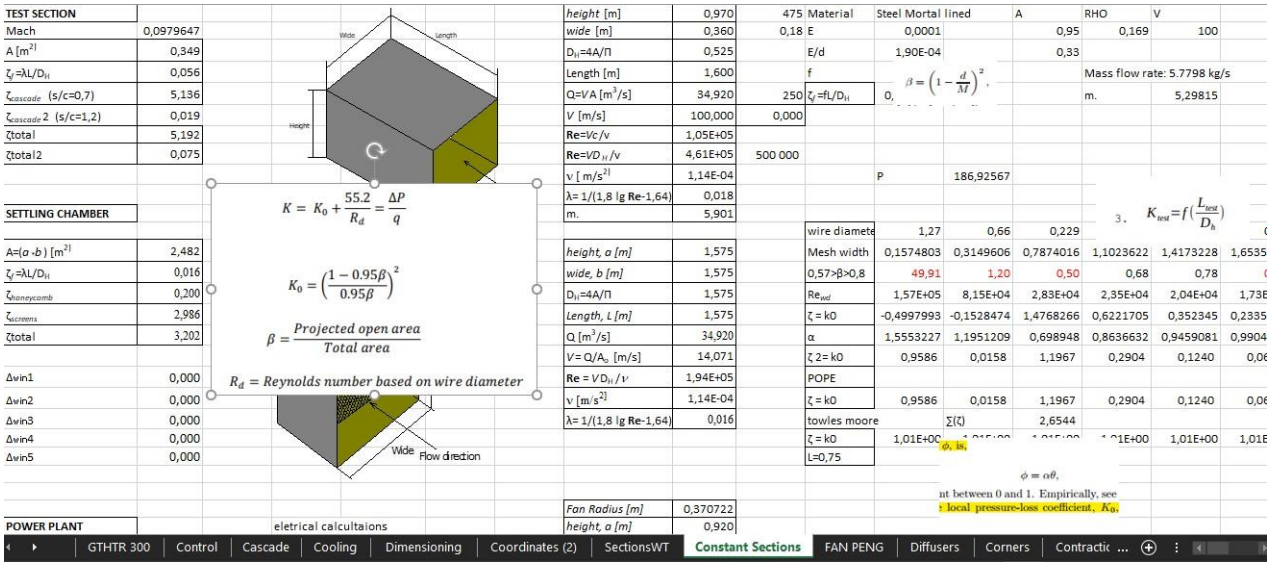

Figure A.13: Test section and settling chamber design.

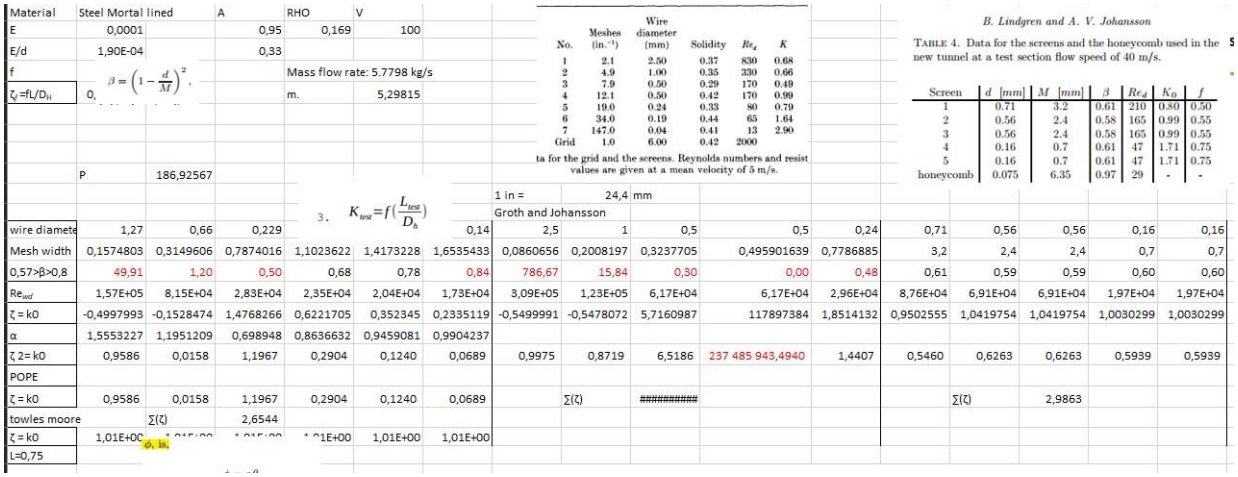

Material	Steel Mortal lined		A	RHO	V										
E	0,0001		0,95	0,169	100										
E/d	1,90E-04		0,33												
f		$\beta = \left(1 - \frac{d}{M}\right)^2$		Mass flow rate: 5.7798 kg/s											
ζ_f=fL/D_H	0,			m.	5,29815										
	P	186,92567													
						1 in =	24,4	mm							
						Groth and Johansson									
wire diamete	1,27	0,66	0,229		0,14	2,5	1	0,5	0,5	0,24	0,71	0,56	0,56	0,16	0,16
Mesh width	0,1574803	0,3149606	0,7874016	1,1023622	1,4173228	1,6535433	0,0860656	0,2008197	0,3237705	0,495901639	0,7786885	3,2	2,4	2,4	0,7	0,7
0,57>β>0,8	49,91	1,20	0,50	0,68	0,78	0,84	786,67	15,84	0,30	0,00	0,48	0,61	0,59	0,59	0,60	0,60
Re_{wd}	1,57E+05	8,15E+04	2,83E+04	2,35E+04	2,04E+04	1,73E+04	3,09E+05	1,23E+05	6,17E+04	6,17E+04	2,96E+04	8,76E+04	6,91E+04	6,91E+04	1,97E+04	1,97E+04
ζ = k0	-0,4997993	-0,1528474	1,4768266	0,6221705	0,352345	0,2335119	-0,5499991	-0,5478072	5,7160987	117897384	1,8514132	0,9502555	1,0419754	1,0419754	1,0030299	1,0030299
α	1,5553227	1,1951209	0,698948	0,8636632	0,9459081	0,9904237										
ζ 2= k0	0,9586	0,0158	1,1967	0,2904	0,1240	0,0689	0,9975	0,8719	6,5186	237 485 943,4940	1,4407	0,5460	0,6263	0,6263	0,5939	0,5939
POPE																
ζ = k0	0,9586	0,0158	1,1967	0,2904	0,1240	0,0689		∑(ζ)	##########				∑(ζ)	2,9863		
towles moore		∑(ζ)	2,6544													
ζ = k0	1,01E+00			1,01E+00	1,01E+00	1,01E+00										
L=0,75																

B. Lindgren and A. V. Johansson

TABLE 4. Data for the screens and the honeycomb used in the new tunnel at a test section flow speed of 40 m/s.

Screen	d [mm]	M [mm]	β	Re_d	K_0	f
1	0.71	3.2	0.61	210	0.80	0.50
2	0.56	2.4	0.58	165	0.99	0.55
3	0.56	2.4	0.58	165	0.99	0.55
4	0.16	0.7	0.61	47	1.71	0.75
5	0.16	0.7	0.61	47	1.71	0.75
honeycomb	0.075	6.35	0.97	29	-	-

No.	Meshes (in.$^{-1}$)	Wire diameter (mm)	Solidity	Re_d	K
1	2.1	2.50	0.37	830	0.68
2	4.9	1.00	0.35	330	0.66
3	7.9	0.50	0.29	170	0.49
4	12.1	0.50	0.42	170	0.99
5	19.0	0.24	0.33	80	0.79
6	34.0	0.19	0.44	65	1.64
7	147.0	0.04	0.41	13	2.90
Grid	1.0	6.00	0.42	2000	

ta for the grid and the screens. Reynolds numbers and resist values are given at a mean velocity of 5 m/s.

Figure A.14: Screens comparison.

	Vax	80	Cp	5190							
	Hub tip ratio	Inlet outer radius[m]	Inlet inner radius[m]	Exit outer radius[m]	Exit inner radius[m]	Rotational speed[rev/s]	rpm	omega	Mean blade speed[m/s]	Flow coefficient	
	0,6	0,4653	0,2792	0,4638	0,2807	77	4620	483,8	180,09	0,4442	
			blade span inlet	blade span average	blade span outlet	Chord					
			0,1861	0,1846	0,1831	0,062					
				Absoute	Absoute	Absoute	Relative	Relative			
	Stage number	Loading coefficient	efficiency	Alpha 1[deg]	Alpha 2[deg]	Alpha 3[deg]	Beta 1[deg]	Beta 2[deg]	Diffusion factor	Power input [kW]	Temperature rise [C]
	1	0,312	0,853	0	35,63	28,65	66,05	56,91	0,4529	59,7	2,0
	2	0,293	0,903	28,65	51,44	20	59,61	44,9	0,4683	59,0	2,0
										118,7	4,0
	Fan Radius	A	Diameter				Delta Beta	s/c	s	No blades	
Schroud	0,46455	0,6779768	0,9291				9,14	1,5	0,0923	13	
	0,27995	0,2462129					14,71	0,7	0,0431	27	
	0,370721863	0,4317638									

Figure A.15: Liming Peng estimations.

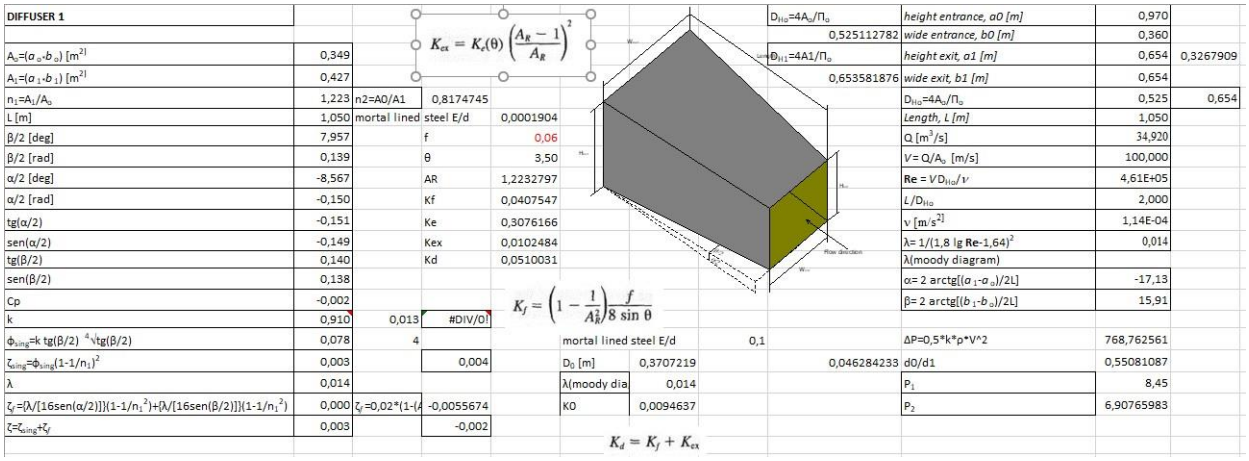

DIFFUSER 1										
		$K_{ex} = K_c(\theta)\left(\frac{A_R - 1}{A_R}\right)^2$					D_{Ho}=4A_o/Π_o	height entrance, a0 [m]	0,970	
							0,525112782	wide entrance, b0 [m]	0,360	
A_o=(σ_o·b_o) [m^2]	0,349						D_{H1}=4A1/Π_o	height exit, a1 [m]	0,654	0,3267909
A_1=(σ_1·b_1) [m^2]	0,427						0,653581876	wide exit, b1 [m]	0,654	
n_1=A_1/A_o	1,223	n2=A0/A1	0,8174745					D_{Ho}=4A_o/Π_o	0,525	0,654
L [m]	1,050	mortal lined	steel E/d	0,0001904				Length, L [m]	1,050	
β/2 [deg]	7,957		f	0,06				Q [m^3/s]	34,920	
β/2 [rad]	0,139		θ	3,50				V= Q/A_o [m/s]	100,000	
α/2 [deg]	-8,567		AR	1,2232797				**Re** = VD_{Ho}/ν	4,61E+05	
α/2 [rad]	-0,150		Kf	0,0407547				L/D_{Ho}	2,000	
tg(α/2)	-0,151		Ke	0,3076166				ν [m/s^2]	1,14E-04	
sen(α/2)	-0,149		Kex	0,0102484				λ= 1/(1,8 lg **Re**-1,64)^2	0,014	
tg(β/2)	0,140		Kd	0,0510031				λ(moody diagram)		
sen(β/2)	0,138							α= 2 arctg[(a$_1$-σ_o)/2L]	-17,13	
Cp	-0,002							β= 2 arctg[(b$_1$-b_o)/2L]	15,91	
k	0,910	0,013	#DIV/0!							
ϕ_{wing}=k tg(β/2) $^4\sqrt{}$tg(β/2)	0,078	4			mortal lined	steel E/d	0,1	ΔP=0,5*k*ρ*V^2	768,762561	
ζ_{wing}=ϕ_{wing}(1-1/n_1)^2	0,003		0,004		D_0 [m]	0,3707219		0,046284233 d0/d1	0,55081087	
λ	0,014				λ(moody dia	0,014		P_1	8,45	
ζ_f=[λ/[16sen(α/2)]](1-1/n_1^2)+[λ/[16sen(β/2)]](1-1/n_1^2)	0,000	ζ_f =0,02*(1-(	-0,0055674		K0	0,0094637		P_2	6,90765983	
ζ=ζ_{wing}+ζ_f	0,003		-0,002							

$$K_f = \left(1 - \frac{1}{A_R^2}\right)\frac{f}{8\sin\theta}$$

$$K_d = K_f + K_{ex}$$

Figure A.16: Diffusers design.

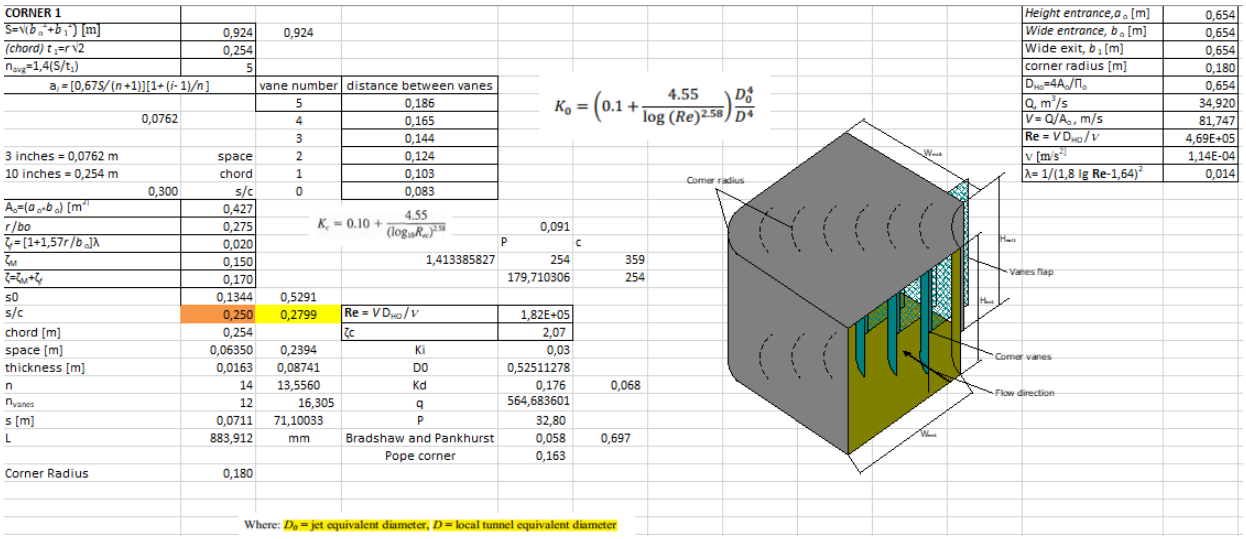

CORNER 1						
$S=\sqrt{(b_o^2+b_1^2)}$ [m]	0,924	0,924				
(chord) $t_1=r\sqrt{2}$	0,254					
$n_{ave}=1,4(S/t_1)$	5					
$a_i=[0,67S/(n+1)][1+(i-1)/n]$		vane number	distance between vanes			
		5	0,186			
0,0762		4	0,165			
		3	0,144			
3 inches = 0,0762 m	space	2	0,124			
10 inches = 0,254 m	chord	1	0,103			
0,300	s/c	0	0,083			
$A_o=(a_o \cdot b_o)$ [m²]	0,427					
r/bo	0,275		$K_c = 0.10 + \frac{4.55}{(\log_{10} R_e)^{2.58}}$	0,091		
$\zeta_t=[1+1,57r/b_o]\lambda$	0,020			P	c	
ζ_M	0,150		1,413385827	254	359	
$\zeta=\zeta_M+\zeta_t$	0,170			179,710306	254	
s0	0,1344	0,5291				
s/c	0,250	0,2799	Re = $V D_{HO}/\nu$	1,82E+05		
chord [m]	0,254		ζc	2,07		
space [m]	0,06350	0,2394	Ki	0,03		
thickness [m]	0,0163	0,08741	D0	0,52511278		
n	14	13,5560	Kd	0,176	0,068	
n_{vanes}	12	16,305	q	564,683601		
s [m]	0,0711	71,10033	P	32,80		
L	883,912	mm	Bradshaw and Pankhurst	0,058	0,697	
			Pope corner	0,163		
Corner Radius	0,180					

Where: D_0 = jet equivalent diameter, D = local tunnel equivalent diameter

$$K_0 = \left(0.1 + \frac{4.55}{\log(Re)^{2.58}}\right)\frac{D_0^4}{D^4}$$

Height entrance, a_o [m]	0,654
Wide entrance, b_o [m]	0,654
Wide exit, b_1 [m]	0,654
corner radius [m]	0,180
$D_{HO}=4A_o/\Pi_o$	0,654
Q, m³/s	34,920
$V = Q/A_o$, m/s	81,747
Re = $V D_{HO}/\nu$	4,69E+05
ν [m/s²]	1,14E-04
λ= 1/(1,8 lg **Re**-1,64)²	0,014

Figure A.17: Corner ducts design.

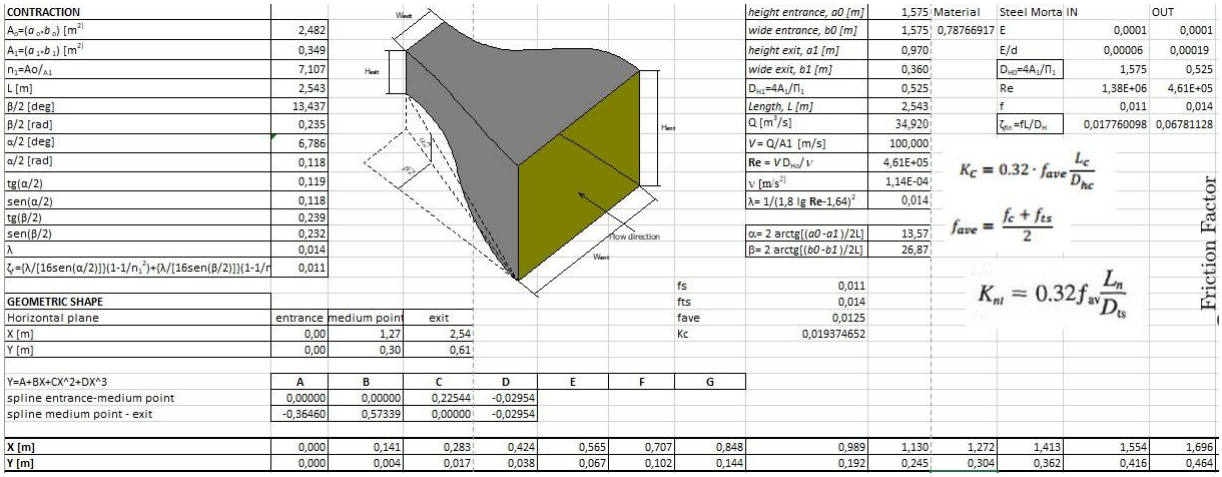

CONTRACTION													
$A_o=(a_o \cdot b_o)$ [m²]	2,482												
$A_1=(a_1 \cdot b_1)$ [m²]	0,349												
$n_1=Ao/_{A1}$	7,107												
L [m]	2,543												
β/2 [deg]	13,437												
β/2 [rad]	0,235												
α/2 [deg]	6,786												
α/2 [rad]	0,118												
tg(α/2)	0,119												
sen(α/2)	0,118												
tg(β/2)	0,239												
sen(β/2)	0,232												
λ	0,014												
$\zeta_t=[\lambda/[16\text{sen}(\alpha/2)]](1-1/n_1^2)+[\lambda/[16\text{sen}(\beta/2)]](1-1/n$	0,011												
								fs	0,011				
								fts	0,014				
								fave	0,0125				
								Kc	0,019374652				
GEOMETRIC SHAPE													
Horizontal plane	entrance	medium point	exit										
X [m]	0,00	1,27	2,54										
Y [m]	0,00	0,30	0,61										
Y=A+BX+CX^2+DX^3	A	B	C	D	E	F	G						
spline entrance-medium point	0,00000	0,00000	0,22544	-0,02954									
spline medium point - exit	-0,36460	0,57339	0,00000	-0,02954									
X [m]	0,000	0,141	0,283	0,424	0,565	0,707	0,848	0,989	1,130	1,272	1,413	1,554	1,696
Y [m]	0,000	0,004	0,017	0,038	0,067	0,102	0,144	0,192	0,245	0,304	0,362	0,416	0,464

height entrance, a0 [m]	1,575	Material	Steel Morta	IN		OUT
wide entrance, b0 [m]	1,575	0,78766917	E	0,0001		0,0001
height exit, a1 [m]	0,970		E/d	0,00006		0,00019
wide exit, b1 [m]	0,360		$D_{HO}=4A_1/\Pi_1$	1,575		0,525
$D_{H1}=4A_1/\Pi_1$	0,525		Re	1,38E+06		4,61E+05
Length, L [m]	2,543		f	0,011		0,014
Q [m³/s]	34,920		$\zeta_{fo}=fL/D_H$	0,017760098		0,06781128
$V = Q/A1$ [m/s]	100,000					
Re = $V D_{HO}/\nu$	4,61E+05					
ν [m/s²]	1,14E-04					
λ= 1/(1,8 lg **Re**-1,64)²	0,014					
α= 2 arctg[(a0-a1)/2L]	13,57					
β= 2 arctg[(b0-b1)/2L]	26,87					

$$K_C = 0.32 \cdot f_{ave}\frac{L_c}{D_{hc}}$$

$$f_{ave} = \frac{f_c + f_{ts}}{2}$$

$$K_{nl} = 0.32 f_{av}\frac{L_n}{D_{ts}}$$

Friction Factor

Figure A.18: Contraction design.

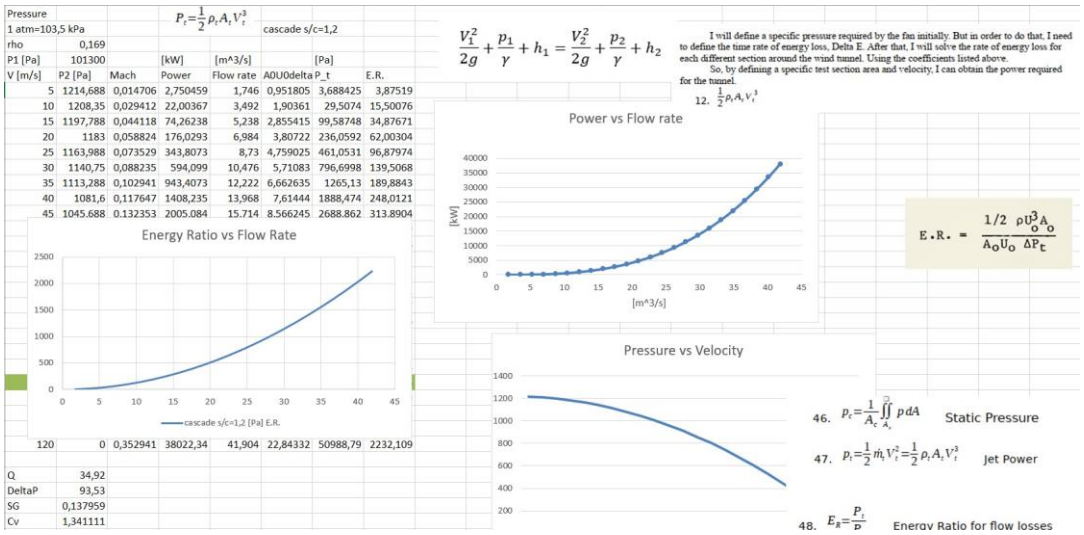

Pressure								
1 atm=103,5 kPa					cascade s/c=1,2			
rho	0,169							
P1 [Pa]	101300		[kW]	[m^3/s]		[Pa]		
V [m/s]	P2 [Pa]	Mach	Power	Flow rate	A0U0delta	P_t	E.R.	
5	1214,688	0,014706	2,750459	1,746	0,951805	3,688425	3,87519	
10	1208,35	0,029412	22,00367	3,492	1,90361	29,5074	15,50076	
15	1197,788	0,044118	74,26238	5,238	2,855415	99,58748	34,87671	
20	1183	0,058824	176,0293	6,984	3,80722	236,0592	62,00304	
25	1163,988	0,073529	343,8073	8,73	4,759025	461,0531	96,87974	
30	1140,75	0,088235	594,099	10,476	5,71083	796,6998	139,5068	
35	1113,288	0,102941	943,4073	12,222	6,662635	1265,13	189,8843	
40	1081,6	0,117647	1408,235	13,968	7,61444	1888,474	248,0121	
45	1045.688	0.132353	2005.084	15.714	8.566245	2688.862	313.8904	
120	0	0,352941	38022,34	41,904	22,84332	50988,79	2232,109	
Q	34,92							
DeltaP	93,53							
SG	0,137959							
Cv	1,341111							

$$P_t = \frac{1}{2}\rho_t A_t V_t^3$$

$$\frac{V_1^2}{2g} + \frac{p_1}{\gamma} + h_1 = \frac{V_2^2}{2g} + \frac{p_2}{\gamma} + h_2$$

I will define a specific pressure required by the fan initially. But in order to do that, I need to define the time rate of energy loss, Delta E. After that, I will solve the rate of energy loss for each different section around the wind tunnel. Using the coefficients listed above.
So, by defining a specific test section area and velocity, I can obtain the power required for the tunnel.

12. $\frac{1}{2}\rho_t A_t V_t^3$

Power vs Flow rate

Energy Ratio vs Flow Rate

$$E.R. = \frac{1/2\ \rho U_o^3 A_o}{A_o U_o\ \Delta P_t}$$

Pressure vs Velocity

46. $p_c = \frac{1}{A_c}\iint_{A_c} p\,dA$ Static Pressure

47. $P_t = \frac{1}{2}\dot{m}_t V_t^2 = \frac{1}{2}\rho_t A_t V_t^3$ Jet Power

48. $E_R = \frac{P_t}{P}$ Energy Ratio for flow losses

Figure A.19: Complementing estimations and graphics.